STRESS CORROSION CRACKING

OF ROTOR STEELS

IN CARBONATE / BICARBONATE

AND SODIUM HYDROXIDE SOLUTIONS

By

JOHANN RECHBERGER

Dipl. Ing. ETH, Swiss Federal Institute of Technology, 1982

A THESIS SUBMITTED IN PARTIAL FULFILLMENT OF

THE REQUIREMENTS FOR THE DEGREE OF

MASTER OF APPLIED SCIENCE

in

THE FACULTY OF GRADUATE STUDIES

Department of Metallurgical Engineering

We accept this thesis as conforming

to the required standard

THE UNIVERSITY OF BRITISH COLUMBIA

February 1986

In presenting this thesis in partial fulfilment of the requirements for an advanced degree at the University of British Columbia, I agree that the Library shall make it freely available for reference and study. I further agree that permission for extensive copying of this thesis for scholarly purposes may be granted by the head of my department or by his or her representatives. It is understood that copying or publication of this thesis for financial gain shall not be allowed without my written permission.

Department of _Met. Eng._

The University of British Columbia
1956 Main Mall
Vancouver, Canada
V6T 1Y3

Date _February, 27th 1986_

ABSTRACT

In this study, the stress corrosion behavior of 3.5%NiCrMoV and 1%CrMoV steels was investigated. Tests were conducted at 95°C in carbonate/bicarbonate and sodium hydroxide solutions. Results from slow strain rate tensile tests and fracture mechanics experiments were compared. A new, easily machinable, specimen geometry for fracture mechanics experiments was tested. The influence of pH, potential, microstructure and inclusions were studied.

Stress corrosion cracking (SCC) was found with all three steels in the 3.5M NaOH solution at active, passive and transpassive potentials. In the 1M carbonate/bicarbonate solutions, the 1%CrMoV steels showed very severe cracking only during slow strain rate experiments. No major difference in cracking behavior was found between a regular 3.5%NiCrMoV steel and a super clean 3.5%NiCrMoV steel with low Mn and Si content. In acidic CO_2/H_2O environments, crack tip blunting was observed due to strong dissolution processes.

TABLE OF CONTENTS

LIST OF TABLES

LIST OF FIGURES

LIST OF SYMBOLS AND ABBREVIATIONS

Symbol

a	crack length
Δa	crack propagation
B	specimen width
CC, CL, LC	description of fracture plane
F	Faraday constant
I	moment of inertia
i	anodic current density
K_I	stress intensity for mode I opening
$K_I(a)$	stress intensity with crack length a
K_{IC}	fracture toughness
K_{ISCC}	threshold stress intensity
L	lever arm
M	bending moment
P	load
p	density
σ	bending stress
v	crack velocity
V_{SCE}	volts with resp. to standard calomel electrode
V_{SHE}	volts with resp. to stand. hydrogen electrode
W	specimen thickness
W'	equivalent weight
x	distance from neutral fiber
Y	specimen geometry correction factor

Abbreviation

DCB	double cantilever beam
EDX	energy dispersive X-ray analysis
HSLA	high strength low alloy steel
PTFE	polytetrafluorethylene ("Teflon")
R_C	Rockwell-C hardness
SCC	stress corrosion cracking
SEM	scanning electron microscope
Steel-"A"	3.5%NiCrMoV steel with low Mn and Si content
Steel-"O"	1%CrMoV steel
Steel-"R"	3.5%NiCrMoV steel
SSRT	slow strain rate tensile test
TN-DCB	T-notch double cantilever beam
TEM	transmission electron microscope
v-K plot	crack velocity vs. stress intensity

ACKNOWLEDGEMENTS

I.   INTRODUCTION

Most modern low pressure (LP) steam turbines (shafts
and discs) are made out of steels that have Ni, Cr, Mo and V
as major alloying elements. Stress corrosion cracking (SCC)
of these steels can cause catastrophic failure of the
turbine with obvious safety hazard to personnel and enormous
economic impact to the power generating industry. A survey
in the U.S. in 1980 showed that more than one third of the
inspected power plants had LP disc cracking problems[1,2]. The
cracks were often found in keyways and the blade attachment
regions, both areas that are highly stressed and conducive
to the formation of a crevice.   From the crack length and
the operating time, typical crack growth rates of 10^{-10} m/s
to 10^{-12} m/s were calculated[3].

Even if the service environment is, in most cases,
highly purified steam[4], various corrosion products are found
in the stress corrosion cracks, for example, iron oxides,
chlorides, sulphates and carbonates.   In some cases,
strongly alkaline hydroxide deposits are found in the
cracked regions[3]. It can be assumed that various steam
impurities get   concentrated   at   locations   of   steam
condensation and therefore produce locally very aggressive
environments.

To determine the susceptibility of rotor steel to SCC,
various test methods are being applied. Examples are:

constant load, slow strain rate tensile tests or fracture mechanics tests. The test environments chosen are often quite different from the original steam composition because of the need to simulate the worst conditions which could exist, for example, in local condensates at a keyway. This also includes the corrosion potential which can be controlled by imposing a specific potential onto the test piece by means of an external DC electrical source.

With these stress corrosion experiments, data can be obtained in a relatively short time. But even so, test periods of several hundred hours are quite common. One has to bear in mind that turbines are in operation for many years or decades and, therefore, even very small cracking rates cannot be tolerated.

1.1. Rotor - Steel

The size of rotor forgings has steadily increased over the past years accompanied by a corresponding increase in inlet steam pressures and temperatures. Requirements arose for improved material properties for the high pressure (HP) and the intermediate pressure (IP) rotors at elevated temperatures and for the low pressure (LP) rotors at low temperatures. These requirements have been met by improvements in steel making processes, refinements of alloy compositions and heat treatment, as well as forging practice[5].

Steel making process:

The most commonly adopted method is basic electric arc melting followed by a vacuum treatment of the molten steel, either by ladle degassing or by stream degassing of the ingot. Careful ladle metallurgy methods allows control of very low levels of P and S, whereas the contents of As, Sb, Sn and Cu can only be kept low by proper selection of raw materials[6]. Finally, uphill pouring under protective atmosphere prevents hydrogen and nitrogen pickup during the casting process[7].

Alloy composition[5]:

The high temperature HP and IP rotors are mainly made out of steel with approximately 0.25% C, 1% Cr, 1% Mo and 0.3% V. The high steam admission temperatures of up to 540°C require a material with a good balance of creep strength, ductility and toughness.

For the low temperature LP rotors, a 3.5%NiCrMoV - steel is normally used with a balance maintained between strength level and toughness. Creep properties are not important at the gas inlet temperatures below 300°C. The nickel content may vary between 2 and 3.75%, depending upon the diameter, strength, and toughness requirements for the rotor.

1.2. Microstructure / Heat treatment

LP as well as HP rotor steels are heat treated to produce an upper bainitic structure. This microstructure proved to give the best combination of strength, toughness and stress corrosion cracking resistance in the LP rotor steels[9,10,11] and gave especially good creep rupture properties in the HP rotor steels[12].

The bainitic microstructure is normally obtained by an austenizing treatment at 960-975°C for 1%CrMoV - steels and 830-850°C for 3.5%NiCrMoV - steels, followed by oil or water quenching respectively.

Tempering treatments are in the temperature range of 690-710°C for 1%CrMoV-steels and 600-620°C for 3.5%NiCrMoV-steels. To minimize residual stresses, slow furnace cooling from the tempering temperature is necessary, especially for large forgings.

A major disadvantage of the heat treated NiCrMoV-steels is their sensitivity to temper embrittlement in the temperature range of 350-450°C. This detrimental effect is caused by the segregation of impurity elements at the prior austenite grain boundaries (P, Sn, As, Sb, together with Ni, Cr and Mo)[13,14]. It has been found that a lowering of the Si and Mn content together with additions of Mo can reduce the severity of embrittlement[7,15].

1.3. Stress corrosion cracking of rotor alloys

1.3.1. General mechanisms of SCC

The various models of SCC can be largely divided into two basic classes: those which consider that crack propagation proceeds by anodic dissolution at the crack tip and those which consider that crack propagation is essentially mechanical. At present, the film rupture or slip step dissolution models are widely quoted.

Vermilyea[16] proposes a film rupture model whereby a protective film is ruptured by plastic strain at the crack tip and allows the crack to advance by dissolution until repassivation occurs (repassivation time may range from 10^{-3} to 1 second). After repassivation, plastic flow near the crack tip accumulates strain until at a critical value the film ruptures and dissolution can take place again.

Staehle[17] formulates a mechanism by which a protective surface film is ruptured by slip processes. The newly exposed bare metal at slip sites (so called slip steps) allows metal dissolution. Depending on the potential and the chemistry of the environment at the crack tip, repassivation takes place and subsequent film rupture and dissolution cycles lead to further cracking of the material. Staehle points out that crack advance can be noticed only in specific electrochemical conditions at the crack tip. Three

cases are distinguished: very fast repassivation of the slip step which gives virtually no incremental advance; very fast dissolution which causes pitting or crack blunting; a critical ratio of dissolution-attack to repassivation, at which continued penetration takes place.

Uhlig[18] describes an adsorption of surface active species, the consequence of which is a reduction in the surface energy required to form a crack, and therefore, a reduced fracture stress. Various embrittlement phenomena have been explained by this model.

There is often dispute as to whether the failure of a material is actually attributed to SCC or to hydrogen embrittlement. From a thermodynamic point of view, one could say that alloys cracking preferentially at anodic potentials are sensitive to SCC, whereas cracking in the cathodic region is evidence of hydrogen induced cracking. But this potential dependence is an uncertain criterion since it is well known[19,20,21] that crack tip conditions (potential and pH) may vary considerably from those measured at the bulk metal/electrolyte interface.

Presently, there exists no single coherent theory that explains all of the observed stress corrosion phenomena. In many cases, no clear distinction between SCC and hydrogen induced cracking can be drawn.

1.3.2. Controlling factors for SCC

The following factors play important roles in the SCC behavior of rotor steels:

-Chemical composition, concentration, and temperature of the "corrosive" environment.

-Electrochemical potential

-Material composition

The stress levels and rotor design are also parameters that influence the SCC behavior of a turbine, but these will not be discussed in further detail.

1.3.3. Environment

Laboratory tests have shown that steels, heat treated to high strength values (>950 MNm^{-2}), are susceptible to SCC in high purity water or steam as well as in aqueous solutions containing various anions, for example, Cl^-, HS^-, SO_4^{2-}, HCO_3^-, CO_3^{2-} and OH^- [10,21-30]. However, it must be reemphasised that even if tests are conducted in dilute aqueous solutions, the chemistry inside the crack may be very different. This can be due to concentration of damaging species by physical means (diffusion, evaporation of solvent) or by electro chemical reactions inside cracks. Also, chemical leaching[31] of the alloy or reactions with impurities in the metal[32] can cause local changes in the environment.

For steam turbine materials concentrated solutions of caustics, chlorides and hydrogen sulphide are found to cause cracking[31,33,34,35]. More recent investigations showed that at very high stress levels cracking also occurs in steam and pure water[2,4,36].

McMinn et al[3] studied the effect of temperature and caustic concentration on SCC susceptibility and found that increasing temperature lowers the caustic concentration necessary for cracking. At temperatures below 50°C, even in very concentrated solutions, no cracking was found.

Shalvoy et al[37] investigated the effect of various steam impurities and found that such species (eg. Nitrates) can cause an anodic shift in the free corrosion potential and enhance caustic SCC. Also gaseous impurities like CO_2 can result in accelerated cracking[2,38,39].

1.3.4. Electrochemical potential

Agrawal et al[40] did extensive polarization studies on Fe-Ni-Cr alloys in sodium hydroxide solutions. They found that all Fe-Ni-Cr alloys exhibit active/passive behavior. They examined the effect of temperature and caustic concentration on the free corrosion potential as well as the influence of alloying additions on the corrosion resistance.

Unlike mild or plain carbon steels, which are susceptible only over a narrow range of potentials[10,41], rotor steels are susceptible to caustic SCC over a broad range of potentials[34,37]. Shalvoy et al[37] found the critical potential ranges in 40%NaOH to be between -850 to -600mV$_{SHE}$ and above +150mV$_{SHE}$.

Bandyopadhyay[42] found cracking at -350mV$_{SHE}$ and at -750mV$_{SHE}$ in 9M NaOH. The former potential is the transpassive region of the polarization curve and the later is near the active to passive transition. At the potential of -350mV$_{SHE}$ where SCC of mild steel does not occur[43], the segregation of phosphorus to the prior austenite grain boundaries (temper embrittlement) is suggested to cause the decrease in SCC resistance in rotor steels. McMinn et al[2] did SCC tests at the free corrosion potential and found cracking in concentrated and diluted sodium hydroxide solutions, pure water and carbonated water. All tests were conducted in aerated and deaerated solutions.

1.3.5. Material composition

Since the microstructure of most rotor steels is bainitic, the emphasis for SCC investigation lies on the alloy composition. A key role for the resistance to SCC seems to lie in the alloy impurities.

Bandyopadhyay et al[31,42] studied the effect of Mo and P when segregated to the prior austenite grain boundary. They observed severe caustic cracking in the transpassive region with the presence of P and Mo grain boundary segregation, which was explained by the incorporation of Mo and P in the growing oxide film. Both elements enhance the growth kinetics of the oxide film and decrease its ductility. The presence of Mo in P-free steels, however, shows no detrimental effect. The effect of silicon and manganese is not completely clear yet. Parkins et al[44] suggest that elements that form carbides like Ti, Cr and Mn are beneficial to SCC resistance, whereas especially Si (usually found in the ferrite in preference to the carbides), seems to be detrimental. Also, Bandyopadhyay[45] relates carbide composition and carbide morphology to the SCC resistance.

McMinn et al[2] found that the lowering of the nickel content in rotor steels gives an improvement in SCC resistance. However, this effect was only observed in specific environments and cannot be used as a general conclusion. They suggest that the yield strength of the material has a greater effect on SCC behavior than the alloy composition. Greenfield et al[36] tested rotor steels with varying Ni, Mo and V contents and found no significant difference in SCC behavior.

Besides the influence of microsegregation at grain boundaries, Parker[32,46] points out the effect of sulphide

inclusions on the SCC behavior of steels. Sulphides act as major cracking initiators particularly in acidic solutions. The composition of the inclusions is very important because it determines their solubility in a certain environment. Parker found that inclusions have a pronounced effect in very dilute environments whereas in aggressive environments they may be of secondary importance. However, Roberts[36] tested rotor steels in pure steam and water and found no difference in cracking behavior of samples taken from heavily segregated areas (centre portion of forging) and samples taken from zones with no segregation.

At present, there is only very little agreement about the influence of different alloying or impurity elements on the SCC of rotor steels.

1.4. Present objectives

The principal objective was to study and correlate the SCC behavior of three different rotor steels with their electrochemical polarization behavior in environments that simulate the steam condensates present in steam turbine operation i.e. carbonate and sodium hydroxide solutions. A second objective was to correlate inclusions, principally CaS and MnS in remelted and doped rotor steel, with corrosion behavior of the steel. In this manner, new information may be generated to assist in the mechanistic understanding of reported failures of cracked steam turbine rotors and SCC results obtained in other laboratories.

II. EXPERIMENTAL

2.1. Material

For our experiments three different rotor steels were available, their designation is "A", "R" and "O" - steel.

2.1.1. Chemical composition of the materials

Steel "A" is a 3.5%NiCrMoV - steel with very low concentration of impurity elements. Also, the manganese and silicon content are kept considerably below the regular concentration.

The reference steel "R" has a composition of a regular 3.5%NiCrMoV - steel used in commercial LP steam turbines. According to the ASTM Norm[47] it represents an A470-Class5 rotor steel.

The 1%CrMoV steel "O" is classified after the ASTM Norm as A470-Class8 rotor steel.(Typical for HP turbines)

Figure 1 on page 14 gives the composition of all three steels. All concentrations are given in wt% and are provided by the producers of the materials[15].

Figure 1: Chemical composition (wt%) of the rotor steels
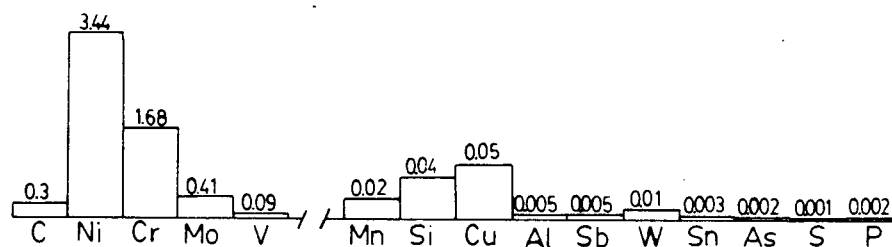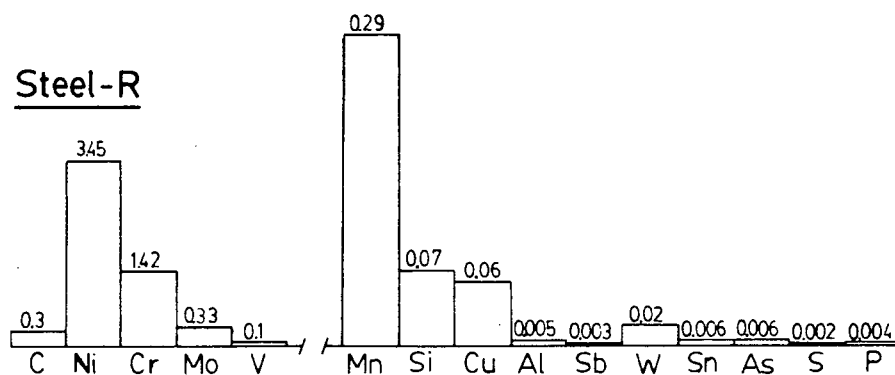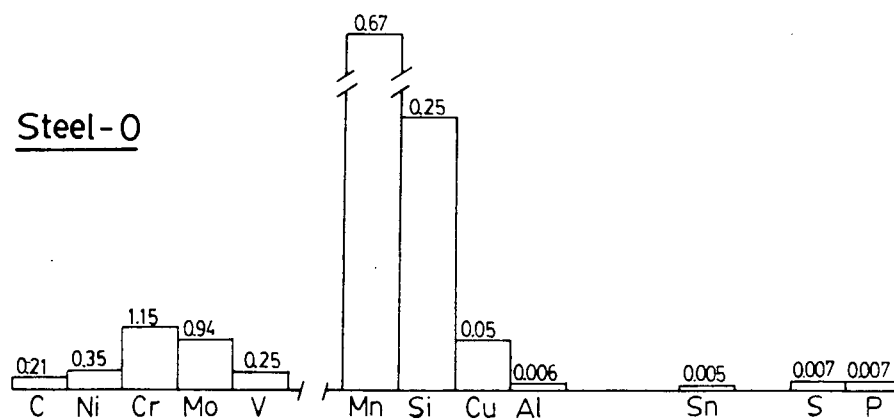
2.1.2. Heat treatment

The heat treatment of the steels "A" and "R" given below was conducted by the manufacturer and was not further changed for our investigations.

Steel "O" was received in the hot-rolled and air-cooled condition and was not further heat treated for our experiments.

Figure 2: Heat treatment of steels "A" and "R"

Steel-A
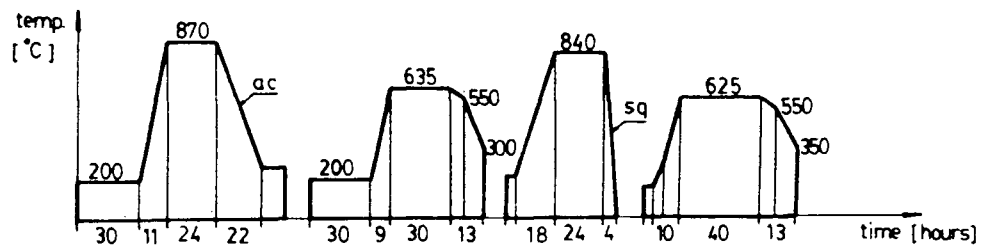
Steel-R
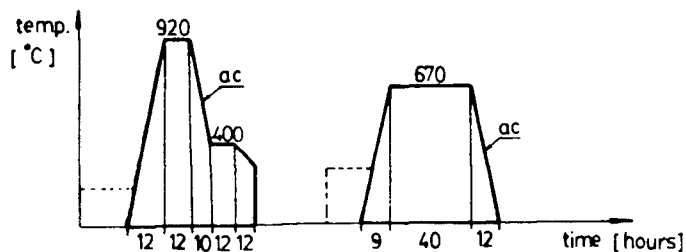
ac: air cooling

sq: spray quenching (water)

2.1.3. Sampling of rotor material

Steel "A" and "R" were received as discs which were sectioned from big rotor forgings. Steel "O" was available as a long round shaft. Figure 3 below shows the locations where specimens were sectioned from the forgings. The description of the notched samples is as follow:

First letter: direction normal to the fracture plane

Second letter: direction of crack propagation

"L": length, direction of metal working

"C": chord of cylindrical cross section

Figure 3: Sampling map
Steel-"O"

Specimen:

Fracture mechanics

Charpy-V

Slow strain rate

"Centre"

Microstructure, Hardness

"Surface"
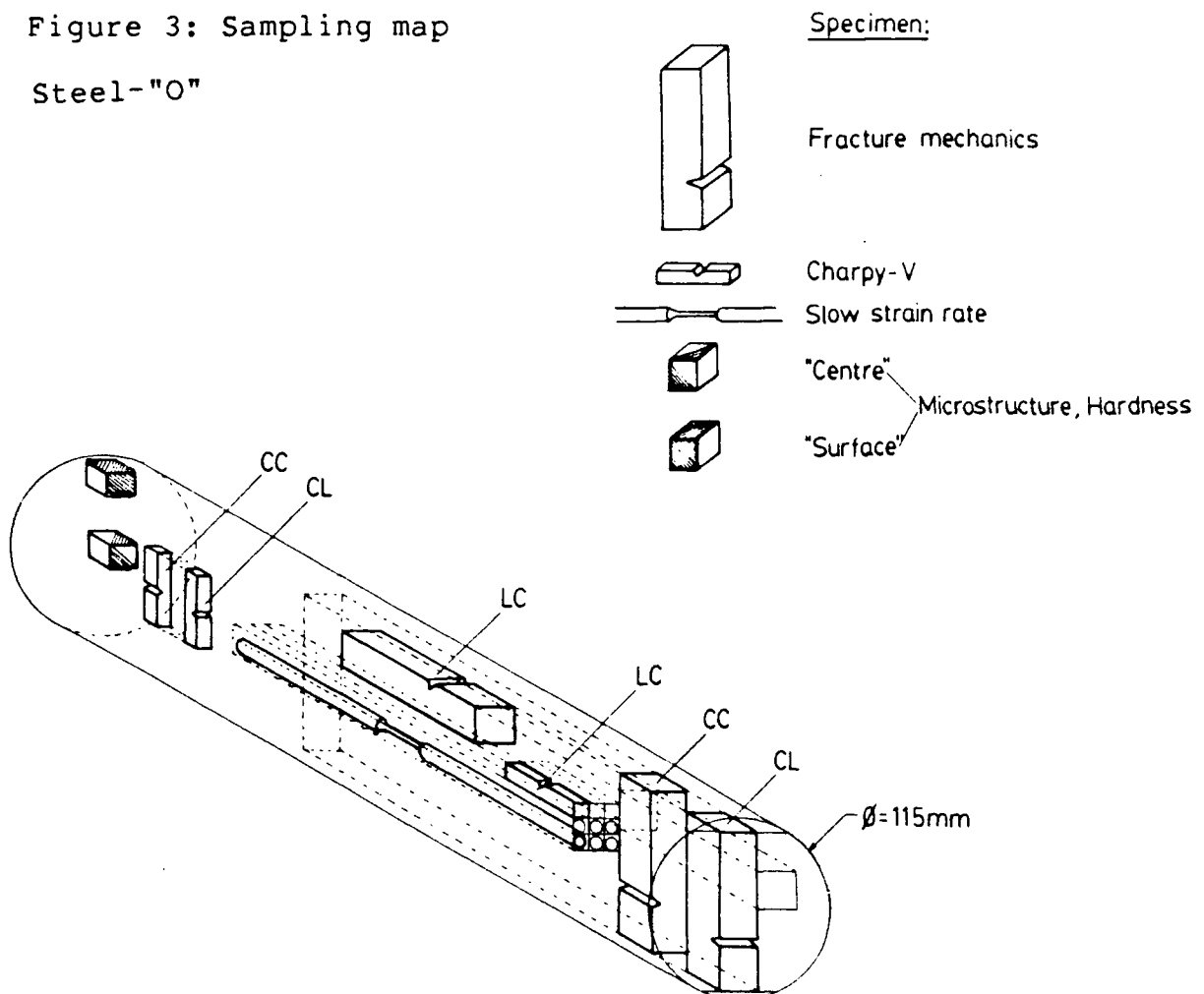
Figure 3: cont'd:
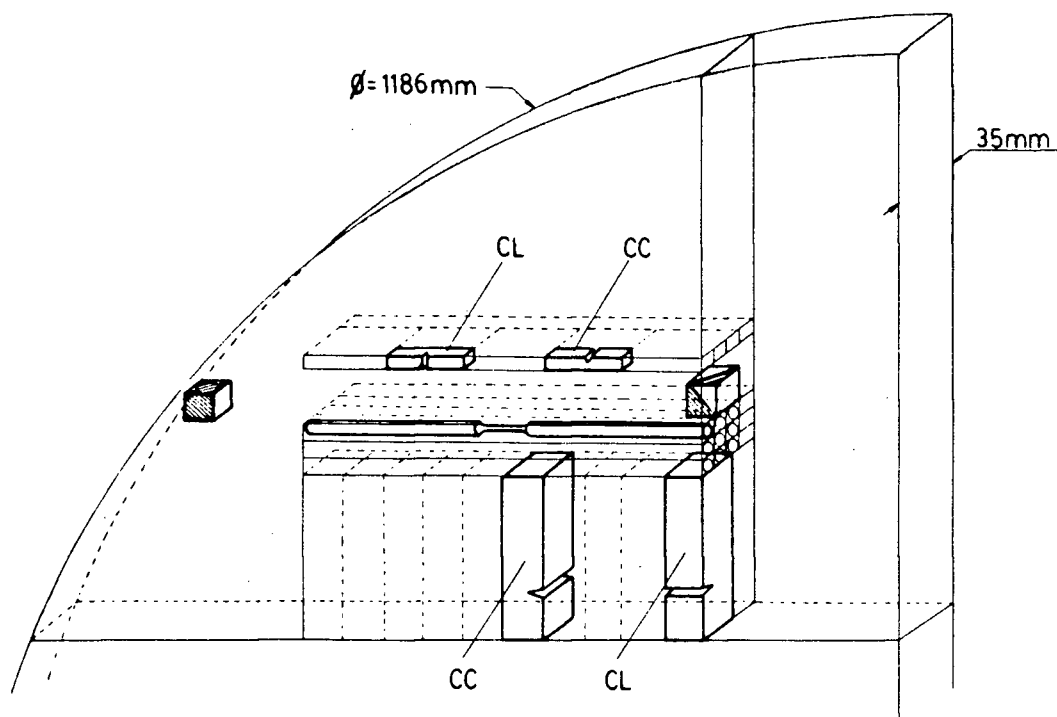
Steel-"A"

Steel-"R"
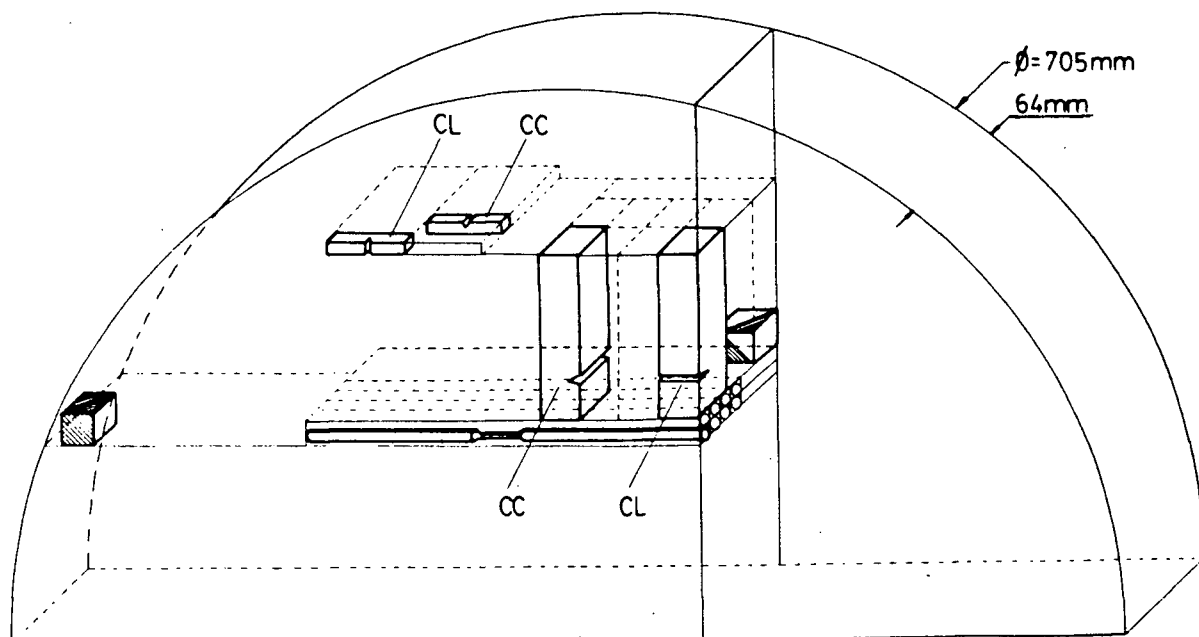
2.1.4. Mechanical properties

Tensile-, hardness-, and charpy-V-notch tests were performed on all three steels at room temperature. To check the influence of temperature on the plastic deformation behavior, (slow) tensile tests were also conducted at 100°C and 160°C. (A hot oil bath was chosen as the inert test medium)

Table I below summarizes the results of the mechanical tests.

Table I: Mechanical properties

Material/Temp.	Yield Strength (MPa) *1)	Ult.Tensile Strength (MPa) *1)	Elongation to Failure (%) *1)	Hardness (centre) (R_c) *2)	Hardness (surface) (R_c) *2)	Charpy-V (J) *3)			Fracture Toughness (MNm$^{-3/2}$) *4)		
						CC	CL	LC			
Steel "A" 3.5%NiCrMoV											
RT	725	853	17.1	22.5	26.0	133	133	--	250		
100°C	645	771	15.0	--	--	--	--	--			
160°C	637	779	15.8	--	--	--	--	--			
Steel "R" 3.5%NiCrMoV											
RT	727	838	16.7	25.0	26.0	137	137		250		
100°C	712	810	14.0	--	--	--	--	--			
160°C	670	797	15.7	--	--	--	--	--			
Steel "O" 1%CrMoV									CC	CL	LC
RT	931	1100	13.2	34.7	35.6	6	6	20	43	43	55
100°C	924	1072	11.0	--	--	--	--	--			
160°C	839	933	11.0	--	--	--	--	--			

*1) For each temperature only one test was performed. The samples had a gage length of 25.4mm and a diameter of 4.0mm. Tensile tests at room temperature were run at $\dot{\varepsilon}=3.3\cdot10^{-4}s^{-1}$. At $100^{\circ}C$ and $160^{\circ}C$ $\dot{\varepsilon}$ was $3.3\cdot10^{-5}s^{-1}$.

*2) Hardness measurements were taken at locations indicated on the sampling map (page 16,17)

*3) With steel "O" the toughness was measured in the CL, CC and LC directions. Because of the thin disc shape only CL and CC directions were investigated on steel "A" and "R".

*4) Fracture toughness values of steel "A" and "R" are literature data[50]. Steel "O" values were obtained by breaking SCC samples in air.

Steels "A" and "R" showed very similar properties. The hardness of "A" in the centre region was lower than in the R- steel. This was due to a different cooling rate of each forging. The 1%CrMoV steel "O" showed higher yield and ultimate tensile strength but a little less ductility. However, the toughness of "O" was very much lower than in the two NiCrMoV-materials. This correlated with the considerably higher hardness of the 1%CrMoV steel.

The toughness of "O" was strongly dependent on the direction of the fracture plane. This observation can be explained with the presence of a rolling texture and the elongated manganese sulphides in the rolling direction. For the steels "A" and "R" no direction dependence of the toughness was assumed since neither rolling texture nor elongated inclusions were present.

With increasing test temperature, both yield strength and ultimate tensile strength decreased. However, this could

also be due to the faster strain rate at room temperature. The effect of temperature on the percentage elongation to failure was rather minimal. (More tests would be necessary to confirm these results.)

On the stress strain curve, no strain aging phenomena was observed during plastic deformation at the elevated temperatures investigated.

2.1.5. <u>Production of CaS and MnS rich steels</u>

1.5 kg charges of the ordinary 3.5%NiCrMoV - steel "R" were remelted in a vacuum induction furnace. Sulphur was added to the charge in the form of FeS powder. The melting was conducted in an argon atmosphere (1.1atm). Calcium granulates and Manganese oxide powder were immersed into the superheated melt ($\approx$1600°C) with a plunger. After the Calcium or Manganese additions, the steel was cast into a chilled steel mold.

Additions per charge:
For CaS-rich steel: 20gms Ca, 1gm FeS
For MnS-rich steel: 20gms MnO, 1gm FeS
The casting was hot rolled at 950°C. In 8 passes a 50% reduction was achieved. Afterwards, the heat treatment previously described for steel "R" (page 15) was conducted.

2.2. Microstructure / carbides / inclusions

For viewing the very fine microstructure of the bainitic steels, both a light microscope and a transmission electron microscope (TEM) were used. The locations for the microstructural investigations are indicated on the sampling map (page 16).

2.2.1. Optical microscope investigations

The samples were ground with SiC paper down to 800 grit. For the final polishing finish, diamond paste down to 1/4 μm grade was used. When inclusions were examined, alcohol was used as polishing lubricant and coolant instead of water.

The microstructure was revealed with a picric acid etchant: 200ml ethanol, 20gm picric acid and a few drops of conc. HCL. Examination and photography were conducted with a "Zeiss-Ultraphot" optical microscope.

2.2.2. Steel "A" (3.5%NiCrMoV super clean)

The microstructure of the rotor forging was investigated at two locations. One was a few centimeters below the surface and the other one 23 centimeters further towards the centre. Typical microstructures are shown in Figures 4 and 5 below.
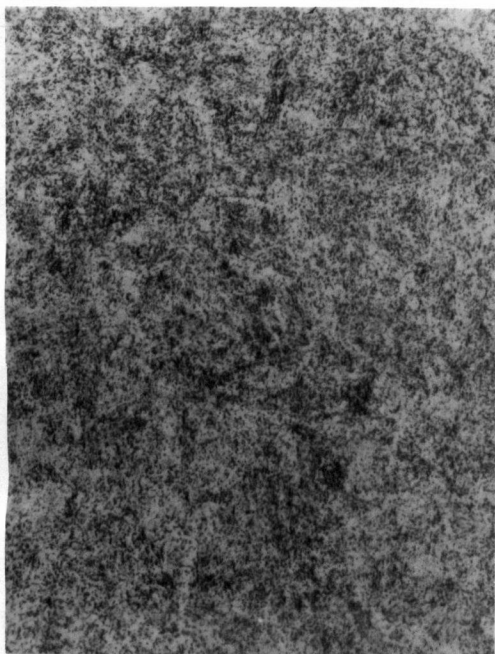
Figure 4:

Microstructure of steel "A", centre region

Bainite, carbide particles in ferrite matrix
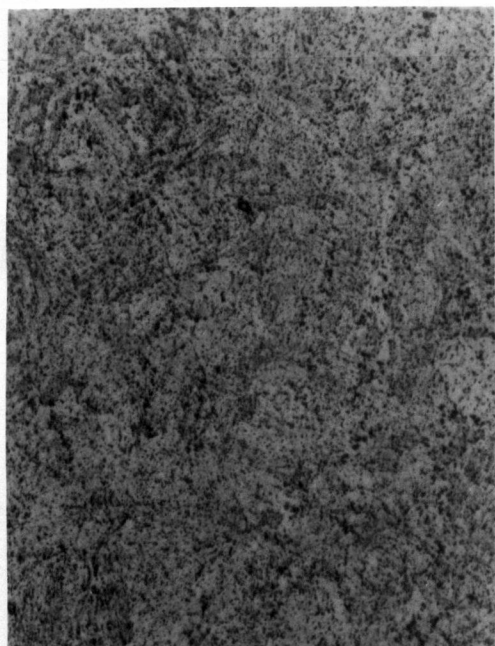
Mag.: 600x, etched

Figure 5:

Microstructure of steel "A", surface region

Mag.: 600x, etched

From the Figures 4 and 5 (pg. 22), it can be seen that the bainitic microstructure was essentially the same at both locations. Also, no difference was observed between the radial and the longitudinal direction at the same locations. However, it was observed that in the centre region the carbides were more numerous and coarser. This could be explained with the faster cooling rate at the surface region. Neither Picric acid nor Nital etching revealed prior austenite grain boundaries. No further metallographic experiments were undertaken to determine the prior austenite grain size. However, from fractography studies, a size below 30 μm could be estimated.

From the production report[48] of this steel, it is further known that throughout the whole rotor cross-section a bainitic microstructure was present.

2.2.3. Steel "R" (3.5%NiCrMoV)

Similarly to steel "A", no difference in microstructure was observed between regions near the surface and 23 cm. below the surface towards the centre. According to Figures 6 and 7 (page 24), it also seems that the size and distribution of carbides were very much the same in both locations. This observation is supported by the hardness measurements which also showed no difference in the two regions. Even with different alloy compositions and heat

treatment, both steels "A" and "R" appeared to have a very similar microstructure.

Figure 6:

Microstructure of steel "R", centre region

Bainite, fine and coarse carbides in ferrite matrix
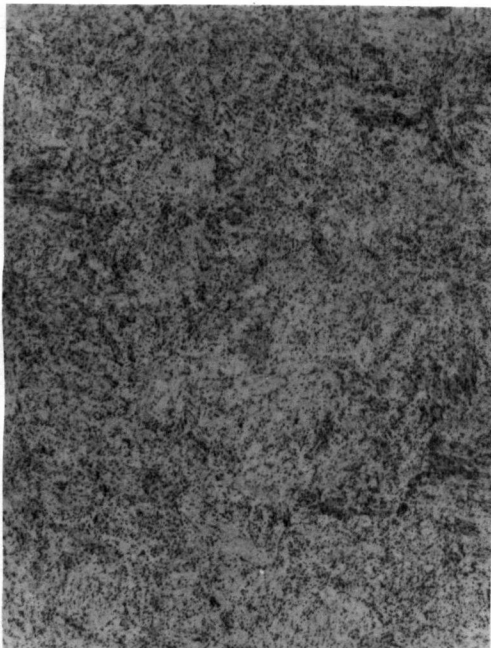
Mag.: 600x, etched

Figure 7:

Microstructure of steel "R", surface region

Mag.: 600x, etched

2.2.4. Steel "O" (1%CrMoV)

According to the continuous cooling transformation diagram[49] of a 1%CrMoV-steel (similar to the one investigated), air cooling of the rotor steel "O" should have resulted in a bainitic microstructure with possibly some ferrite present. Photomicrographs taken at different locations in the material again did not show any major difference in structure between surface and centre regions. However, at low magnification a slight rolling texture could be observed in the longitudinal direction. (See Fig.8) At higher magnification a coarser and less homogeneous carbide distribution is visible compared to the one found in the "A" and "R" steels. (See Fig.9)

Figure 8:

Microstructure of steel "O", radial direction with rolling texture

Bainite, bright areas are ferrite, darker areas carbides + ferrite, rolling texture visible as horizontal bands (slightly darker)

Mag.: 120x, etched
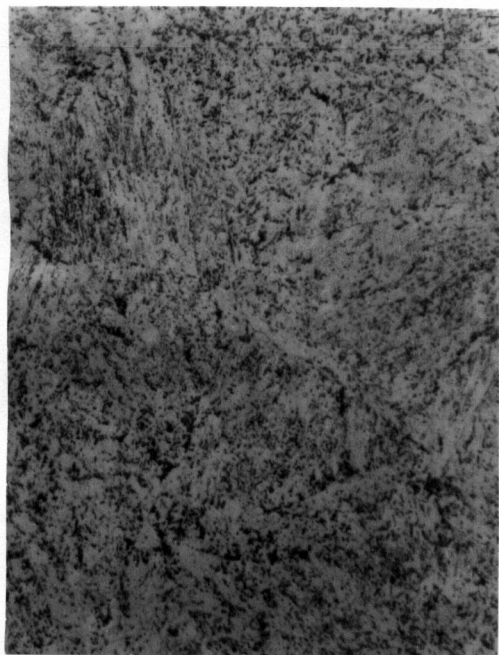
Figure 9:

Microstructure of steel "O"

Coarse carbides and ferrite

Mag.: 600x, etched

2.2.5. Transmission electron microscope (TEM) investigations

Discs for TEM studies were sectioned from unstrained slow strain rate test pieces using a spark machining technique. The discs were 3mm in diameter and 2mm thick and were carefully ground on SiC paper to a thickness of about 0.1mm. (It was tried to keep the mass of the samples as small as possible because of their disturbing effect on the magnetic field in the microscope lens system).

The final electrochemical thinning was conducted with a "Struers polipower" jet polishing device. A mixture of 20 percent perchloric acid in methanol was used as electrolyte. The potential was held at about 20-22 Volts with a medium flow rate setting. The electrolyte temperature was maintained at 25°C.

Examination and photography were conducted with a Hitachi H800 scanning transmission electron microscope. For a qualitative chemical analysis of matrix and carbides, an Ortec - energy dispersive X-ray (EDX) analyzer was used.

2.2.6. Steels "A" and "R"

In the light microscope steel "A" and "R" showed the same microstructure. However, the TEM studies revealed some differences. The Figures 10-13 on page 29 (all electron micrographs taken at about the same magnification) show that the ferrite grains in steel "R" are very narrow and needle-like, whereas in "A" a rather irregular shape is present. Also, the carbides in "R" seem to vary in size more than in steel "A".

The Figures 14 and 15 on page 30 show that inside the ferrite subgrains of steel "R", carbides are precipitated at an angle to the longitudinal direction. In both steels, bigger carbides were often located along subgrain boundaries

and possibly along prior austenite boundaries.(Figures 16 and 17)

According to the literature[51,52,53], steel "R" represents the microstructure of a "lower bainite" whereas "A" has features typical of "upper bainite".

2.2.7. Steel "O"

This steel had a much less uniform microstructure compared with "R" and "A". On Figure 18 (pg. 32), bainite and ferrite are visible. The very small particles in the ferrite may be carbides or could be some sort of contamination from the polishing solution. The electropolishing of this steel was not as satisfactory as for the other two steels. The structure of the bainite would suggest "upper bainite". On the boundaries between ferrite and bainite rather large, elongated carbides were present. (See Figures 19,20 on page 32)

Figure 10:

TEM-picture, microstructure of steel "A" with carbides and subgrains

Bainite, bright areas are ferrite, dark particles carbides
Mag.: 4,000x

Figure 11:

TEM-picture, microstructure of steel "A" with carbides and subgrains

Mag.: 3,500x

Figure 12:

TEM-picture, microstructure of steel "R" with elongated subgrains

Fine, needle like and round carbides, bright area in the centre is a hole in the sample
Mag.: 4,000x

Figure 13:

TEM-picture, microstructure of steel "R" with carbides and subgrains

Mag.: 4,000x
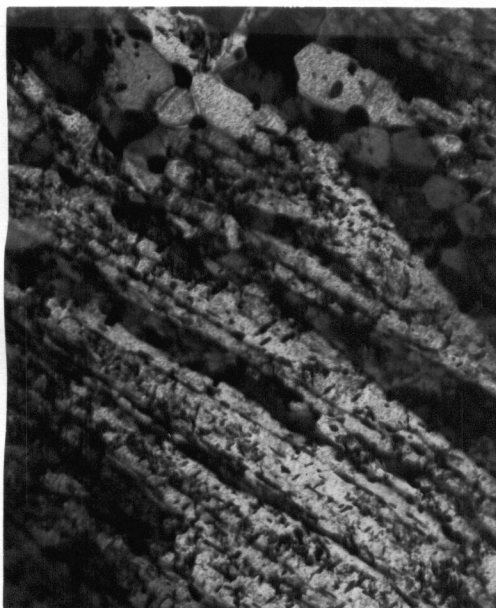
Figure 14:

TEM-picture, steel "R",
elongated carbides inside
subgrains

Small carbides are not aligned
with the long subgrain axis

Mag.: 12,000x

Figure 15:

TEM-picture, steel "R", carbides
inside subgrains and at grain
boundaries

Mag.: 9,000x
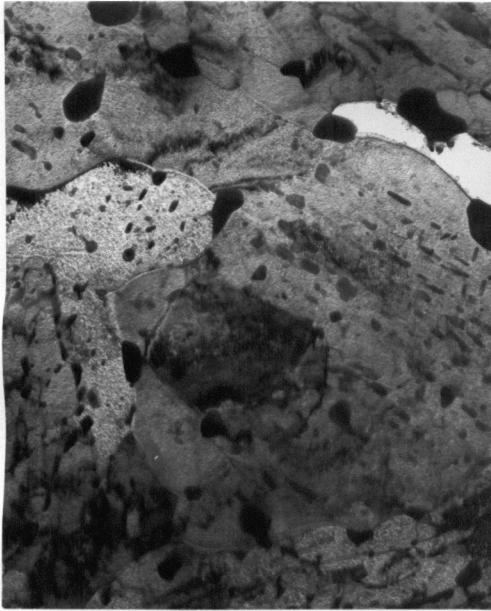
Figure 16:

TEM-picture, steel "R", carbides
at subgrain boundaries

Mag.: 15,000x

Figure 17:

TEM-picture, steel "A",
elongated carbides at subgrain
boundaries

Carbides aligned with the long
subgrain axis, fine dark lines
are dislocations

Mag.:40,000x
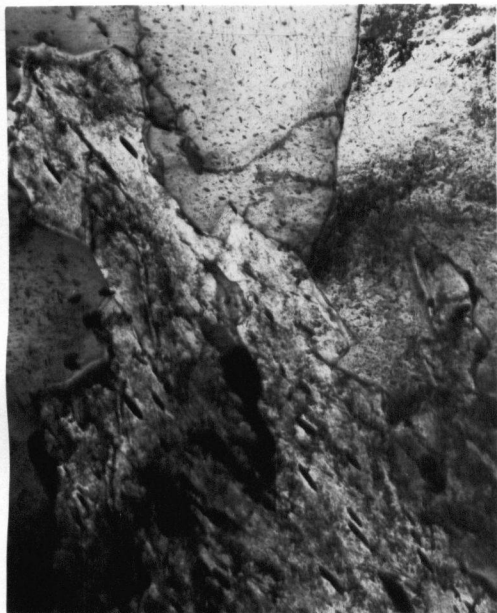
Figure 18:

TEM-picture, steel "O", microstructure with ferrite and bainite

Carbides are aligned in one direction inside the bainite grain. Small particles inside the ferrite grain may not be carbides, but could be a contamination from the electropolishing

Mag.: 8,000x

Figure 19:

TEM-picture, steel "O", big carbides at subgrain boundaries

Ferrite and bainite grains
Mag.: 5,000x

Figure 20:

TEM-picture, steel "O", carbides inside grains and at grain boundaries

Big elongated carbides at the grain boundary to the left
Mag.: 6,000x

2.2.8. Qualitative carbide analysis by EDX

All carbides were iron carbides with different contents of alloying elements. In steel "A" and "R" no major difference in composition could be detected between big carbides located at the grain boundaries and small carbides in the interior. However, all carbides in "A" and "R" seemed to be enriched in the alloying elements Mo, V and Cr. In steel "O", most carbides were enriched in Cr only, but to a lesser degree than in steel "A" and "R". However, the long, big grain boundary carbides of "O"-steel were enriched in Cr and Mo. Caution must be exercised, however, because these X-ray analyses were only qualitative and did not allow a more detailed interpretation. Figures 21 and 22 below show an example of an EDX analysis on steel "R".
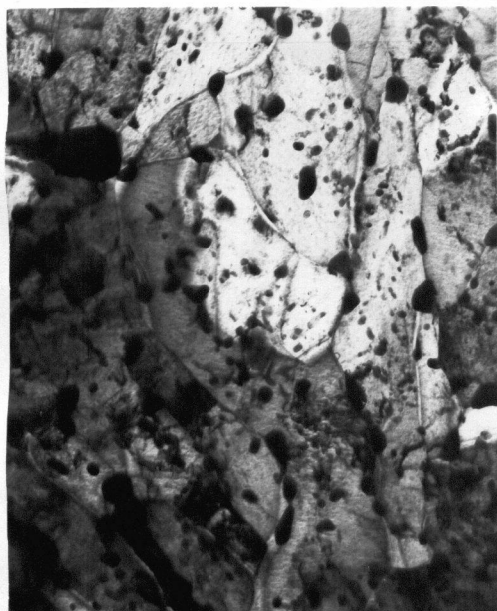
Figure 21:

TEM-picture, steel "R", locations for EDX-analysis

Big carbide in the top left corner, matrix analysis in a carbide free zone

Mag.: 15,000x

Figure 22 : EDX-analysis, steel "R", matrix and carbides.
Qualitative analysis, peak hight not directly proportional
to element contents.

Enrichment of Mo, V, and Cr in the carbides

PRESET:LT=   100S   DEAD TIME: 8%   COUNTS/SECOND: 465
FULL SCALE: 1K LINEAR   0-10 KEV   10 EV/CH

MATRIX

FeKα

FeKβ

NiKα

0.00   2.56   5.12   7.68   10.23

PRESET:LT=   100S   DEAD TIME:13%   COUNTS/SECOND: 280
FULL SCALE: 1K LINEAR   0-10 KEV   10 EV/CH

CARBIDE

CrKα   FeKα

MoLα   V Kα CrKβ   FeKβ

0.00   2.56   5.12   7.68   10.23
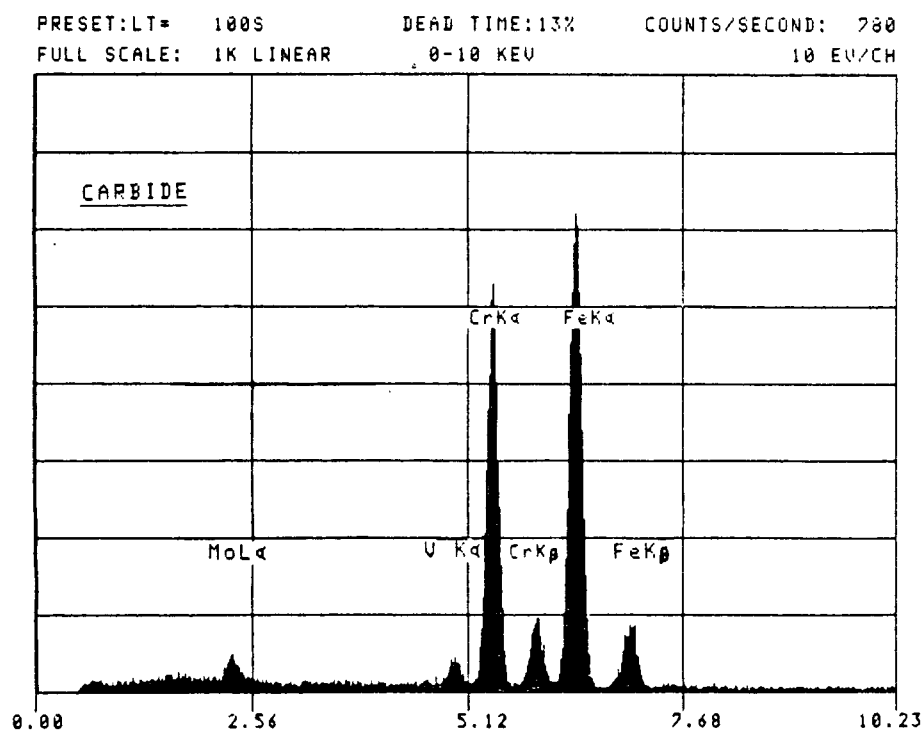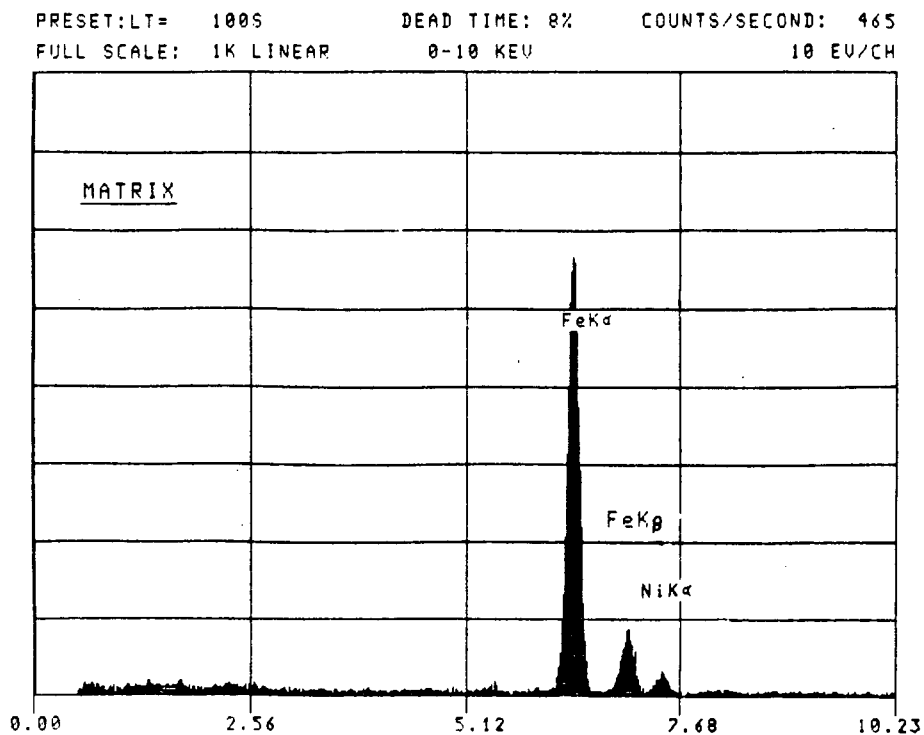
2.2.9. Electron diffraction of carbides

Electron diffraction studies were attempted in order to characterize the carbides in more detail. However, because of the very strong effect of the sample matrix on the magnetic field of the microscope lenses it was very difficult to analyze single carbides with the tilt - specimen holder. To avoid these problems, the extraction replica method would have been preferable but was not employed in this project. Attempts were made to obtain ring patterns from areas containing a multitude of carbides with little success, due to the variety of carbides paterns which were present. Figures 23 and 24 illustrate patterns from single carbides and multiple carbides. In Figure 23 the pattern cannot be indexed as Fe_3C, but may represent an orthorhombic structure analogous to Cementite.
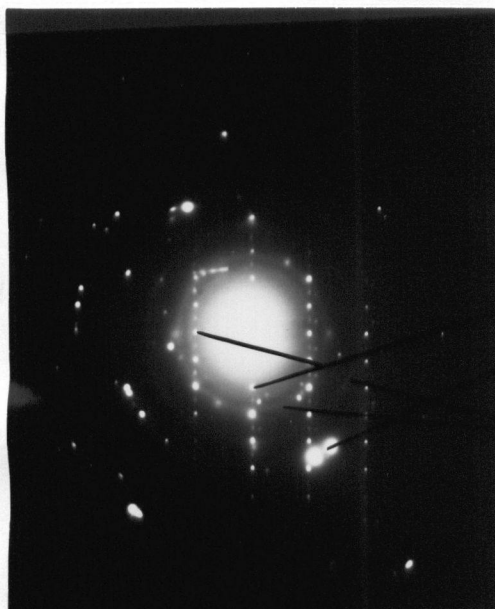
Figure 23:

Electron diffraction pattern of a carbide, steel "R"

Carbide

αFe

Fe-oxides

(400) Fe_3O_4
(202) Fe_2O_3

(200) α-Fe
(211) α-Fe

Figure 24:

Electron diffraction pattern
of several carbides, steel "R"

(110) α-Fe

(440) Fe_3O_4
(300) Fe_2O_3

Carbides

(311) Fe_3O_4
(110) Fe_2O_3
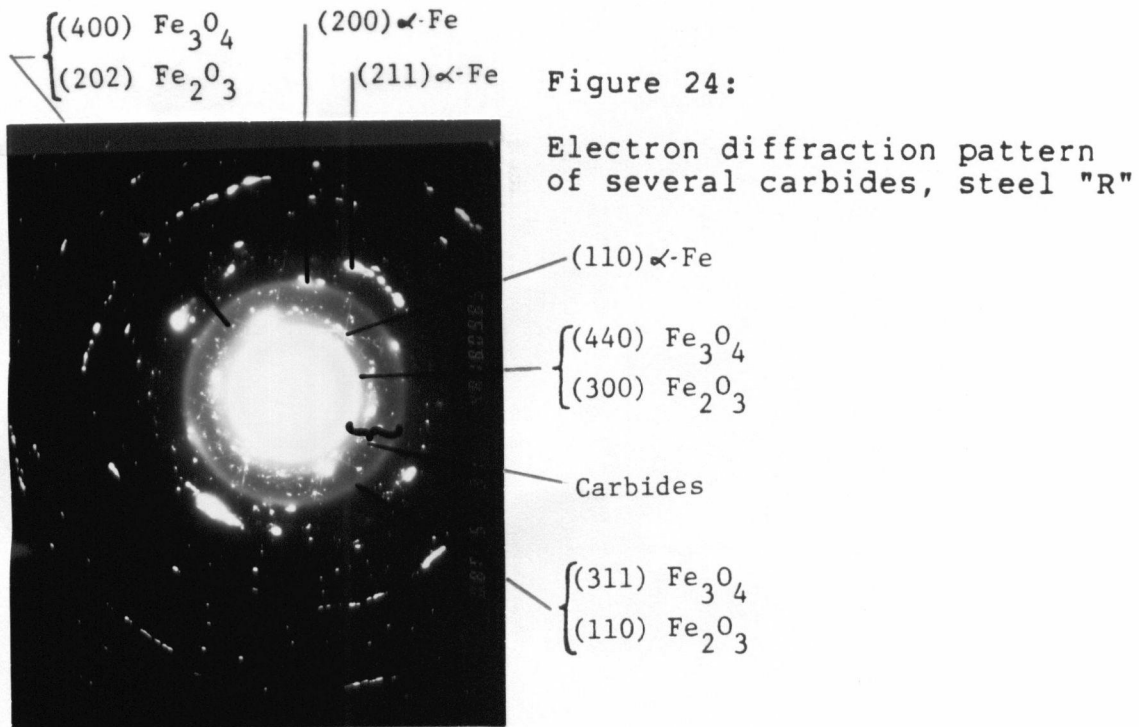
Bandyopadhyay et al[45] conducted studies on the composition of carbides in rotor steels. In a tempered bainitic microstructure they found M_3C, M_7C_3 and M_2C carbides. The M_3C type were bigger carbides preferentially located along grain boundaries. The M_7C_3 and M_2C particles were found to be very small with diameters below 0.1 μm. The M_3C were found to be iron carbides enriched in Cr up to 25%, Mo up to 4% and V up to about 2%. The M_7C_3 contained mainly iron and chromium, whereas M_2C represented Mo,V-carbides. This enrichment of alloying elements in the carbides supports our qualitative findings with the EDX analysis.

2.2.10. Inclusions

Since specifications for rotor steels are very tight on the content of impurity elements such as sulphur, the inclusions are very small and not very numerous. In this study no attempt was made to fully characterize the distribution and size of all inclusions present in the test materials. However, attempts were made to characterize typical inclusion types present in each of the three steels.

Steel A: The big inclusions were found to have a diameter of about 10μm. Most inclusions, however, were smaller than 3μm. At a few locations, very long and narrow particles were detected with a length up to 50μm. The shape of most inclusions was quite irregular with sharp corners. Round particles were rather seldom.

Qualitative investigations with an EDX analyzer attached to a scanning electron microscope (SEM) revealed the following data:

-Small round inclusions were calcium sulphides. Sometimes aluminum or silicon was detected in the centre of these particles, which most probably represents an oxide core (often observed in CaS-inclusions[54]). See Figure 25.

-Inclusions with sharp corners (often triangular shape) were composed mainly of Si, Al and Fe. Therefore they could be classified as oxides. See Figure 26.

-Long flattened particles could also represent oxides becouse they were also rich in silicon. See Figure 27
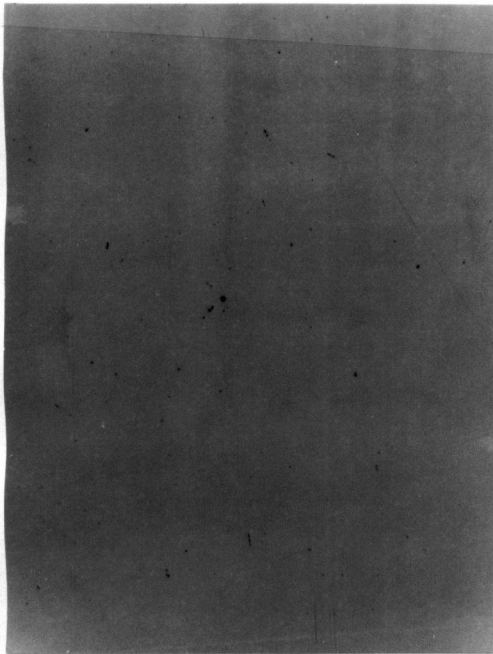
Figure 25:

Distribution of inclusions in steel "A"

Average inclusion appearance in the centre region

Mag.: 40x
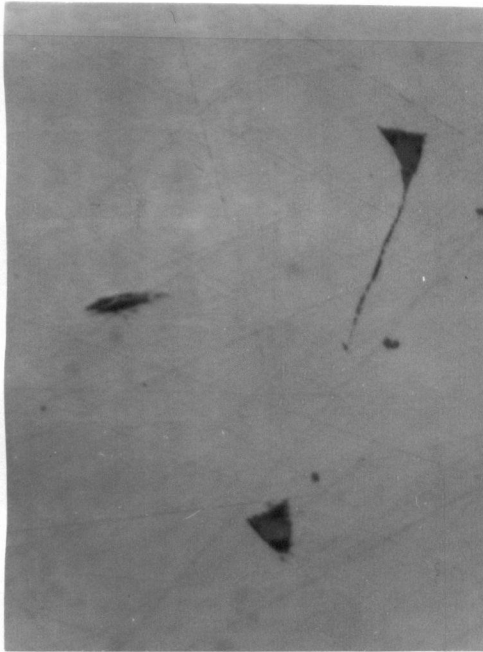
Figure 26:

Oxide inclusions in steel "A"

Mag.: 1,000x
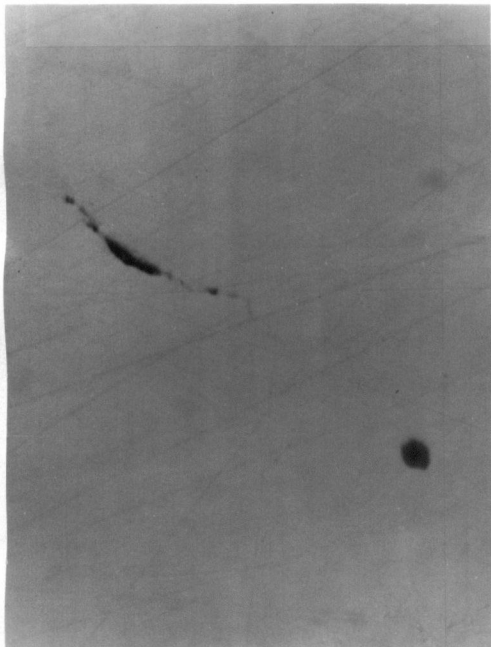
Figure 27:

Oxide and sulphide inclusions in steel "A"

Round particle is CaS

Mag.: 1,000x

Steel R: Compared to the "A" steel, "R" seemed to have fewer but bigger inclusions. Their shape was mostly round with diameters between about 10 and 20 µm. Also, a few smaller irregular shaped particles could be found.

With the EDX analysis, the big round inclusions could be classified as CaS with an alumina / silica core. The irregular shaped particles seemed to be exclusively silica inclusions. (See Figures 28-30)
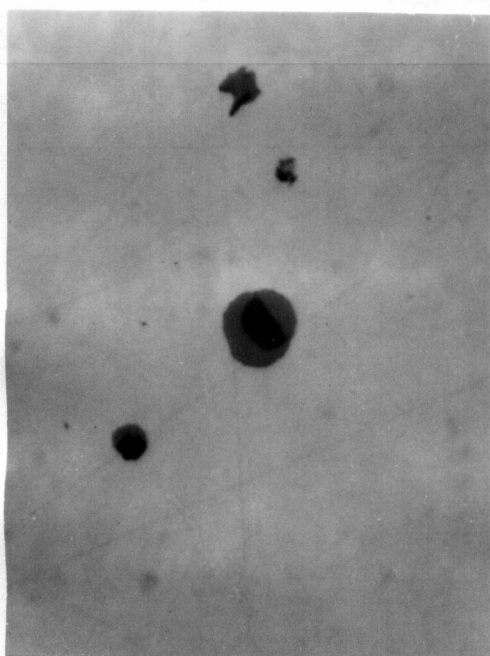
Figure 28:

CaS inclusions in steel "R"

Dark area in the centre of the
inclusion is an oxide core
Mag.: 1,000x
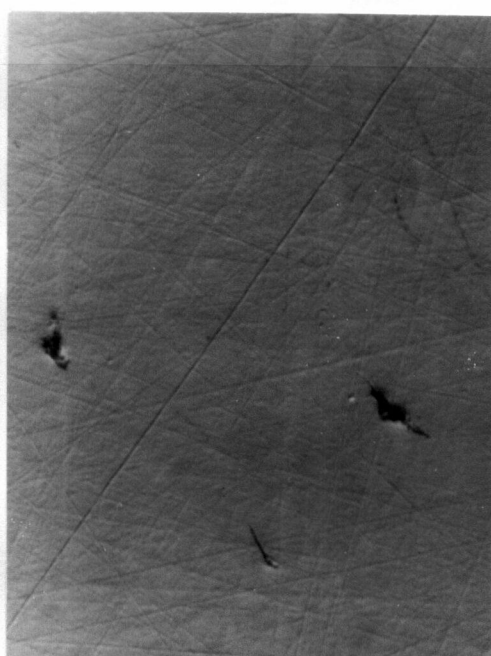
Figure 29:

Oxide inclusions in steel "R"

Mag.: 1,000x
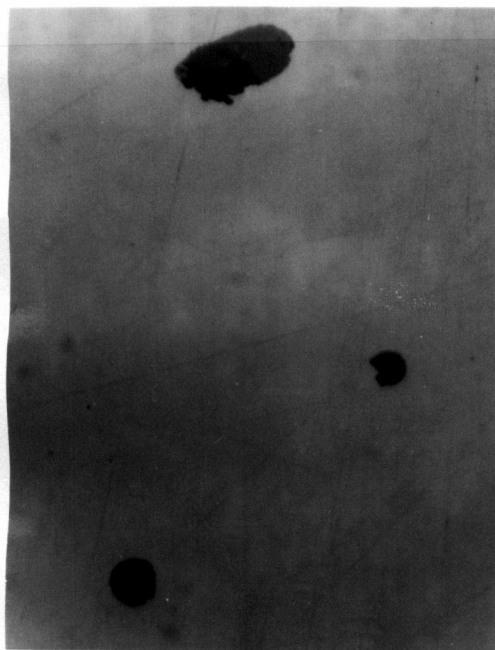
Figure 30:

CaS inclusions with oxide core, steel "R"

Mag.: 1,000x

Steel O: A completely different inclusion distribution was found in this steel. In the rolling direction long stringers of flattened inclusions were observed. Their length was generally 50μm but stringers composed of several aligned inclusions were a few hundred microns long. Their thickness was mostly below 10μm. In addition, only a few round inclusions could be found and their size was smaller than a few microns. Irregular shape oxide inclusions could only very rarely be detected. The composition of the elongated inclusions classified them as MnS. In a few MnS stringers, small particles (probably oxides) of Al and Si were found. (See Figures 31 and 32, pg. 42)
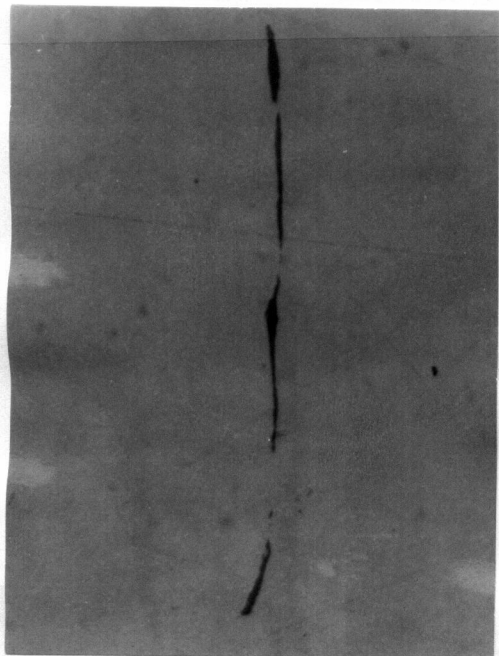
Figure 31:

Elongated MnS inclusions in steel "O"

Mag.: 1,000x
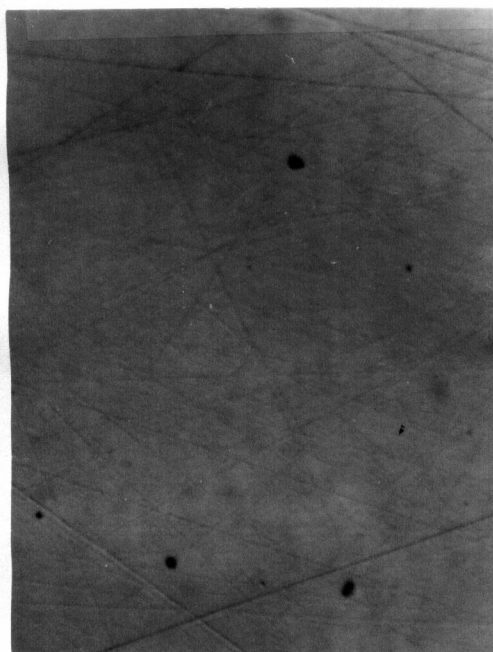
Figure 32:

Small round inclusions in steeel "O"

Not identified as sulphides or oxides

Mag.: 1,000x

Remelted steel "R" doped with inclusions, MnS and CaS.
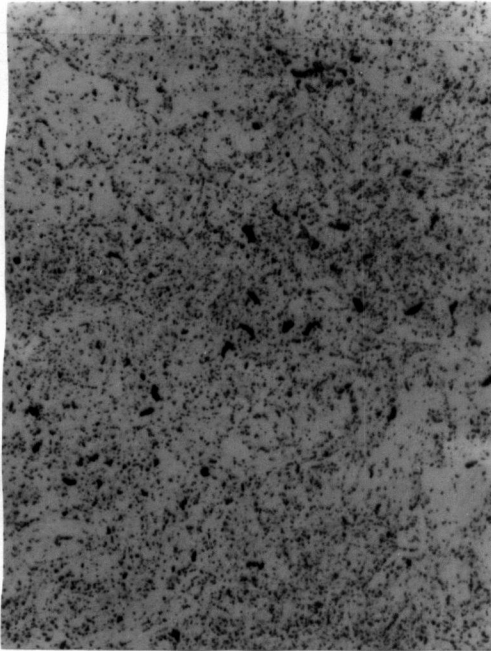
Figure 33:

Microstructure and inclusions
in CaS doped steel "R"

Black particles are etched away
inclusions, small particles
are carbides, most probably a
bainitic microstructure is
present

Mag.: 600x
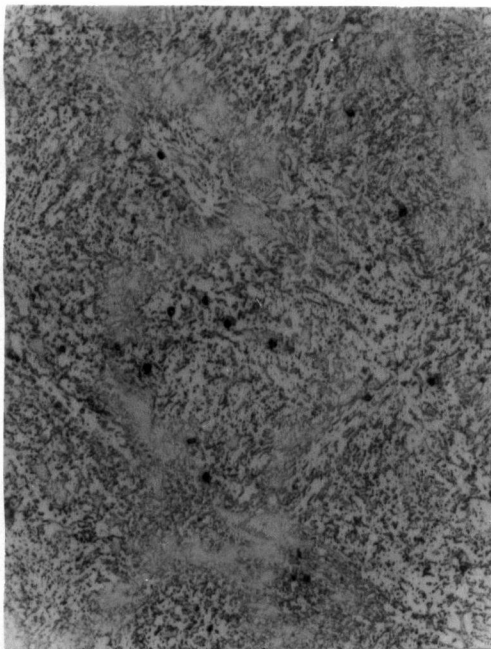
Figure 34:

Microstructure and inclusions
in MnS doped steel "R"

Big particles are etched away
inclusions, small particles
are carbides, microstructure
is not clearly identified,
(hardness is much lower than
in the CaS doped steel)

Mag.: 600x

2.2.11. Summary of microstructures

In "A" and "R" steels, a fully bainitic microstructure was observed. The 1%CrMoV-steel "O" showed a ferritic/bainitic structure.

Steel "A" showed a very uniform distribution of fine carbides whereas bigger carbides were found along the grain boundaries in steel "O".

The iron carbides in the 3.5%NiCrMoV-steels "A" and "R" were enriched in the alloying elements V,Cr and Mo. Steel "O" carbides showed only an enrichment in Cr, but to a lesser degree than in "A" and "R". Inclusions in steel "A" were mainly small oxides with a few CaS particles.

Steel "R" contained quite big CaS inclusions, but fewer oxides.

In the hot rolled steel "O", stringers of MnS inclusions were detected.

2.3. Electrochemical Polarization studies

Under free corrosion conditions (the metal specimen is immersed in a corrosive liquid and no external voltage is applied), both reduction and oxidation reactions occur on the metal surface. Therefore, both anodic and cathodic currents are present and equal in magnitude.

For studying corrosion processes it is often advantageous to separate anodic and cathodic reactions. This can be done by use of a voltage source to force the metal specimen to a potential other than the free corrosion potential. As a result of this "polarization", depending on the polarity, either the anodic or cathodic current predominates on the metal surface.

Experimentally one measures the corrosion current as a function of the applied potential measured with respect to a standard reference electrode. A record of potential versus log current is then called a polarization curve.

Figure 35, on page 46 illustrates how an experimentally obtained polarization curve can be explained as the synthesis of oxidation and reduction reactions.

Figure 35 : Illustration of a theoretical and experimental polarization curve
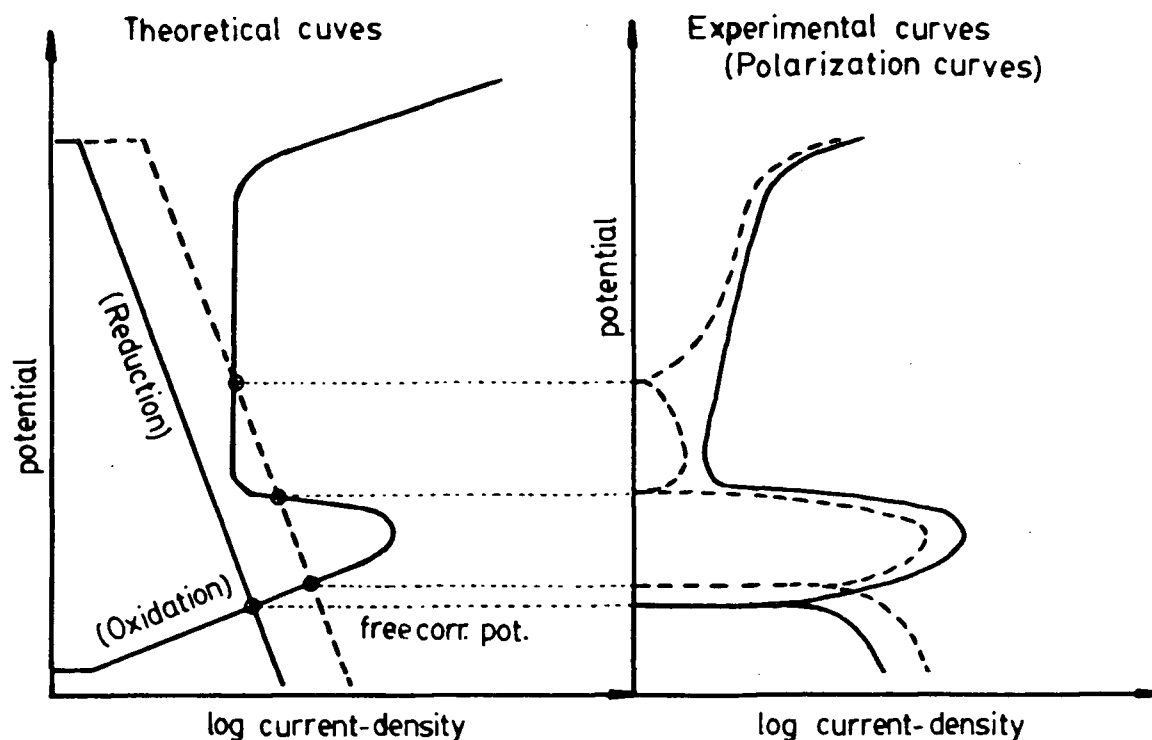
The position of oxidation and reduction curves is dependent on variables like temperature, concentration of species in solution or aeration and agitation of the solution. Therefore, the intersection point(s) of the oxidation curve with the reduction curve change(s) according to these parameters. This means that the free corrosion potential of a certain metal is strongly dependent on the environment conditions. Therefore, by imposing a certain potential onto the metal (in a given environment), one can simulate the free corrosion behavior of the same metal for a different environmental condition.

2.3.1. Sample preparation, test set up

Rods of approximately 4mm diameter and a length of 12cm were machined from all three materials. The samples were ground with SiC paper down to 800 grit and then electropolished in chromic-acetic acid. (1330ml acetic acid, 250 gms chromium trioxide, 70 ml H_2O). For the test the samples were wrapped in PTFE-Teflon tape so that only the bottom section with an approximate surface area of 2.5 cm^2 was exposed to the environment. Before each test, the samples were cleaned with acetone and alcohol.

The test cell (see Fig.36, pg. 49) was a 600ml PTFE beaker fitted with a PTFE lid. A heating mantle coupled with a temperature controller allowed adjustment of the solution temperature to $\pm$ 1°C. An approximate 3cm^2 platinum sheet in the solution served as counter electrode. A PTFE Luggin capillary was connected via a saturated KCl salt bridge to a standard calomel reference electrode. The reference electrode was kept at room temperature(23°C).

All solutions were made with reagent grade chemicals and distilled water. The solutions were purged with USP nitrogen before and during the test, except for tests with carbonate solutions, where CO_2 was bubbled through the solution. All tests were conducted at 95°C.

Investigations were conducted in the following solutions:

$CO_2 + H_2O$ $,p(CO_2)=1$ atm

$CO_2 + H_2O + NaHCO_3$ $,p(CO_2)=1$ atm , $c(NaHCO_3)=3.5 \cdot 10^{-3} M$ to 1M

$H_2O + NaHCO_3 + Na_2CO_3$ $,c(NaHCO_3)=1M$, $c(Na_2CO_3)=1M$

$H_2O + NaOH$ $,c(NaOH)=0.35M, 3.5M$

The pH range for the carbonate solutions at 95°C was from pH = 4.5 for the CO_2/H_2O solution up to about 9.5 for the 1 molar carbonate/bicarbonate solution. The sodium hydroxide solutions were in the pH range of 12-13.

All polarization curves were obtained with a Princeton Applied Research Model 350A Corrosion Measurement System. The potential scan rate was either 1mV/sec or 0.3mV/sec. All tests represent anodic polarization curves (scanning from negative to positive potentials). Each test was started at a potential at least 150mV more negative than the free corrosion potential in order to remove any oxide film on the sample surface. No attempt was made to correct for potential differences arising from liquid junction potentials in the salt bridge. (The correction would be in the order of a few millivolts[55]).

Figure 36 : Test set up for polarization studies
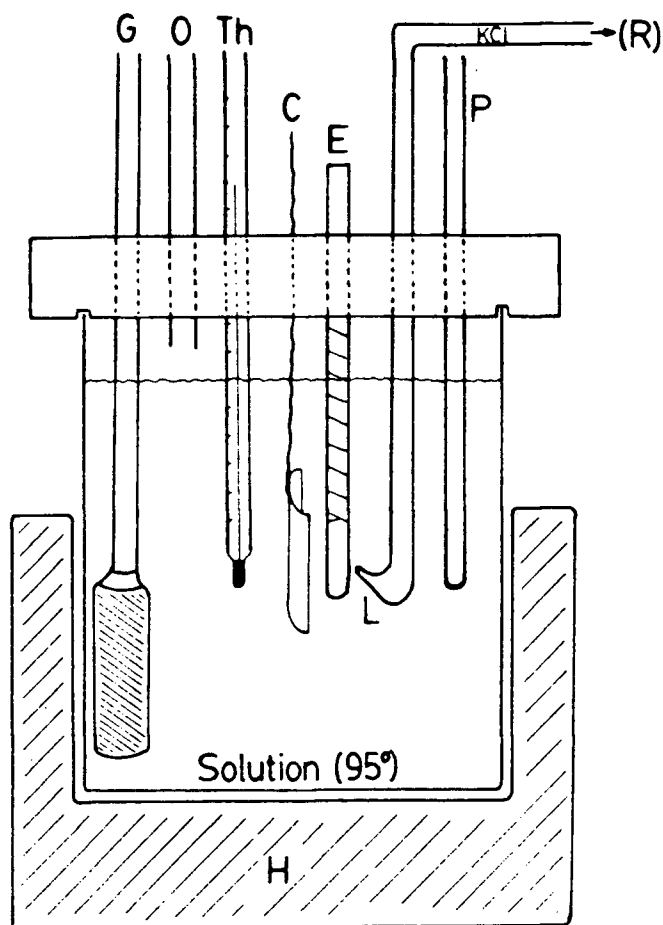
G : Gas inlet

Th: Thermometer

O : Gas outlet

C : Pt-counter electrode

E : Working electrode

R : Calomel reference cell

P : Temperature controller

H : Heater

L : Luggin capillary

2.4. Slow strain rate tensile test

The slow strain rate tensile test (SSRT) is often applied for determination of SCC sensitivity. The advantage of this method is the rapidity with which the test results can be obtained. The susceptibility to SCC is usually indicated by a reduction in mechanical properties. eg. lesser degree of necking before failure and the presence of secondary cracks in the gage section.

From the length of the secondary cracks and the test duration, average crack velocities can be calculated. In the present study only the time spent during plastic deformation was considered.

2.4.1. Sample preparation, test set up

All slow strain rate tensile tests were conducted with a vertically mounted Hounsfield tensometer fitted with a reduction gear and 12 rph synchronous motor. A crosshead speed of $4.4 \cdot 10^{-5}$mm/sec corresponded to a strain rate of $1.7 \cdot 10^{-6}$ sec^{-1}.

Rods of 25.4cm (10") length and 9.5mm (3/8") diameter were machined according to the sampling map (page 16). The gage section in the centre of the rod had a diameter of 4mm and a length of 25.4mm. Both ends of the tensile samples were threaded for mounting in tensile grips.

The gage section was ground with SiC paper and subsequently electropolished in chromic acetic acid. During the test, the sample was wrapped with PTFE tape and only the gage section was exposed to the solution.

The test cell (see Fig. 37, pg. 52) was a 600ml PTFE beaker, fitted with a rubber lid. A heating tape wrapped around the beaker coupled with a temperature controller allowed adjustment of the temperature to $\pm 1^\circ C$. A platinum sheet served as counter electrode. A PTFE Luggin capillary was connected via a salt bridge to a standard calomel reference electrode in the same manner as during the polarization tests.

Solutions were made up as described in 2.3.1. and the tests were all performed at $95^\circ C$.

The testing potentials were chosen according to the results of the polarization studies. Tests were conducted at the free corrosion potential, near and at the active peaks and in passive regions.

The potential was controlled with a Wenking Potentiostat, Model 70HP10 or an ECO Model 549 respectively. The usual test duration to failure was around 24 hours, depending on the steel and the environment.

After the test the two samples halves were cleaned in inhibited acid (3ml HCl, 4ml 2-Butyne-1,4 diol, 50ml H_2O) and one sample piece was electrolytically coated with nickel

and sectioned longitudinally (coating protects surface edge during mechanical polishing). On the polished longitudinal cross section, the corrosion attack and secondary crack length could be examined. The other half of the broken sample was used for scanning electron microscope (SEM) investigations on an ETEC-Autoscan.

Figure 37 : Set up for slow strain rate tensile tests

G : Gas inlet

Th: Thermometer

O : Gas outlet

C : Pt-counter electrode

E : Working electrode

R : Calomel reference cell

P : Temperature controller

H : Heater

L : Luggin capillary
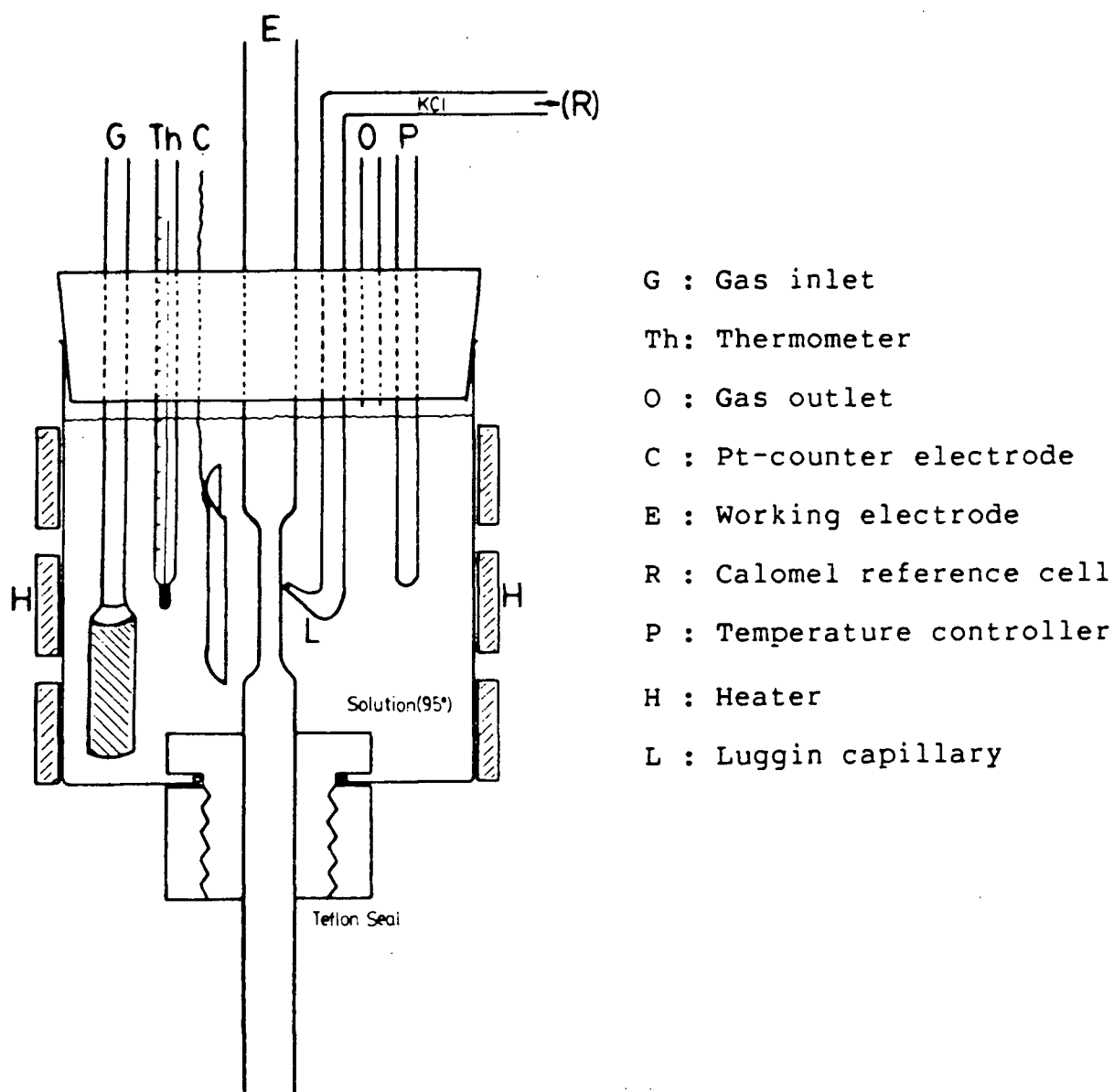
2.5. Fracture mechanics test

Results from polarization and slow strain rate studies
are often used as guidelines for the set up of long term
fracture mechanics tests. With a fracture mechanics test a
more realistic simulation of SCC can be done. Instead of a
smooth sample, such as in the SSRT studies, a prenotched and
fatigue pre-cracked specimen is used. This eliminates the
problems of crack initiation and allows loads to be employed
below the macroscopic yield strength. The characterization
of the stress state at the crack tip is done by defining the
so called stress intensity factor "K". This parameter
combines nominal stress with the crack length and a
correction factor accounts for the specimen geometry[56]. The
stress intensity factor is, therefore, a very useful
parameter for the comparison of various samples with
different crack length and loading conditions.

2.5.1. Specimen design

The most common specimen geometries used for SCC
studies in the corrosion laboratory at U.B.C. are the T-
notch double cantilever beam (TN-DCB)[57] and the double
cantilever beam (DCB)[58]. Both samples can be self stressed
(wedge or bolt loaded) or can be connected to a load
controlling device.

For this study, an easy-to-machine cantilever beam type of specimen was designed. By bolting two specimens together a test sample similar to the T-notch double cantilever beam can be made up and allows two cantilever bend specimen to be tested simultaneously.

Bars of size 101.6 x 25.4 x 25.4mm (1"x1"x4") were cut out according to the sampling map (page 16) . The notch was produced by drilling a hole (3/16" in diameter) through the sample and removing the remaining metal between the hole and top face of the specimen. This produced a 3/16" wide slot. A fine jewellers-saw cut was then made along the bottom of the slot about 1mm deep. Finally a razor blade scratch produced the initiation site for the fatigue pre-crack. (See Fig.38)

Figure 38 :
Specimen geometry for fracture-mechanics tests
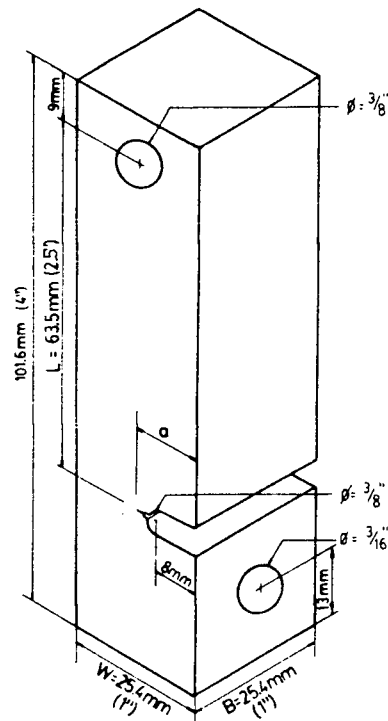
The specimen were fatigue pre-cracked by cyclic bending on a Sonntag SF-1-U fatigue machine. The applied load was selected so that the stress intensity at the crack tip was at least 5-10 $MNm^{-3/2}$ below the stress intensity applied during the SCC test.

The stress intensity for our sample geometry was calculated using a formula described by Brown[59]. (See Fig. 39d, pg. 57) The same relationship was used by Robinson and Scully[60] to do SCC experiments with a notched cantilever beam. However, this formula assumes pure bending of a cantilever beam which is not fully satisfied in our set up. The maximum bending moment that can be applied is controlled by the maximum tensile fiber bending stress. The analysis is valid only below the yield point of the material.

The relationship between tensile fiber bending stress and bending moment is given by $\sigma = Mx/I$ ...(1)

M = bending moment;

x = distance from neutral fiber;

I = moment of Inertia

Applied to our cantilever beam : $\sigma = (6M)/B(W-a)^2$ ...(2)

Calculations for our case have shown that at stress intensities above about 50$MNm^{-3/2}$ for steel "A" and "R" this restriction of the maximum applied bending moment is violated. Therefore, linear elastic fracture mechanics should not be applied any longer to calculate the exact

absolute stress intensity at the crack tip. However, a comparison between different steels of the same geometry can still be done.

In Figures 39a - 39d different methods for the determination of the stress intensity applied to our type of specimen geometry are illustrated.

Figure 39 :

Different specimen geometries for fracture mechanics tests
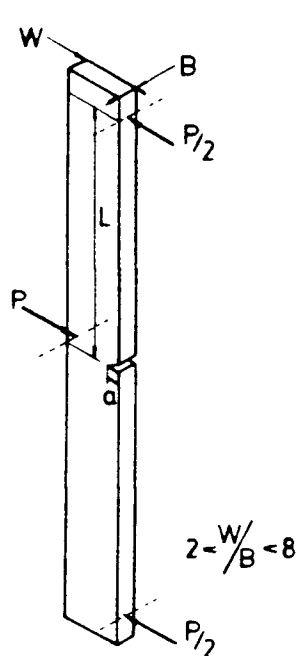
a) 3-Pt Bending
(Brown 58)
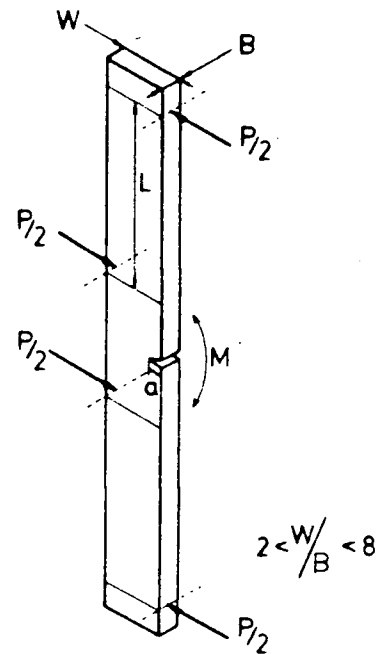
b) Pure Bending
(Brown 58)

$$K = \frac{6M}{BW^2}\sqrt{a} \cdot Y \quad \ldots (3)$$

$$Y = \left[0.624 - 0.876\left(\frac{a}{W}\right) + 4.349\left(\frac{a}{W}\right)^2 - 7.645\left(\frac{a}{W}\right)^3 + 8.040\left(\frac{a}{W}\right)^4\right]$$

$$M = \frac{PL}{2}$$

$$K = \frac{6M}{BW^2}\sqrt{a} \cdot Y \quad \ldots (4)$$

$$Y = \left[0.633 - 0.790\left(\frac{a}{W}\right) + 4.135\left(\frac{a}{W}\right)^2 - 7.379\left(\frac{a}{W}\right)^3 + 7.899\left(\frac{a}{W}\right)^4\right]$$

$$M = \frac{PL}{2}$$

Figure 39 : cont'd
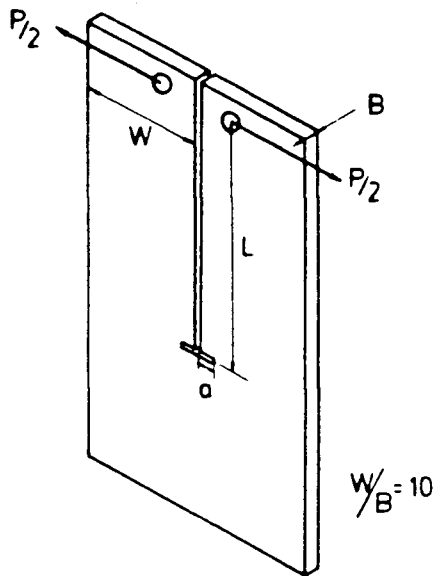
c)   T-DCB
(Russel, Tromans [57])
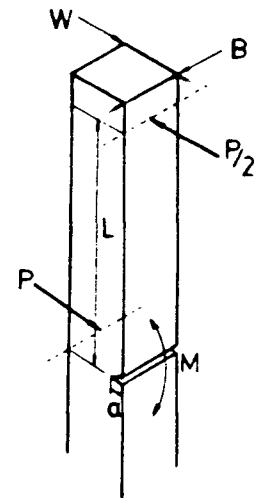
d)   Cantilever Beam
(Brown [59])

$$K = \frac{6M}{BW^2}\sqrt{a} \cdot Y \qquad \ldots (5)$$

$$Y = \left[2.43 - 3.62\left(\frac{a}{W}\right) + 14.5\left(\frac{a}{W}\right)^2 - 24.6\left(\frac{a}{W}\right)^3 + 26.5\left(\frac{a}{W}\right)^4 \right]$$

$$M = \frac{PL}{2}$$

$$K = \frac{4.12 \, M \cdot \sqrt{\frac{1}{Y^3} - Y^3}}{BW^{3/2}} \qquad \ldots (6)$$

$$Y = \left[1 - \left(\frac{a}{W}\right) \right]$$

$$M = \frac{PL}{2}$$

In Figure 40 (pg. 58) all four methods are applied to our specimens geometry and stress intensities are calculated for different crack length.

One reason why the curves differ from each other is the restricted use of each calculation method to specific sample dimensions. This is due to the experimental calibration of the "geometric factor" of each specimen type.

Since the aim of this project was to compare different steel qualities under the same testing conditions no attempt was made to calibrate our sample geometry with the compliance method. (it also would have been difficult to account for the yielding of the bolt during a compliance calibration).

Figure 40 : Stress intensity vs. crack length for different specimen geometries
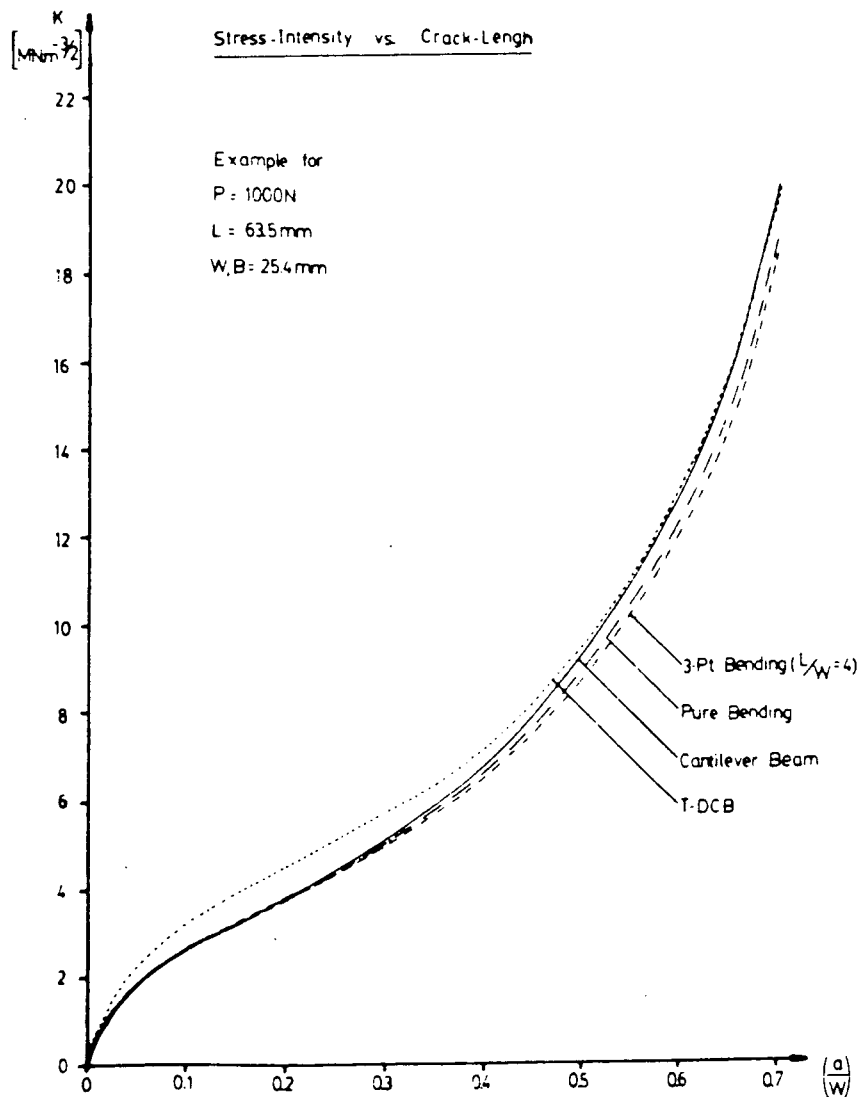
2.5.2. Test set up

Before the test, the samples were cleaned with acetone and alcohol. Subsequently, the specimens were wrapped with PTFE tape so that only the notch area was exposed to the environment. After tightly bolting the two pieces together (with SAE Grade 5 bolts), the bolt ends were also carefully wrapped with PTFE tape. Copper wires were screwed into each sample and connected to the same potentiostat used for the SSRT studies (see page 51).

The test cell (see Fig.41, pg. 60) was a 600 ml Teflon beaker fitted with a Teflon lid. From the side, openings were cut into the lid for the grips. Through the top, the following devices were inserted: Luggin capillary, temperature probe, platinum counter electrode, gas inlet and condenser outlet.

A heating mantle was mounted at the bottom of the beaker and the temperature was adjusted with a temperature controller as described previously (sections 2.3.1 and 2.4.1). The Luggin capillary was positioned about 1mm from the crack tip. To minimize contamination of the test solution with KCl from the reference cell, a "bridge" of test solution was set up between the test cell and a beaker filled with cold (room temperature) test solution. A salt bridge with saturated KCl was then connected from the beaker to the calomel reference cell, (i.e. a double bridge assembly), as shown in Figure 41.

Figure 41 : Test set up for stress corrosion experiments with fracture mechanics specimen
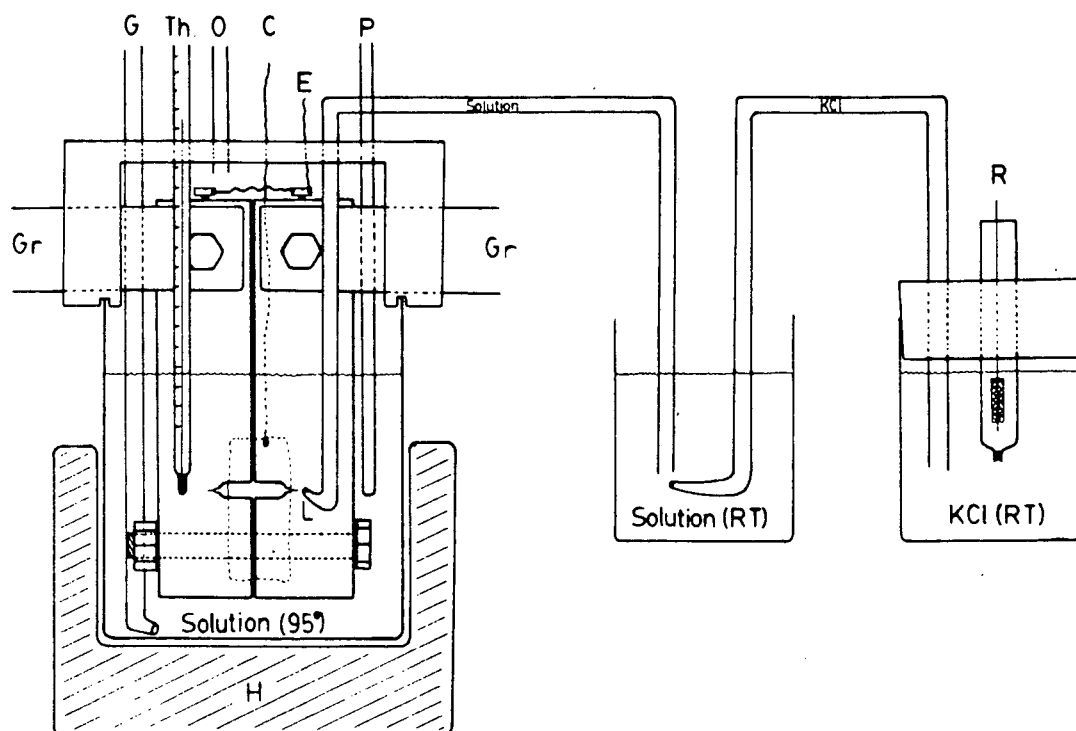
G : Gas inlet

Th: Thermometer

O : Gas outlet

C : Pt-counter electrode

E : Working electrode (SCC-samples)

R : Calomel reference cell

P : Temperature controller

Gr: Grips

H : Heater

L : Luggin capillary

The gas inlet was used for CO_2 in tests with carbonate solutions and for N_2 in all other tests. However, N_2 purging was always stopped after the test was run for a few hours (otherwise gas bubbles tended to form at the tip of the Luggin capillary), and the gas outlet was sealed.

Testing Procedure:

The sample was immersed into the hot test solution ($95^{\circ}C$ for all experiments). Then the desired load was applied with a horizontally mounted Hounsfield tensometer and, at the same time the potential was set to a fixed value with the potentiostat. The lid and all connections were subsequently sealed with silicon rubber to avoid evaporation of the test solution. During the whole test the load was kept constant. This required very little adjustment of the loading mechanism becouse of the slow cracking rates. The normal duration of one test was 500 hours (3 weeks).

After the test, the samples were broken open in liquid nitrogen. Only two experiments required interruption of the test because of a bolt failure. Consequently the specimen configuration proved to be adequate for SCC testing. The major problem was the development of gas bubbles in the Luggin capillary which could cause a loss of potential control. Insertion of a cotton thread into the capillary helped in some circumstances, except when the test solution dissolved it during the test, eg. in the sodium hydroxide solutions.

For investigations of the fracture surface with the SEM, the samples were cleaned with inhibited acid as described on page 51.

The crack propagation increment was measured with a travelling microscope at five different locations on the fracture surface. (see Fig.42)

Figure 42 : Illustration of crack propagation measurements

Crack propagation
measurements

Notch

Fatigue precrack

Stress corrosion crack (Δa)

Overload failure (liq. N_2)
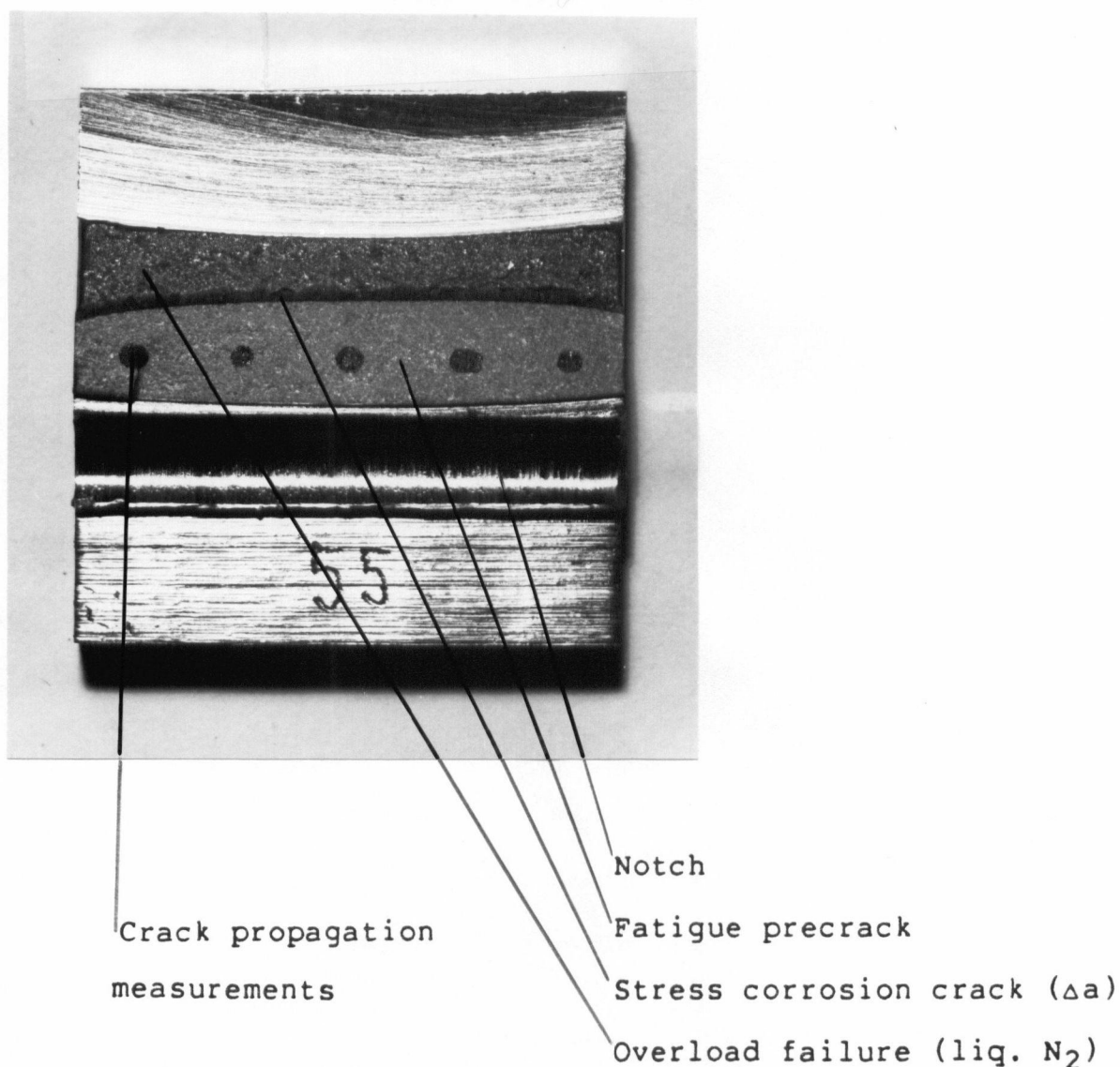
III. <u>RESULTS</u>

3.1. <u>Anodic Polarization curves</u>

In the following Figures anodic polarization curves of all three rotor steels are shown. All curves are drawn with two different scales for the potential: the standard hydrogen electrode (V_{SHE}) and the standard calomel electrode (V_{SCE}). The standard hydrogen electrode scale was obtained by adding 242mV to the standard calomel electrode scale. All experimental measurements were made with the calomel reference electrode. Additionally, results from the remelted and "doped" steel R are shown.

3.1.1. <u>Carbonate solutions</u>

Tests in the dilute carbonate solutions were mainly done with the "O" steel. However, some tests were repeated with "A" and "R" steels but no major difference was found. In the acidic CO_2/H_2O solutions no passivation phenomena was observed and general corrosion occured. The corrosion current density increased towards more noble potentials. See Figure 43, pg. 64.

A small addition of bicarbonate to the CO_2/H_2O solution raised the pH and the polarization behavior changed dramatically. See Fig. 44, pg. 64. A wide active peak at

around -500mV$_{SCE}$ appeared, followed by a passive region above -200mV$_{SCE}$ The corrosion current density in this passive region was about two orders of magnitude smaller than in the CO_2/H_2O system where no passivation was observed. In the very dilute bicarbonate solutions there was a great tendency for crevice corrosion and with samples mounted in epoxy the passive behavior was overwhelmed by crevicing effects.
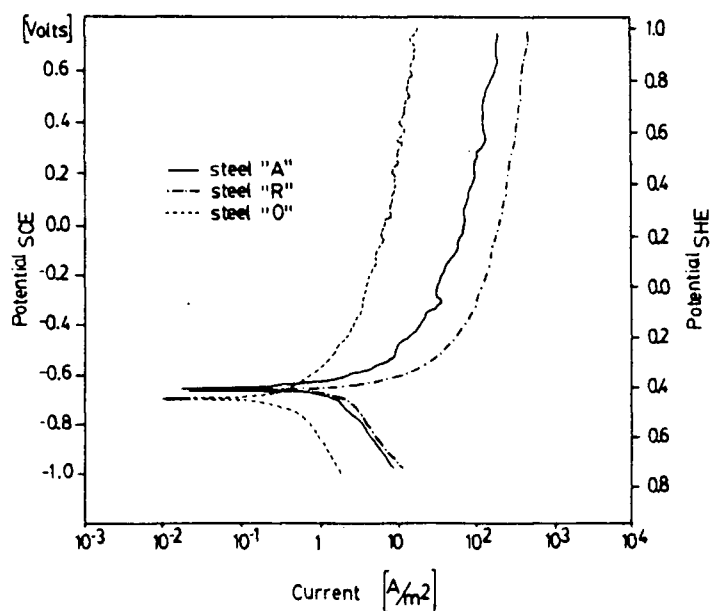
Figure 44:

Polarization curve for steel "O" in NaHCO$_3$ (3.5·10^{-3}M)
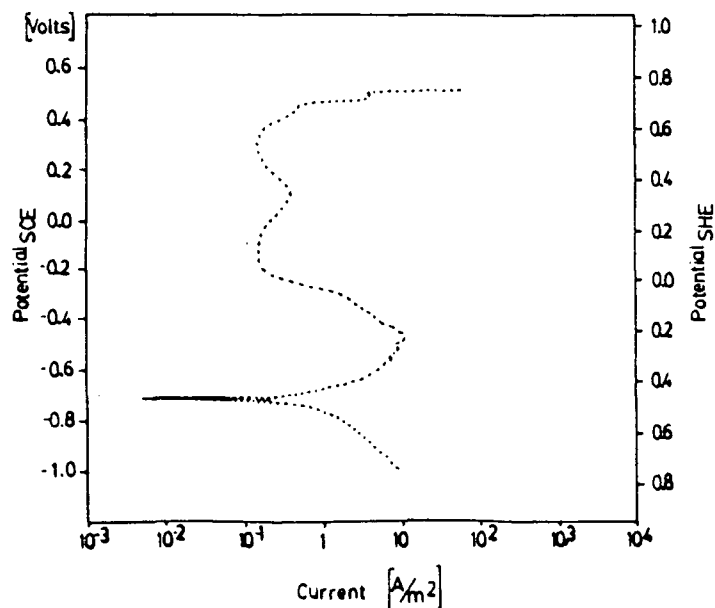
Figure 45:

Polarization curves for steel "O" in NaHCO$_3$ (3.5·10^{-2}M), fast and slow scan

With increasing bicarbonate concentration, the tendency for crevice corrosion decreased and polarization tests could be done with the rod shaped samples as well as with the flat mounted specimen.

Additions of bicarbonate below one mole per liter did not have a great influence on the passive region of the curves. However, it may be stated that the corrosion current in the passive region increased with the increased bicarbonate concentration. (compare Fig.44-46, pg. 64,66)

The active peak in the $3.5 \cdot 10^{-3}$ molar solution was a single wide peak. At higher concentrations this peak subdivided into two peaks. In the $3.5 \cdot 10^{-2}$ molar solution this was only observed at the slow scan rate, whereas in the $3.5 \cdot 10^{-1}$ molar solution both peaks were found at fast and slow scan rates.

Upon raising the pH further in the 1M carbonate/bicarbonate solution, only one active peak was observed. But now the behavior in the passive region changed. At about $300mV_{SCE}$ a current peak ("transpassive" peak) was observed with current densities nearly ten times higher than in the passive plateau. (See Fig.47, pg. 66) Also in the more dilute solutions, sometimes small peaks were found in the passive region but not as pronounced as in the 1 molar carbonate/bicarbonate solution.
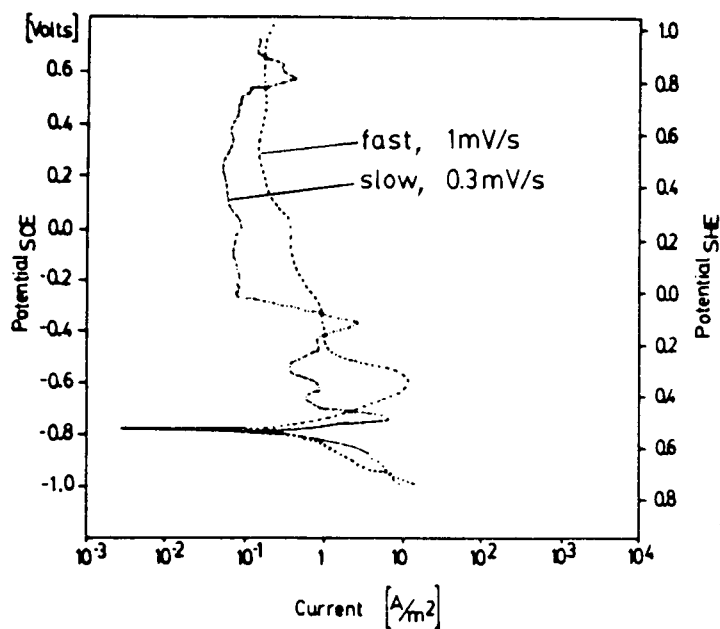
Figure 45:

Polarization curves for steel "O" in $NaHCO_3$ $(3.5 \cdot 10^{-2}M)$, fast and slow scan
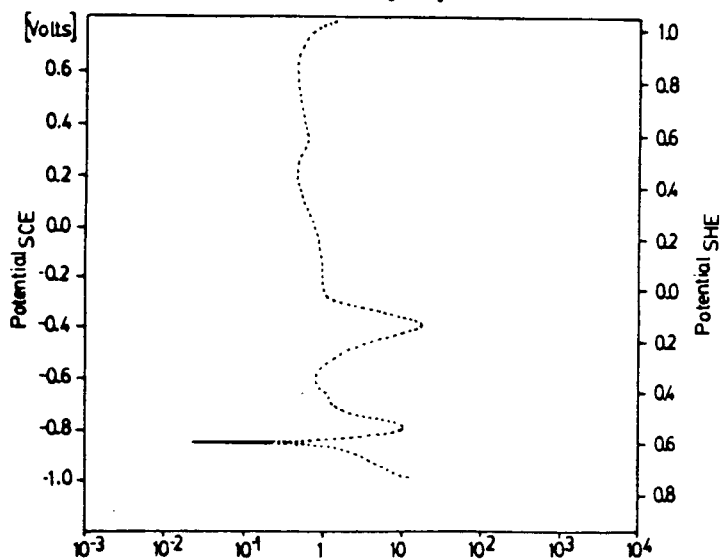
Figure 46:

Polarization curve for steel "O" in $NaHCO_3$ $(3.5 \cdot 10^{-1}M)$
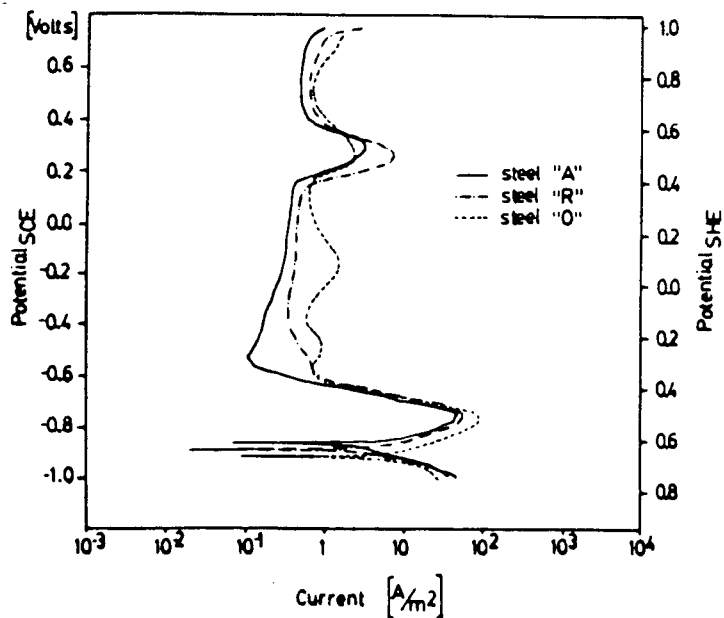
Figure 47:

Polarization curves for steels "A", "R" and "O" in 1M $NaHCO_3$ + 1M Na_2CO_3

3.1.2. Sodium Hydroxide solutions

In the strong alkaline sodium hydroxide solution (3.5 molar, pH 13), active/passive behavior of all three steels was observed. (See Fig. 48, pg. 68) The active peak consisted actually of two peaks but their separation was not well defined in all tests. The current density at the peak was more than one order of magnitude smaller than in the carbonate solutions. In the passive region at about -150mV$_{SCE}$, again another peak was detected with a corrosion current density comparable to the one in the carbonate solution. This transpasssive peak was more pronounced in the steel "A" and "R", whereas in "O" a higher current density in the passive "plateau" diminished the peak appearance.

In this solution the position of the oxidation curve with respect to the reduction curve caused more than one intersection point, producing a zero applied current (compare Fig.35, page 46). Therefore, another "cathodic peak" is seen in some polarization curves at about -800mV$_{SCE}$. However, this peak was not of interest for the present corrosion study.

With a NaOH concentration of 0.35 mole/l, the polarization curves were about identical to the 3.5 molar solutions. However, only a single active peak appeared.
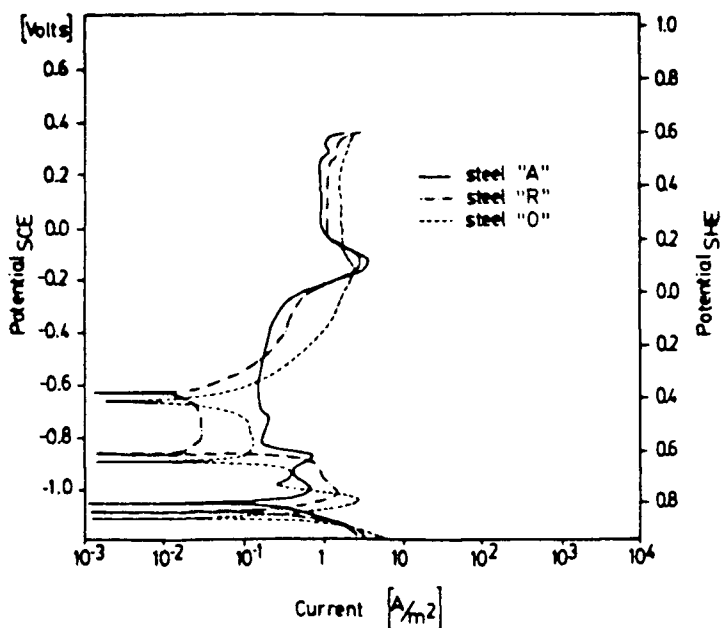
Figure 48:

Polarization curves for steels "A", "R" and "O" in 3.5M NaOH

In Figure 49 a polarization test of the same sample was run twice. It can be seen that the same result is obtained except for the peak in the passive region where a decrease in corrosion current could be seen.
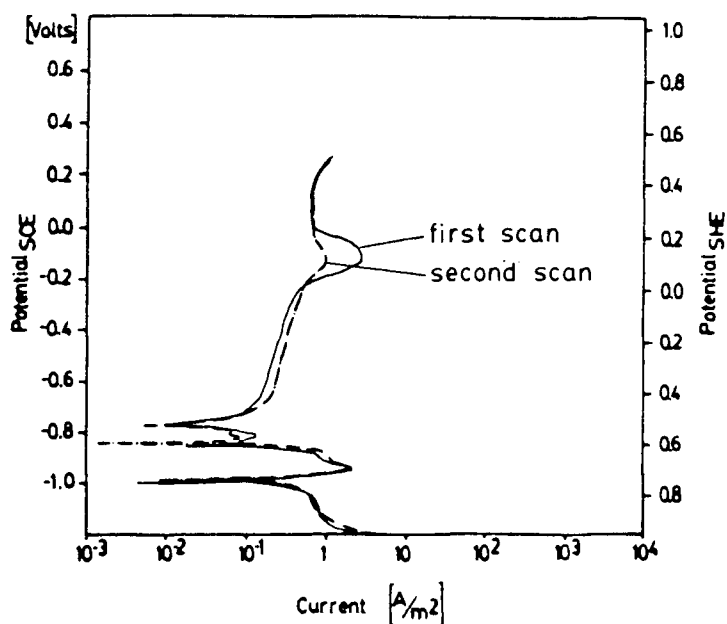
Figure 49:

Polarization curves for steel "R" in 3.5M NaOH, first and second scan

3.1.3. Steel "R" doped with sulphides

Steel "R" was vacuum remelted and then doped with either CaS or MnS. Polarization tests were done in the as-cast, hot rolled and heat treated condition. Tests were only performed in the 3.5 molar NaOH solution at 95°C.

The results are shown in (Fig.50 and 51). For comparison "R"-steel "as received" (not remelted) is also included. From the microstructure investigation it is known that CaS inclusions were also present in "R" but to a lesser degree than in the CaS doped steel.
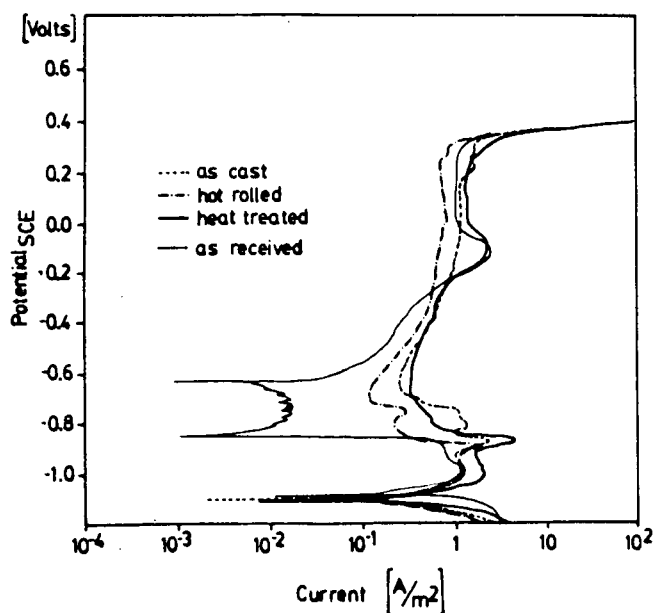
Figure 50:

Polarization curves for steel "R" and steel "R" doped with CaS in 3.5M NaOH
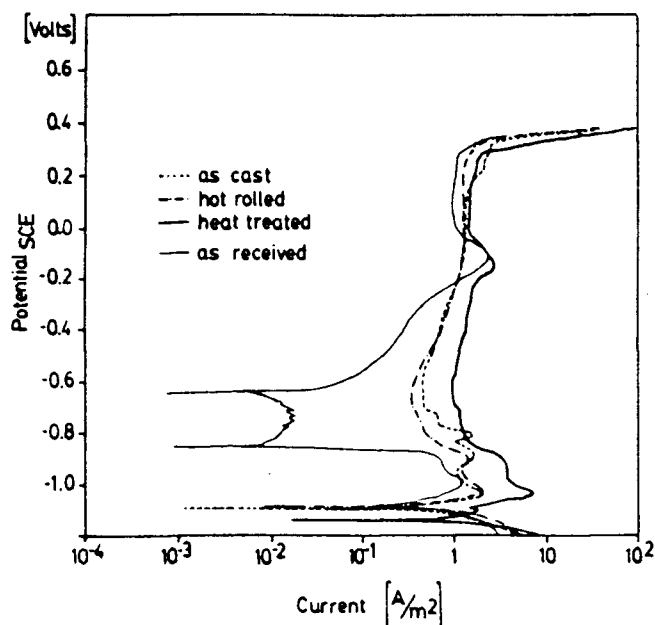
Figure 51:

Polarization curves for
steel "R" and steel "R"
doped with MnS in
3.5M NaOH

No major difference between the doped steel and the
regular R-steel could be seen. The shape of the anodic peak
seemed to consist of different peaks in both doped steels.
The maximum corrosion current density at the peak was about
a factor of five higher than in the regular R-steel. Also
the current density in the passive region seemed to be
higher in the doped steels and, therefore, no cathodic peak
appears in this region. The earlier observed peak in the
passive region was only observed in the heat treated
condition and appears to be uninfluenced by the inclusions.
Practically no difference could be seen between the two
doped steels in the entire potential range investigated. To
fully characterize the influence of inclusions, many more
experiments are necessary. Different solutions with lower
pH values have to be tested.

3.2. Slow strain rate tensile tests

In Table II (pg.72) results of all SSRT studies are summarized. It can be seen that nearly all tests with the carbonate solutions gave much deeper cracks than in the sodium hydroxide solution. This was observed with all three steels. The same behavior is reflected in the reduction in area, where lower values were obtained in the carbonate solutions (a small reduction in area is equivalent to little necking).

Steel "A" and "R" seemed relatively insensitive to cracking in the sodium hydroxide solutions.

Figure 52 page 73 illustrates the effect of potential on the reduction in area. The effect of small potential changes on the cracking behavior of SSRT samples can be seen in Figures 53 and 54 (pg. 74,75). However, to find a clear dependence between the reduction in area and the applied potential many more tests would be necessary.

Table II :   Results of slow strain rate tensile tests

Steel	Environment	Potential mV_{SCE} mV_{SCE}	Red in area %	Max. crack length μm	Crack velocity m/s
"O"	CO_2+H_2O	0	32.7	68	$9.4 \cdot 10^{-10}$
	"	-500	29.1	113	$1.6 \cdot 10^{-9}$
	"	-600	34.4	45	$6.2 \cdot 10^{-10}$
	"	-685	23.7	29	$4.0 \cdot 10^{-10}$
	"	-1000	22.0	--	--
"A"	CO_2+H_2O	-600	71.8	68	$9.4 \cdot 10^{-10}$
	"	free	73.5	<5	$<6.9 \cdot 10^{-11}$
"O"	$3.5 \cdot 10^{-3}M$ NaHCO$_3$	-100	15.3	250	$3.5 \cdot 10^{-9}$
	"	-200	26.1	159	$2.2 \cdot 10^{-9}$
	"	-370	32.6	--	--
	"	-500	40.8	159	$2.2 \cdot 10^{-9}$
	"	-1000	26.6	--	--
"A"	$3.5 \cdot 10^{-3}$NaHCO$_3$	-500	66.7	114	$1.6 \cdot 10^{-9}$
"O"	1MNa$_2$CO$_3$+1MNaHCO$_3$	-600	40.8	--	--
	" "	-680	39.6	45	$6.2 \cdot 10^{-10}$
	" "	-750	38.0	159	$2.2 \cdot 10^{-9}$
	" "	-750	38.1	136	$1.9 \cdot 10^{-9}$
"A"	1MNa$_2$CO$_3$+1MNaHCO$_3$	-750	67.4	114	$1.6 \cdot 10^{-9}$
"R"	1MNa$_2$CO$_3$+1MNaHCO$_3$	-750	68.7	182	$2.5 \cdot 10^{-9}$
"O"	3.5M NaOH	-150	48.8	34	$4.7 \cdot 10^{-10}$
	"	-400	44.9	23	$3.2 \cdot 10^{-10}$
	"	-1000	39.0	10	$1.4 \cdot 10^{-10}$
	"	-1000	41.6	23	$3.2 \cdot 10^{-10}$
"A"	3.5M NaOH	-880	72.4	<5	$6.9 \cdot 10^{-11}$
	"	-980	73.5	18	$2.5 \cdot 10^{-10}$
"R"	3.5M NaOH	-600	68.4	--	--
	"	-880	72.3	--	--
	"	-950	72.7	<7	$9.7 \cdot 10^{-11}$
"O"	0.35M NaOH	-850	43.9	--	--
"O"	Oil (95°C)		48.7	--	--
"A"	Oil (95°C)		75.8	--	--
"R"	Oil (95°C)		72.5	--	--
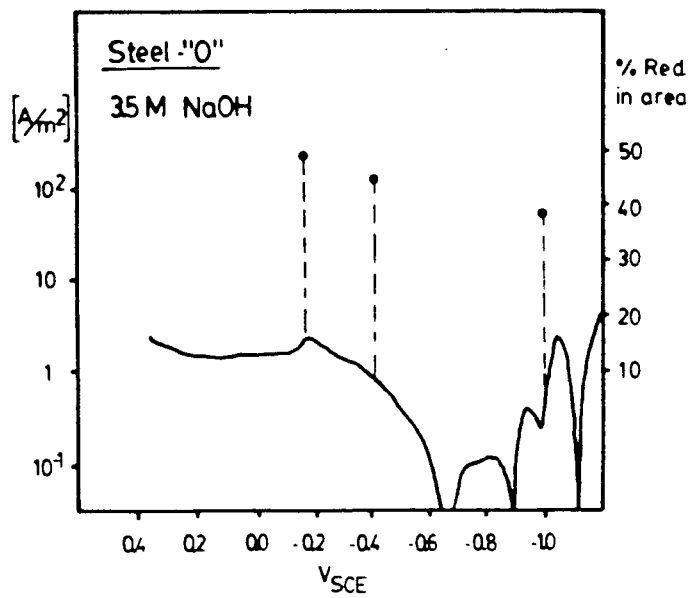
Figure 52:

Influence of potential on the reduction in area during SSRT-tests
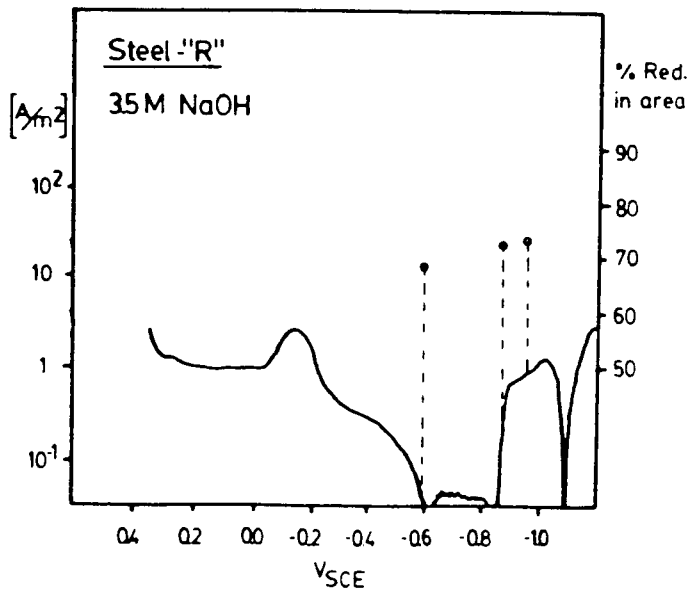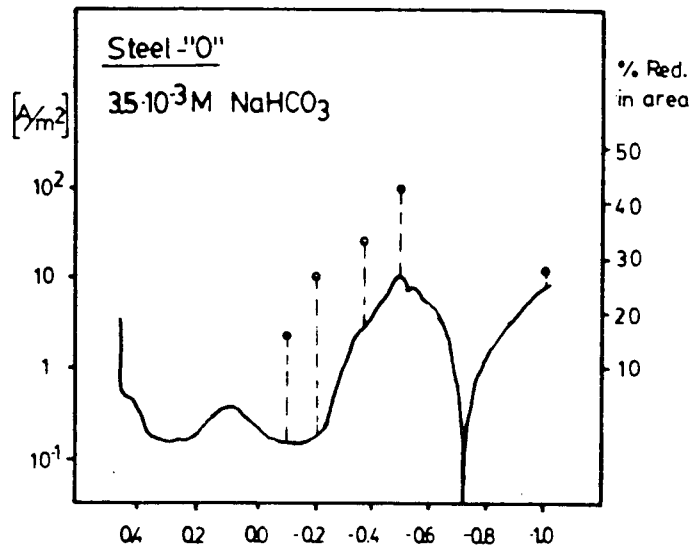
Figure 53 : Reduction in area and surface cracks of steel-"O" at different potentials in the CO_2/H_2O system, SSRT-test
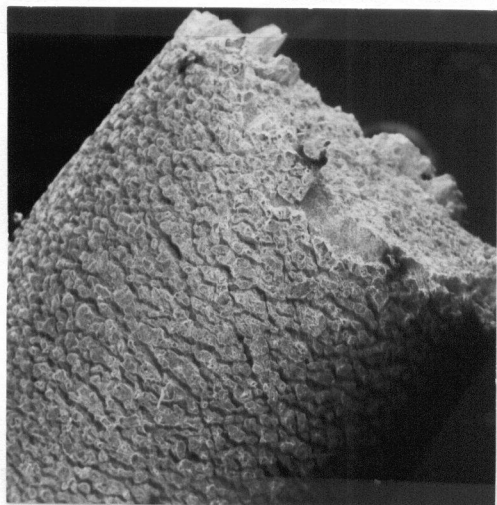
-500 mV$_{SCE}$
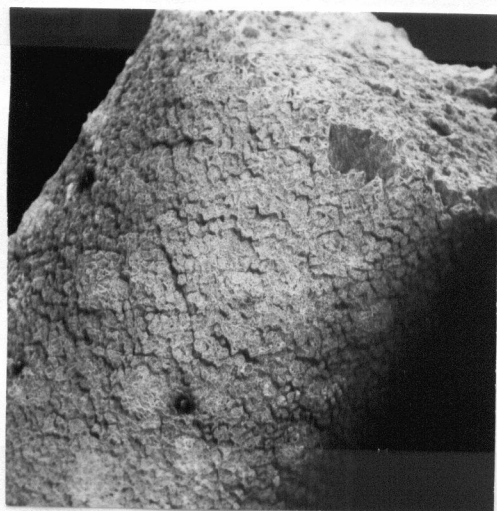
-600 mV$_{SCE}$

-685 mV$_{SCE}$
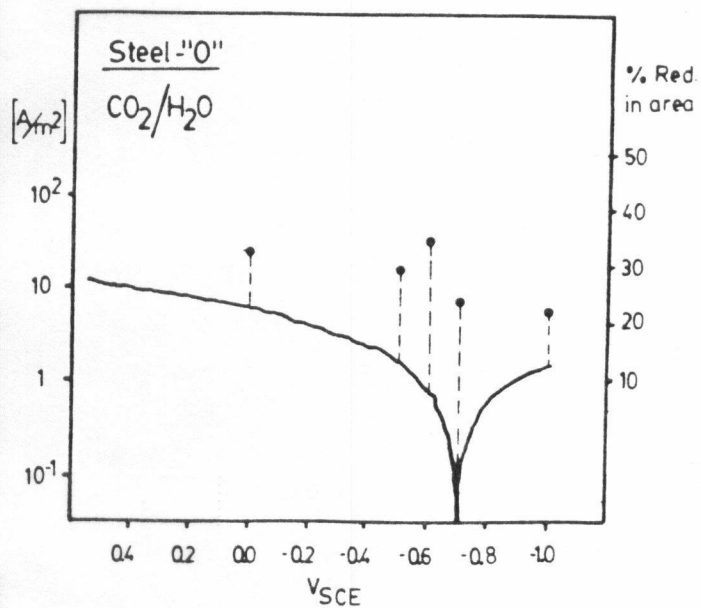
Figure 54 : Reduction in area and surface cracks of steel-"O" at different potentials in the 1M $NaHCO_3$ + Na_2CO_3 system, SSRT-test
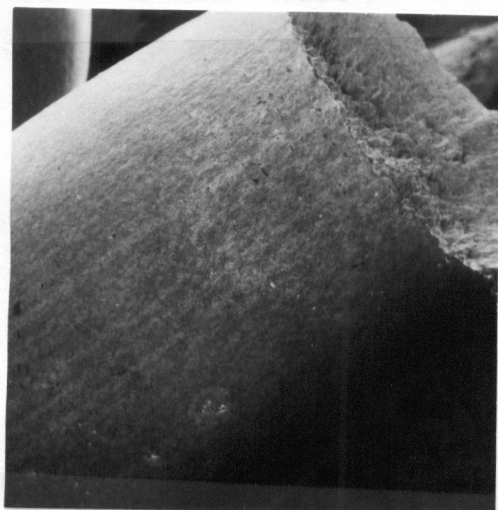
−600 mV$_{SCE}$
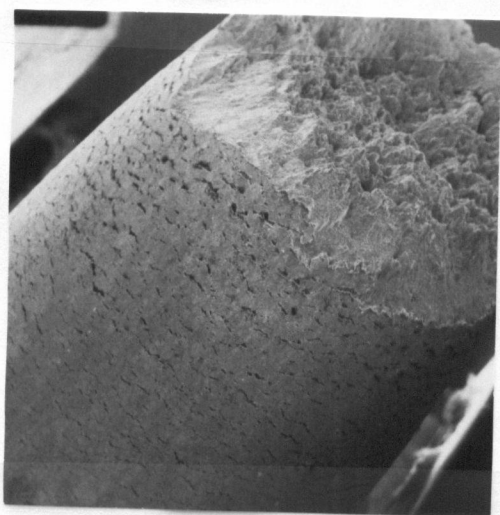
−680 mV$_{SCE}$
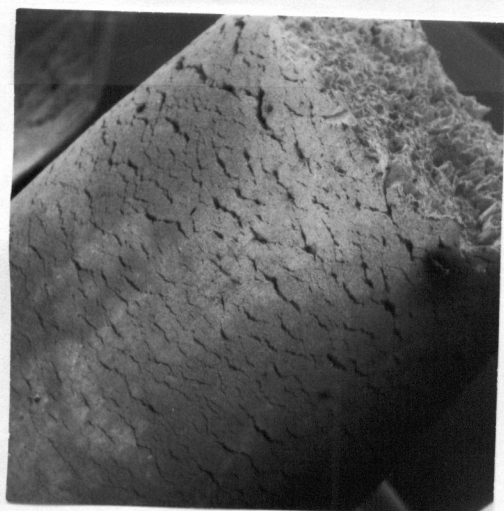
−750 mV$_{SCE}$
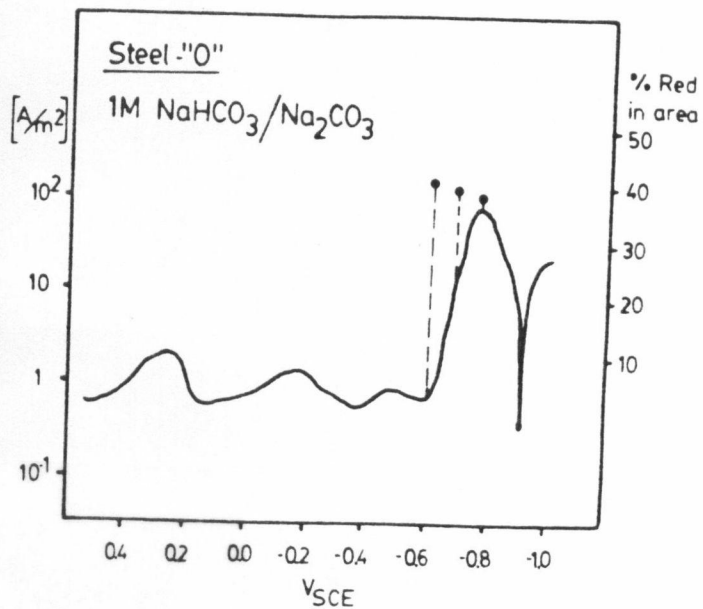
The environment and electrochemical potential selected for the fracture mechanics tests were based on micrographs of sectioned SSRT samples. From these, conclusions could be drawn as to whether the corrosive attack during the SSRT experiment was of a general corrosion and pitting nature, or if sharp, penetrating cracks were formed. The latter were assumed to be a sign for sensitivity to SCC. Different types of SSRT-cracks are illustrated in Figure 55 (pg. 77).

From the longest secondary crack length, an average crack velocity could be estimated by dividing the crack length by the time of plastic deformation during the test. In the 1 molar carbonate/bicarbonate solution, a crack growth rate of about $2 \cdot 10^{-9}$m/s was obtained for all three steels. However, in the 3.5 molar NaOH solution, steel-"O" was cracking at about $3.5 \cdot 10^{-10}$m/s, steel-"A" gave a maximum value of about $2 \cdot 10^{-10}$m/s and steel-"R" seemed to show a cracking-rate below 10^{-10}m/s.

In the Figures 56-58 on page 78, cracking on the surface of the three steels in 3.5M NaOH is compared. It was difficult to draw conclusions about the cracking path. Steel-"A" appeared to show some indications of intergranular cracking.

Figure 55 : Surface cracks in SSRT samples after tests in 3.5M NaOH (steel-"R"), CO_2/H_2O (steel-"O") and 1M $NaHCO_3$ + 1M Na_2CO_3 (steel-"A")
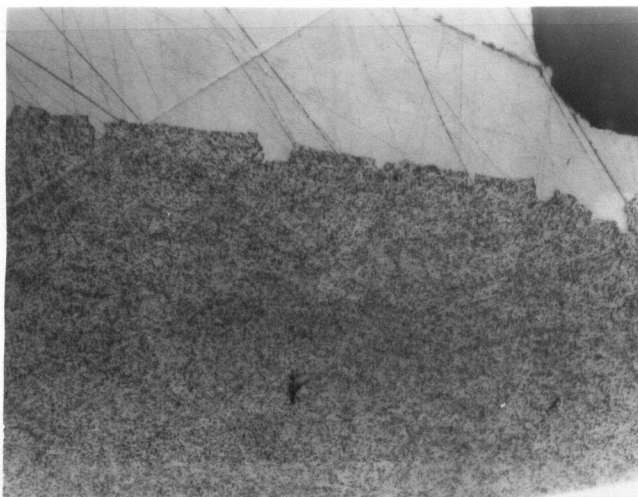
Steel "R", 3.5M NaOH, -950 mV$_{SCE}$

Shallow surface cracks

Mag.: 400x, etched
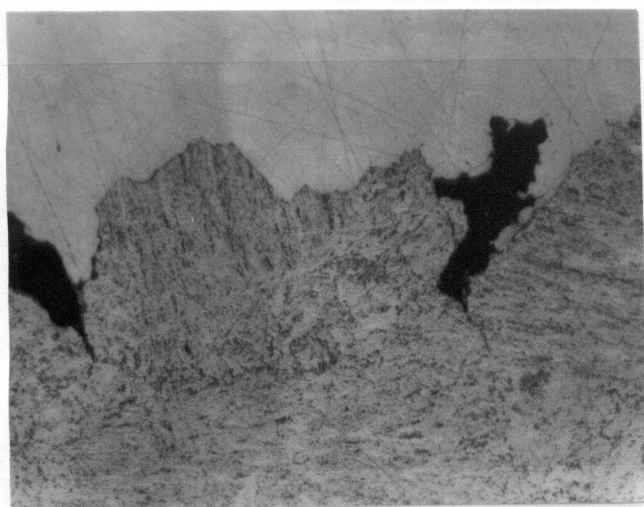
Steel "O", CO_2 / H_2O, -600 mV$_{SCE}$

Strong surface attack

Mag.: 400x, etched
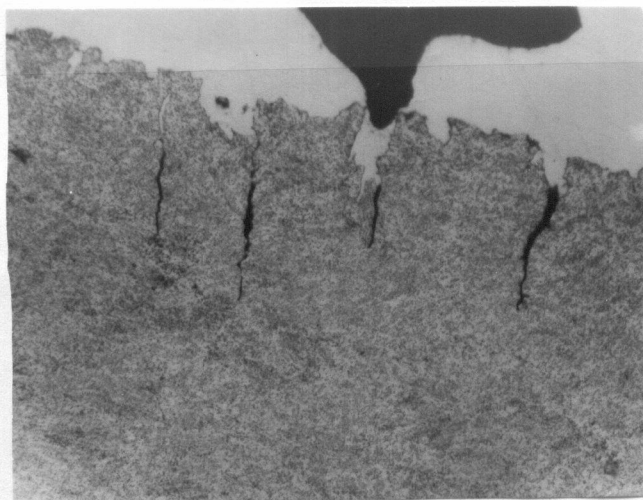
Steel "A", 1M $NaHCO_3$ + 1M Na_2CO_3, -750 mV$_{SCE}$

Deep, penetrating cracks

Mag.: 400x, etched
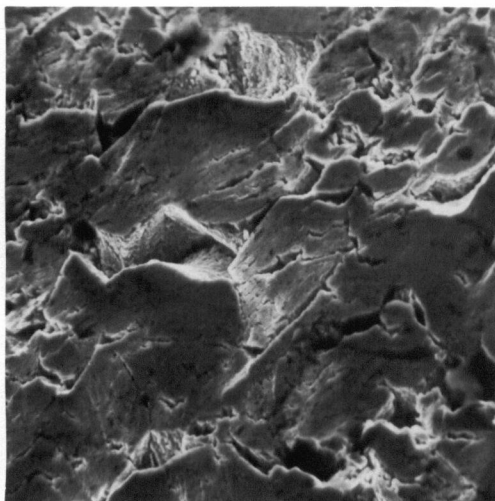
Figure 56:

SEM-picture, surface cracks of steel "A" after testing in 3.5M NaOH at -980 mV$_{SCE}$, SSRT-test

The surface of the samples was cleaned with inhibited acid

Mag.: 1,000x
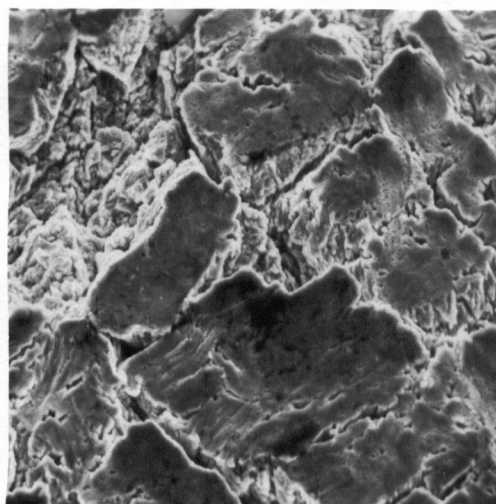
Figure 57:

SEM-picture, surface cracks of steel "R" after testing in 3.5M NaOH at -950 mV$_{SCE}$, SSRT-test

Mag.: 1,000x
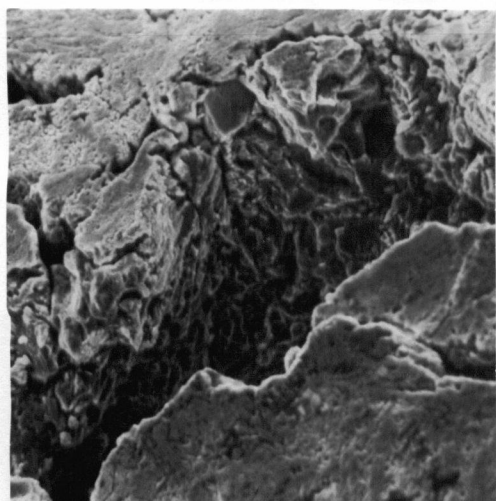
Figure 58:

SEM-picture, surface cracks of steel "O" after testing in 3.5M NaOH at -1000 mV$_{SCE}$, SSRT-test

Mag.: 1000x

In Figures 59 and 60, the fracture surface of steel "A"
and "O" inside the cracks is compared. No major difference
can be seen, which may explain the similar crack velocities
observed for both steels in the carbonate/bicarbonate
solution.
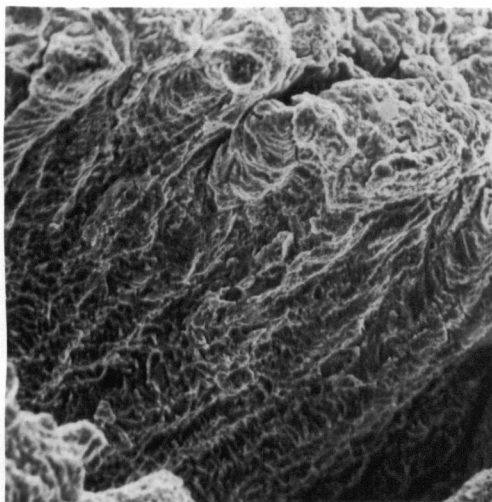
Figure 59:

SEM-picture, fracture surface
inside a crack, steel "A" tested
in 1M $NaHCO_3$ + 1M Na_2CO_3 at
-750 mV_{SCE}, SSRT-test

At the top: surface of the
SSRT-specimen
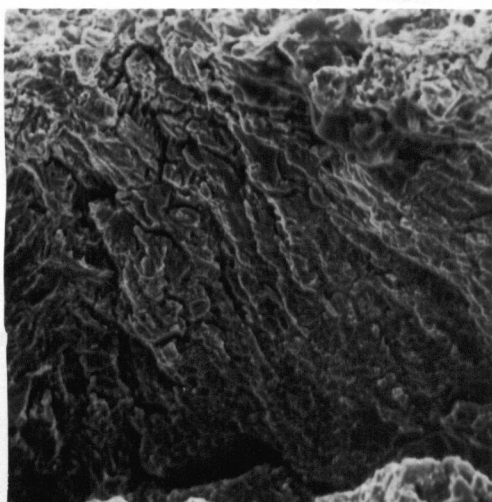
Mag.: 800x

Figure 60:

SEM-picture, fracture surface
inside a crack, steel "O" tested
in 1M $NaHCO_3$ + 1M Na_2CO_3 at
-750 mV_{SCE}, SSRT-test

At the top: surface of the
SSRT-specimen

Mag.: 800x

3.3. Fracture mechanics tests

In Table III, page 84 the results of all fracture mechanics SCC tests are summarized. The numbering of each specimen has no meaning in respects to the testing conditions, it was done during specimen fabrication. Most tests were run for 500 hours or more. However, some tests needed to be terminated earlier because of instrumentation problems. (i.e. unstable potential control)

The stress intensity is reported at the onset of cracking $K_I(a)$ and after a crack growth increment of Δa at the end of a test $K_I(a+\Delta a)$. The increase in crack length, Δa, is an average value obtained from five measurements (compare Fig.42, page62).

The crack growth rate does not include an unknown incubation time and, therefore, the actual crack propagation rate may be higher (especially for short testing times).

For steel "A" and "R" samples were only tested in the "CC" and "CL" directions, becouse the thickness dimension of the discs was not sufficient for "LC" samples. For SCC tests, these specimens were not labeled as "CC" or "CL" since both mechanical tests and metallographic investigations did not reveal any difference between these two directions.

Steel-"O" was tested in "CC" , "CL" and "LC" directions. Because of the directional property dependence

in this material, all samples were labelled according to their directions. (See Table III, pg. 84)

3.3.1. Carbonate solutions

The 1.5%CrMoV steel-"O" showed no cracking in the acidic CO_2 / H_2O solution and none in the near neutral CO_2 + $NaHCO_3$ ($3.5 \cdot 10^{-3}$ molar) solution. In the alkaline 1 molar carbonate/bicarbonate solution, only three samples showed cracking. However, the specimen No."O"/2* may not be compared with the other samples since the solution in this case was strongly contaminated with chloride ions and the potential during the test was not stable due to problems in the electrical circuit. The reason why the other two samples cracked is not clear since all the other tests with lower and higher stress intensities showed no cracking.

The 3.5%NiCrMoV-steel-"A" cracked in the 1 molar carbonate/bicarbonate solutions at a stress intensity of about $50MNm^{-3/2}$. No cracking could be observed below $30MNm^{-3/2}$.
Steel-"R" was not tested in carbonate solutions.

In the CO_2/H_2O solution, both steels "A" and "R" showed strong corrosion at the crack tip. However, this may not be called stress corrosion cracking. It can be assumed that this form of attack blunts the crack tip and therefore,

reduces the tendency for further crack propagation. An illustration of the "rounded" crack tip is given in Fig. 61.
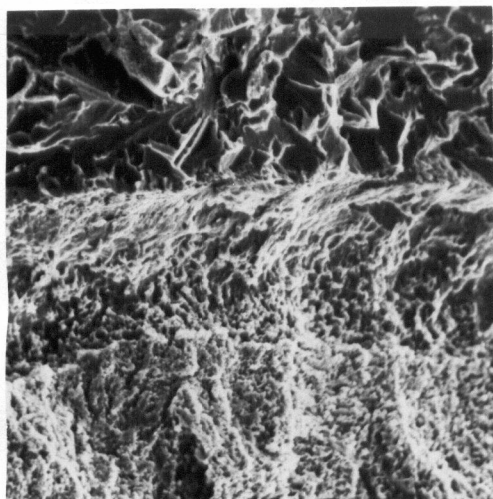
Figure 61:

SEM-picture, crack tip of steel "A" after testing in CO_2 / H_2O at the free corr. pot., SCC-test

At the top: overload fracture in liq. Nitrogen
At the bottom: fatigue precrack
At the centre: rounded SCC crack

Mag.: 900x

3.3.2. Sodium hydroxide solutions

Figure 62, pg.85 shows a v-K plot of all three steels in 3.5 molar NaOH. The potential was set corresponding to the active peak at -870 to -1000mV$_{SCE}$. (Compare polarization curves Fig. 48, pg. 68)

For the 1%CrMoV steel-"O", the stress intensity was varied between about 25 and 45 MNm$^{-3/2}$. The crack growth rate seemed to decrease slightly with decreasing stress intensity. However, even at a stress intensity below 30 MNm$^{-3/2}$ a crack growth rate around $4 \cdot 10^{-10}$ m/s was measured. The K$_{ISCC}$ value (stress intensity below which no measurable cracking is found) must lie below about

$25 MNm^{-3/2}$. However, experiments at such low K-values were not performed. The influence of crack plane direction seemed to be rather minimal. The LC direction may have given a slightly slower crack rate than the "CL"-direction at the same stress intensity, but there was no clear difference in cracking velocity between "CC" and "CL" directions.

The 3.5%NiCrMoV steel "A" was tested between approximately 40 and 55 $MNm^{-3/2}$. It was noticed that the crack growth rate decreased rapidly around 40 $MNm^{-3/2}$. Therefore, a K_{ISCC} value above about 35 $MNm^{-3/2}$ could be estimated. The crack growth rate above 40 $MNm^{-3/2}$ was around $10^{-10}m/s$ and seemed relatively independent of the stress intensity. (typical stage II behavior in a v-K plot).

Not many tests were run with the 3.5%NiCrMoV steel "R". No cracking was observed below 40 $MNm^{-3/2}$. At about $50 MNm^{-3/2}$, however, a crack growth rate similar to the "O"-steel was measured which was higher than for steel-"A".

Table III :   Results of fracture mechanics (SCC) tests

Steel/No	Fracture plane	Test-solution	Potential mV$_{SCE}$	Test-duration hrs	$K_I(a)$ MNm$^{-3/2}$	$K_I(a+\Delta a)$ MNm$^{-3/2}$	(Δa) µm	Crack growth rate m/s
"O"/2*	CC	1M Carb/Bicarb	-750	1000	40.6	46.0	900	2.5x10^{-10}
/10	CC	"	"	500	38.4	-	-	-
/11	CC	"	"	500	25.3	-	-	-
/13	CL	"	"	500	34.9	35.4	110	6.1x10^{-11}
/14	CL	"	"	500	32.3	32.7	100	5.6x10^{-11}
/15	CL	"	"	720	41.0	-	-	-
/16	CL	"	"	720	38.5	-	-	-
/17	CL	"	"	720	39.6	-	-	-
/18	CL	"	"	720	41.4	-	-	-
"A"/49		1M Carb/Bicarb	-750	290	26.1	-	-	-
/50		"	"	290	30.1	-	-	-
/65		"	"	500	50.1	52.6	330	1.8x10^{-10}
/66		"	"	500	48.1	50.6	360	2.0x10^{-10}
"O"/4	CC	CO$_2$ + H$_2$O	free corr	150	29.3	-	-	-
/21	LC	"	"	430	37.0	-	-	-
/22	LC	"	"	430	36.0	-	-	-
"A"/63		CO$_2$ + H$_2$O	free corr	340	65.3	(-)	(30)	(-)
/64		"	"	340	51.4	(-)	(30)	(-)
"R"/57		CO$_2$ + H$_2$O	free corr	360	55.4	(-)	(30)	(-)
/60		"	"	360	50.7	(-)	(20)	(-)
"O"/19	CL	CO$_2$+NaHCO$_3$	-400	500	41.4	-	-	-
/20	CL	"	"	500	32.7	-	-	-
"O"/23	LC	3.5M NaOH	-1000	360	41.9	44.2	360	4.7x10^{-10}
/24	LC	"	"	430	38.6	43.7	980	6.3x10^{-10}
/25	CL	"	"	360	41.5	46.8	990	7.6x10^{-10}
/26	LC	"	"	430	37.0	41.3	920	5.9x10^{-10}
/34	CC	"	"	500	26.2	29.0	847	4.7x10^{-10}
/36	CL	"	"	500	35.2	44.2	1460	8.1x10^{-10}
/37	CL	"	"	500	28.5	30.9	640	3.6x10^{-10}
/38	CC	"	"	500	34.5	38.4	730	4.1x10^{-10}
"A"/45		3.5M NaOH	-1000	460	54.8	56.0	200	1.2x10^{-10}
/46		"	"	460	44.9	45.7	150	9.3x10^{-11}
/47		"	"	500	44.2	44.7	100	5.6x10^{-11}
/48		"	"	500	41.1	42.1	190	1.0x10^{-10}
"R"/53		3.5M NaOH	-1000	500	40.0	-	-	-
/54		"	"	500	39.0	-	-	-
/55		"	-950	500	47.4	52.2	660	3.7x10^{-10}
/56		"	"	500	48.8	54.3	690	3.8x10^{-10}
"O"/61	CC	3.5M NaOH	-650	460	36.5	-	-	-
/62	CL	"	"	460	37.8	38.2	50	3.0x10^{-11}
"O"/29	LC	3.5M NaOH	-400	770	39.0	39.9	170	6.0x10^{-11}
/30	LC	"	"	770	49.2	51.7	360	1.3x10^{-10}
"O"/31	CC	3.5M NaOH	-150	500	36.5	37.5	210	1.2x10^{-10}
/32	CC	"	"	500	36.9	37.9	210	1.2x10^{-10}
"O"/33	CC	3.5M NaOH	∓ 0	500	31.7	40.1	60	3.3x10^{-11}
/35	CC	"	"	500	39.9	40.7	130	7.2x10^{-11}
"A"/43		3.5M NaOH	-870	500	38.3	38.7	50	2.9x10^{-11}
/44		"	"	500	40.6	40.8	20	8.9x10^{-12}
"A"/51		3.5M NaOH	-150	460	56.1	56.5	40	2.4x10^{-11}
/52		"	"	460	48.6	49.0	40	2.4x10^{-11}
"O"/39	CC	0.35M NaOH	-1000	500	33.8	-	-	-
/41	CC	"	"	500	35.4	-	-	-
"O"/27	LC	0.35M NaOH	-870	770	36.9	-	-	-
/28	LC	"	"	770	40.9	-	-	-

Figure 62 : Stress intensity vs. crack velocity for steels "A", "R" and "O". SCC-tests in 3.5M NaOH at the active peak potential (around -1000 mV_{SCE})
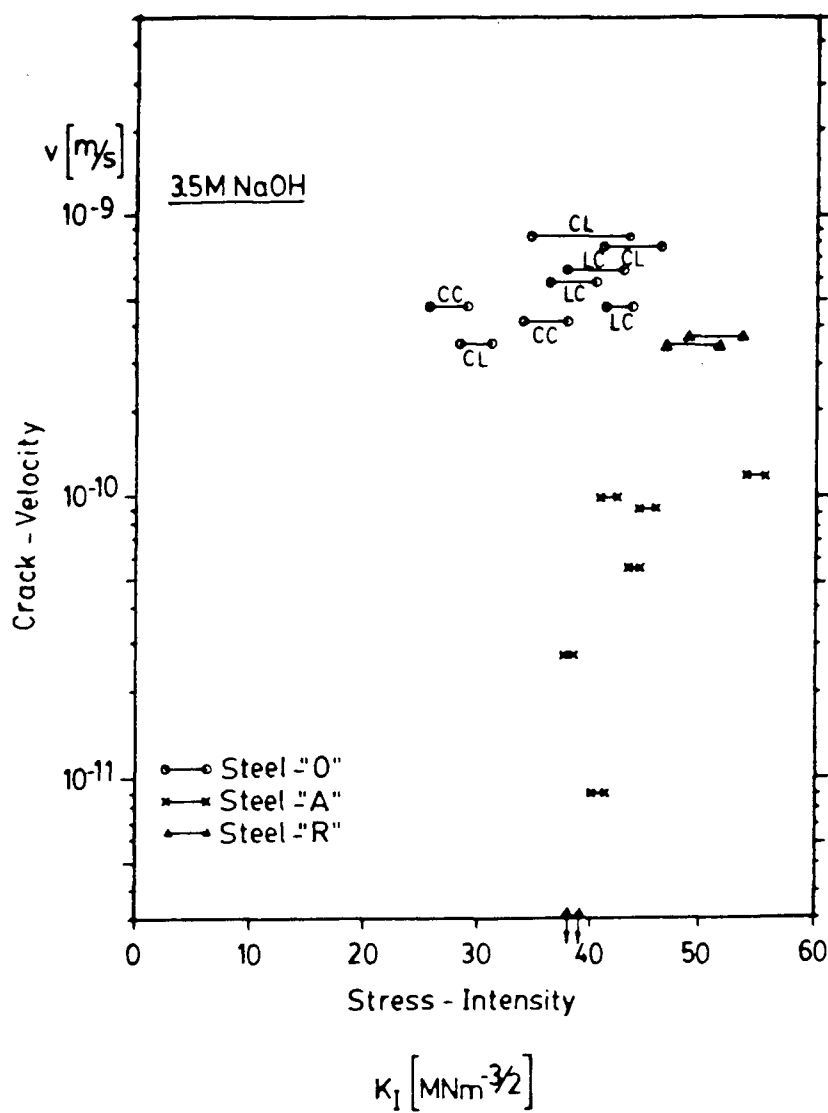
For steel-"O" (and "A"), the influence of test potential on the cracking rate is illustrated in Fig.63, pg. 87. The potential was varied between 0 and $-1000mV_{SCE}$. The stress intensity was chosen around 35 $MNm^{-3/2}$ for steel "O" and around 46 $MNm^{-3/2}$ for steel "A".

Steel-"O" seemed to show maximum crack growth rates at the active peak at $-1000mV_{SCE}$ and at the peak in the passive region at $-150mV_{SCE}$. The difference between the cracking rates at the two peaks was less than one order of magnitude. Lower cracking rates were found between the two peaks and above $-150mV_{SCE}$. For comparison most tests were done with "CC"-specimens.

For steel-"A", not many measurements were done. However, the cracking rate at $-1000mV_{SCE}$ seemed to be only about 4 times higher than at $-150mV_{SCE}$.

Steel "O" was also tested in 0.35M NaOH but no cracking was found at either $-1000mV_{SCE}$ or $-870mV_{SCE}$. Both tests were run at stress intensities where cracking occurred in the more concentrated solution.

Figure 63 : Potential vs. crack velocity for steels "A" and "O" in 3.5M NaOH, SCC-test
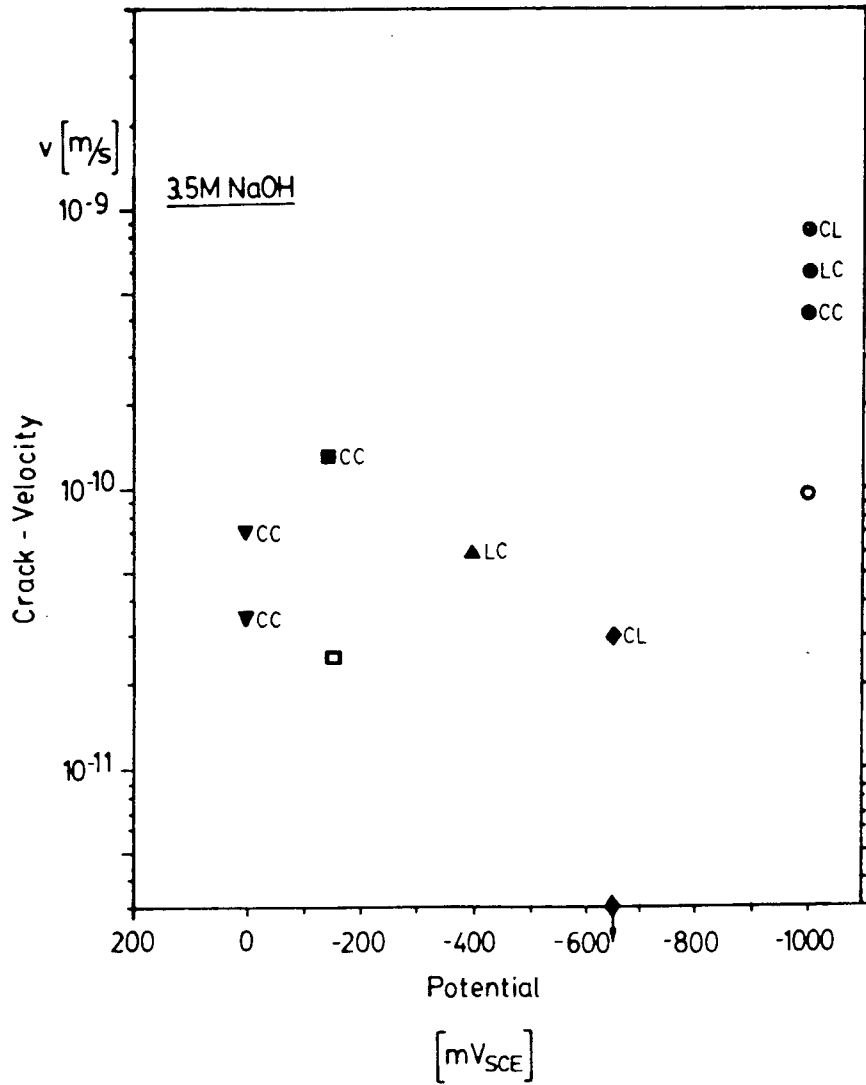
Steel-"O"
- ● - 1000 mV$_{SCE}$
- ◆ - 650 mV
- ▲ - 400 mV
- ■ - 150 mV
- ▼ 0 mV

$(K_I = 32 - 40\, MNm^{-3/2})$

Steel- "A"
- ○ - 1000 mV$_{SCE}$

- □ - 150 mV

$(K_I = 44 - 48\, MNm^{-3/2})$

3.3.3. Fractography

Steel-"A" (3.5%NiCrMoV, super clean)

In both the 3.5M NaOH and the 1M carbonate/bicarbonate solutions, intergranular cracking was observed at all potentials investigated. In the sodium hydroxide solution, however, the appearance of the intergranular fracture surface varied with the testing potential. At $-1000mV_{SCE}$ (active peak) the individual grains on the fracture surface were hardly attacked by the environment whereas at $-150mV_{SCE}$ (transpassive peak) strong etching (or pitting) of the whole fracture surface was observed. (Compare Figures 64 and 65 on page 91). In the carbonate/bicarbonate solution, a strong corrosive attack of the grains occurred at the crack mouth whereas smoother grain surfaces were found at the crack tip (compare Figures 66 and 67, pg. 92). Even when the crack path in all solutions was intergranular, some tests at higher stress intensities (above 55 $MNm^{-3/2}$) showed mixed cracking (intergranular/transgranular).

Steel-"R" (3.5%NiCrMoV)

Steel-"R" was tested only in 3.5M NaOH at the active peak potential and gave a fracture appearance similar to steel-"A".

Steel-"O" (1%CrMoV)

The determination of the crack path in all tests was rather difficult. This could be due to the mixed ferritic/bainitic microstructure. Most probably both intergranular and transgranular cracking occurred. (Compare Figures 68 and 69, pg. 93). In the 3.5M NaOH solution, once again, a strong influence of the potential on the appearance of the fracture surface was observed. At the transpassive peak potential of $-150mV_{SCE}$, a much stronger attack on the grain surface occurred than at the active peak potential of $-1000mV_{SCE}$. (Compare Figures 71, 72 and 73 , pg. 94). At the test potentials between the two peaks, a stronger corrosion attack was observed compared to the tests at $-1000mV_{SCE}$.

As mentioned earlier, Steel-"O" cracked only in 3.5M NaOH with three cracking exceptions in the carbonate/bicarbonate solution. Figure 74 on page 95 shows the fracture surface at the crack tip in the carbonate/bicarbonate solution, which looks very similar to the fracture surface in the NaOH solution at $-1000mV_{SCE}$ (Compare Fig.73, pg.94). From the rounded crack tip, it may be concluded that the crack propagation was mainly a dissolution process.

Earlier it was stated that the orientation of the crack plane did not have a big influence on the propagation rate. Figures 75 and 76 on page 95 show two cases where MnS inclusions were laying in the crack plane ("CL"-direction). Both pictures show the tip of the stress corrosion crack.

In Figures 75 (3.5M NaOH, -1000mV$_{SCE}$) the crack front seems not to be influenced by the presence of the inclusion. From Figure 76 (1M carbonate/bicarbonate,-750mV$_{SCE}$), on the other hand, one could conclude that the crack propagated further in the vicinity of the inclusion. However, this "additional" cracking was only observed very close to the inclusion and may not have markedly influenced the overall cracking behavior. In both examples no change in fractography adjacent to the inclusions was observed.
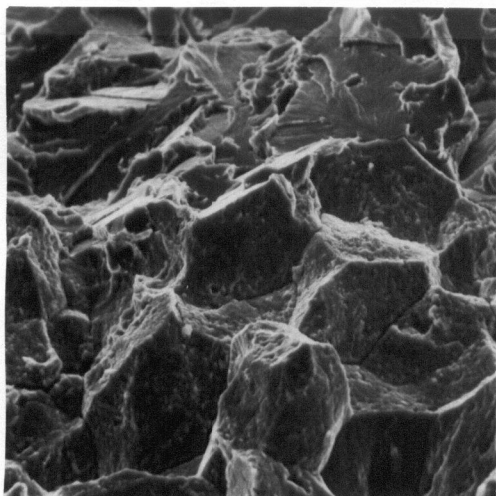
Figure 64:

SEM-picture, crack tip with intergranular fracture surface, steel "A" tested in 3.5M NaOH at -1000 mV$_{SCE}$, SCC-test

At the top: overload fracture in liq. Nitrogen

Mag.: 1,200x
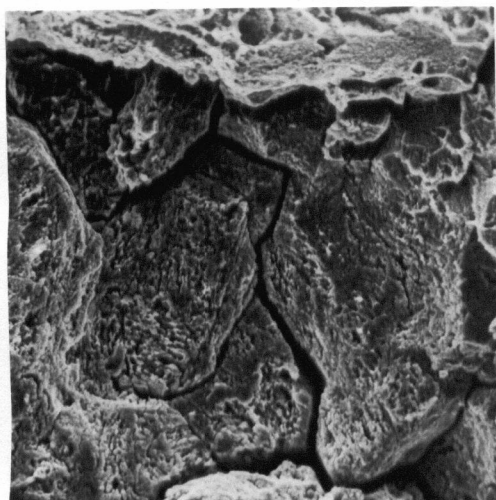
Figure 65:

SEM-picture, strongly etched intergranular fracture surface, steel "A" tested in 3.5M NaOH at -150 mV$_{SCE}$, SCC-test

Mag.: 1,200x
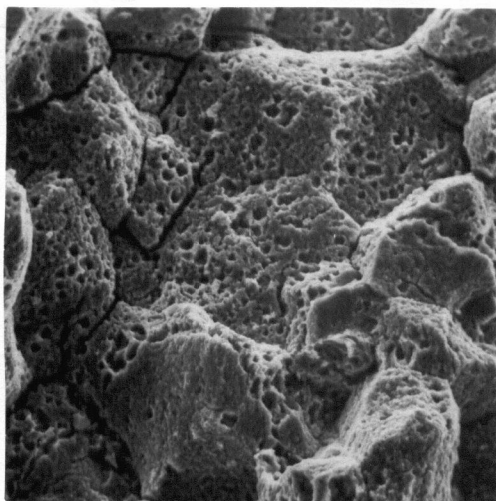
Figure 66:

SEM-picture, pitted intergranular
fracture surface at the crack
mouth, steel "A" tested in
1M $NaHCO_3$ + 1M Na_2CO_3 at
-750 mV_{SCE}, SCC-test
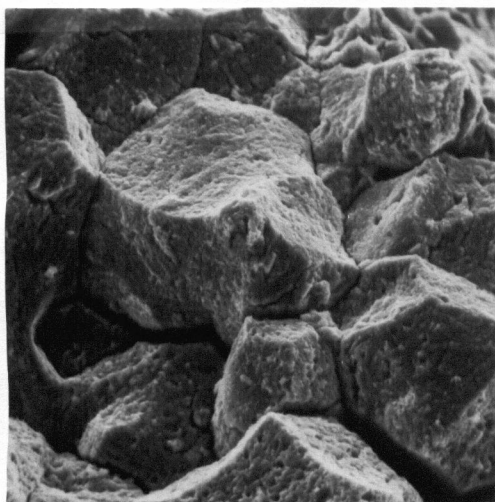
Mag.: 1,700x

Figure 67:

SEM-picture, intergranular
fracture surface, at the crack
tip, steel "A" tested in
1M $NaHCO_3$ + 1M Na_2CO_3 at
-750 mV_{SCE}, SCC-test

Mag.: 1,700x
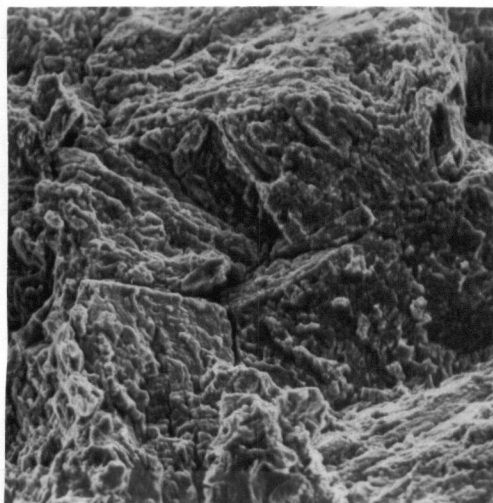
Figure 68:

SEM-picture, strong corrosive attack of the intergranular fracture surface, steel "O" tested in 3.5M NaOH at -1000 mV$_{SCE}$, SCC-test
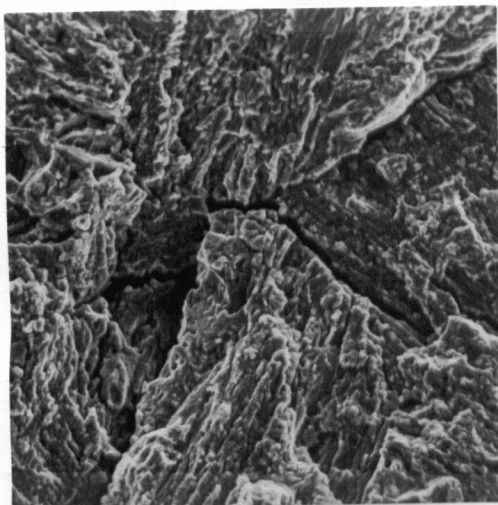
Mag.: 800x

Figure 69:

SEM-picture, transgranular facture appearance, steel "O" tested in 3.5M NaOH at -1000 mV$_{SCE}$, SCC-test

Mag.: 800x
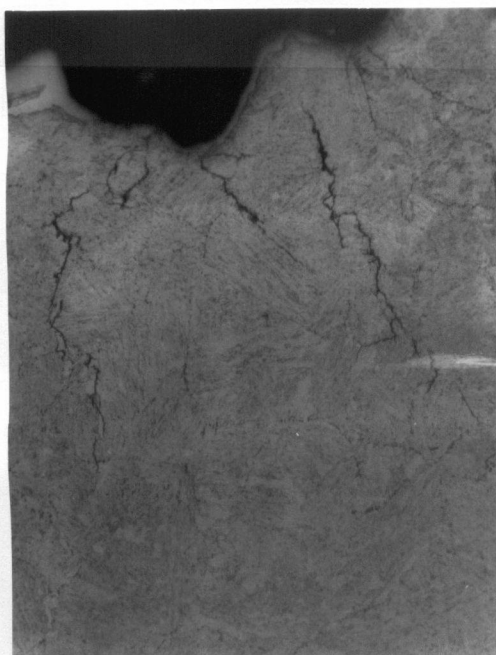
Figure 70:

Secondary cracks, steel "O" tested in 3.5M NaOH at -1000 mV$_{SCE}$, SCC-test

Mag.: 200x, etched
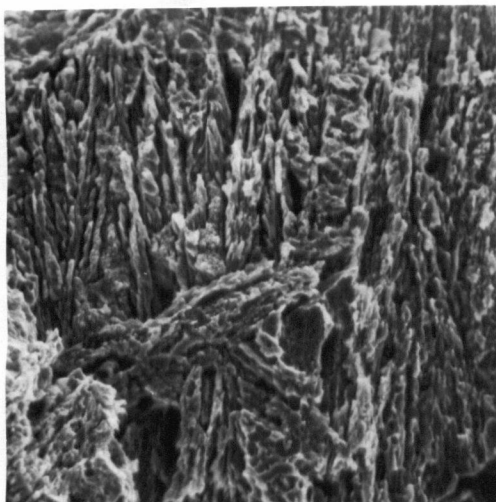
Figure 71:

SEM-picture, strongly attacked
fracture surface, steel "O"
tested in 3.5M NaOH at
-150 mV_{SCE}, SCC-test
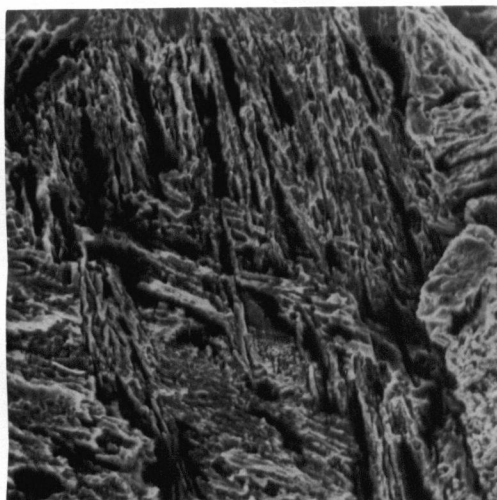
Mag.: 900x

Figure 72:

SEM-picture, strongly attacked
fracture surface, steel "O"
tested in 3.5M NaOH at
-150 mV_{SCE}, SCC-test

Mag.: 1,000x
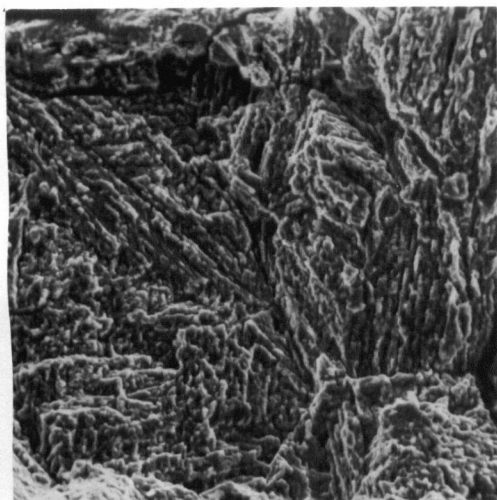
Figure 73:

SEM-picture, fracture surface,
steel "O" tested in 3.5M NaOH
at -1000 mV_{SCE}, SCC-test

Mag.: 900x
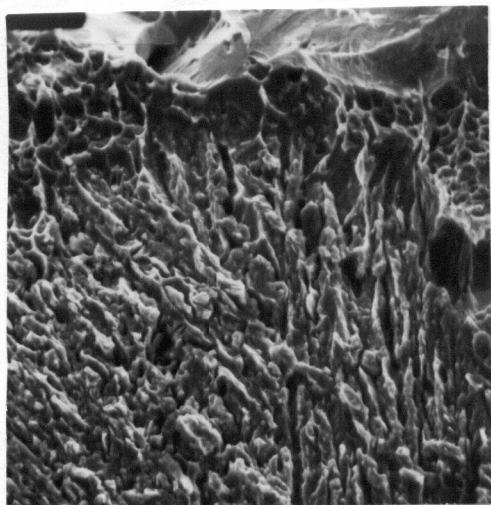
Figure 74:

SEM-picture, rounded crack tip (at the top), with strongly attacked fracture surface, steel "O" tested in 1M $NaHCO_3$ + 1M Na_2CO_3 at -750 mV_{SCE}, SCC-test

Mag.: 1,000x
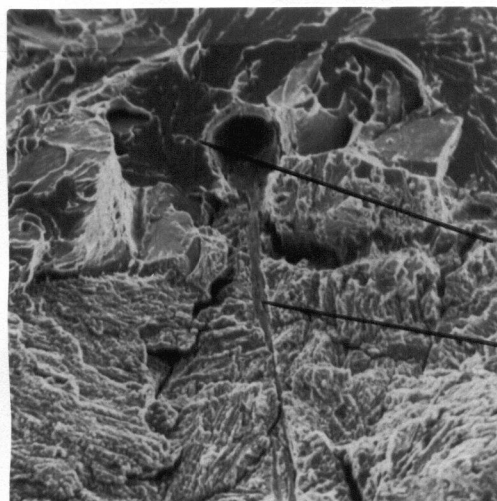
Figure 75:

SEM-picture, crack tip with MnS inclusion (dissolved away), steel "O" tested in 3.5M NaOH at -1000 mV_{SCE}, SCC-test

Crack front is not influenced by the inclusion

MnS inclusion

Mag.: 500x
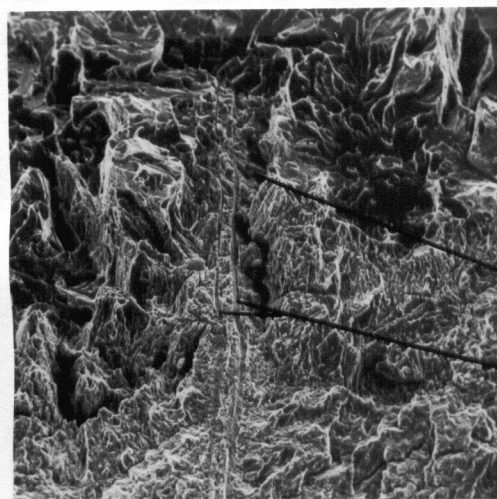
Figure 76:

SEM-picture, crack tip with MnS inclusion (dissolved away), steel "O" tested in 1M $NaHCO_3$ + 1M Na_2CO_3 at -750 mV_{SCE}, SCC-test

Crack propagated further in the vicinity of the inclusion

MnS inclusions

Mag.: 200x

3.3.4. Crack path

Strong crack branching was observed in all SCC-tests. Normally, two main cracks propagated from the tip of the fatigue crack at an angle of about 60° to the crack plane of the fatigue crack and then branched further into smaller cracks. This cracking effect is described by Brown[59] and was explained with the shape of the plastic zone at the crack tip. He observed that in bend-bar stress-corrosion-tests, the crack tends to follow the elastic/plastic interface formed at the crack tip. Green and Mundy[61] did a theoretical and experimental analysis of the plastic zone in the notched bend specimen and found that the elastic/plastic interface ahead of the crack tip has an elliptical shape. The observed crack branching angle during our SCC tests were consistent with these observations and explanations.

An example of crack branching observed in steel "A" is given in Figure 77 below.
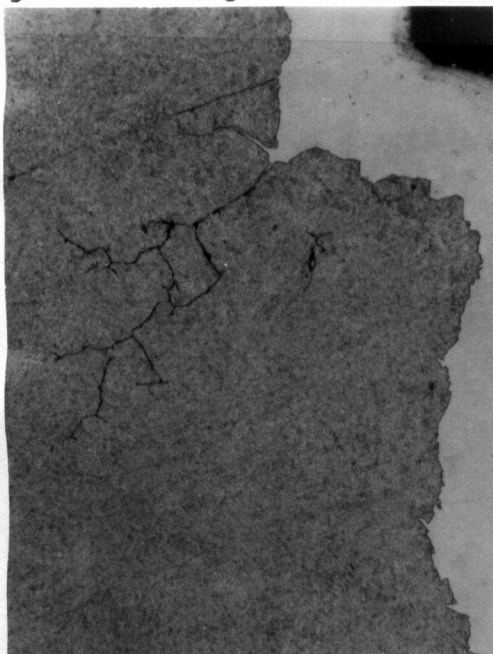
Figure 77:

Crack branching, steel "A" tested in 3.5M NaOH at -1000 mV$_{SCE}$, SCC-test

At the top: vertical fatigue precrack

SCC cracks

At the bottom right: overload overload fracture

Mag.: 220x
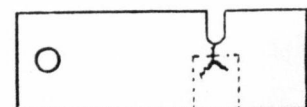
3.3.5. <u>Dynamic SCC-test</u>

A slow loading rate fracture mechanics test was employed to explain the different findings of SCC experiments and SSRT experiments with steel-"O". In the 1M carbonate / bicarbonate solution, very severe cracking was found with the SSRT-test, whereas the conventional statically loaded fracture mechanics experiments gave no cracking beside a few exceptions.

The dynamic test set up was analogous to a regular SCC test, but instead of applying a constant load, the sample was pulled slowly to failure. The crosshead speed was the same as during the SSRT-tests which corresponded to a stress intensity increase rate of about 1.5 $MNm^{-3/2}$ per hour.

The test was started at zero load and was run for about 48 hours. Therefore the stress intensity at the end of the test would be much higher than the K_{IC} value found by testing this steel in air. The reasons for this are crack blunting and crack branching during the test.

In the SSRT experiments (1M carbonate / bicarbonate, -750mV$_{SCE}$) with a duration of about 24 hours, a crack length of about 0.16mm was obtained. From the fracture surface of the dynamic SCC-test a maximum crack length of about 0.05mm could be observed and the fracture surface was not similar to the fracture surface obtained with the SSRT-test. (Compare Fig. 78, 79 below and SSRT Fig.60, pg. 79).

In the dynamic SCC test, a strong corrosive attack could be observed and it is not very clear if the crack advanced by stress corrosion cracking or by some dissolution mechanism.

The same experiment was run in a CO_2/H_2O environment at the free corrosion potential. No cracking or dissolution at the crack tip could be found at all.
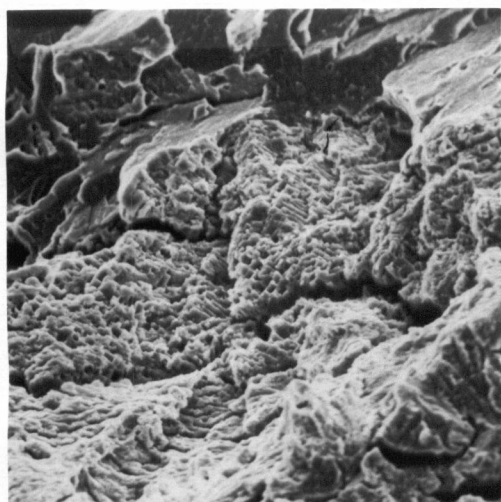
Figure 78:

SEM-picture, crack tip after dynamic SCC-test, steel "O" in 1M $NaHCO_3$ + 1M Na_2CO_3 at -750 mV_{SCE}

At the top: overload fracture
Mag.: 1,000x
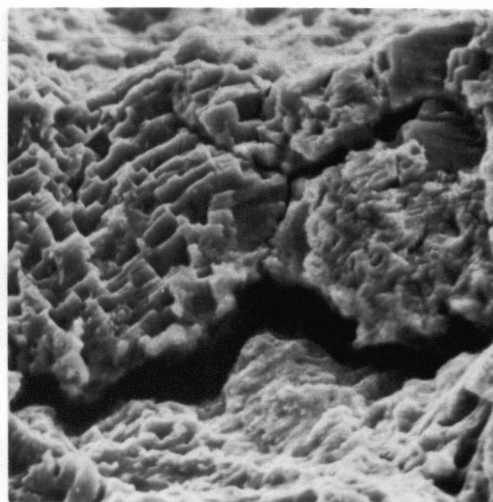
Figure 79:

SEM-picture, crack tip after dynamic SCC-test, steel "O" in 1M $NaHCO_3$ + 1M Na_2CO_3 at - 750 mV_{SCE}

At the top: overload fracture
Mag.: 3,200x

IV. DISCUSSION

4.1. Interpretation of polarization curves

4.1.1. Carbonate solution

The E-pH diagram[62] of iron in water at 100°C (Fig. 80), indicates, that passivity is difficult to achieve at pH <4.5, except at higher oxidizing potentials. With this, passive behavior was not observed in the acidic CO_2/H_2O solution

Figure 80 : E-pH diagram of iron in water at 100°C
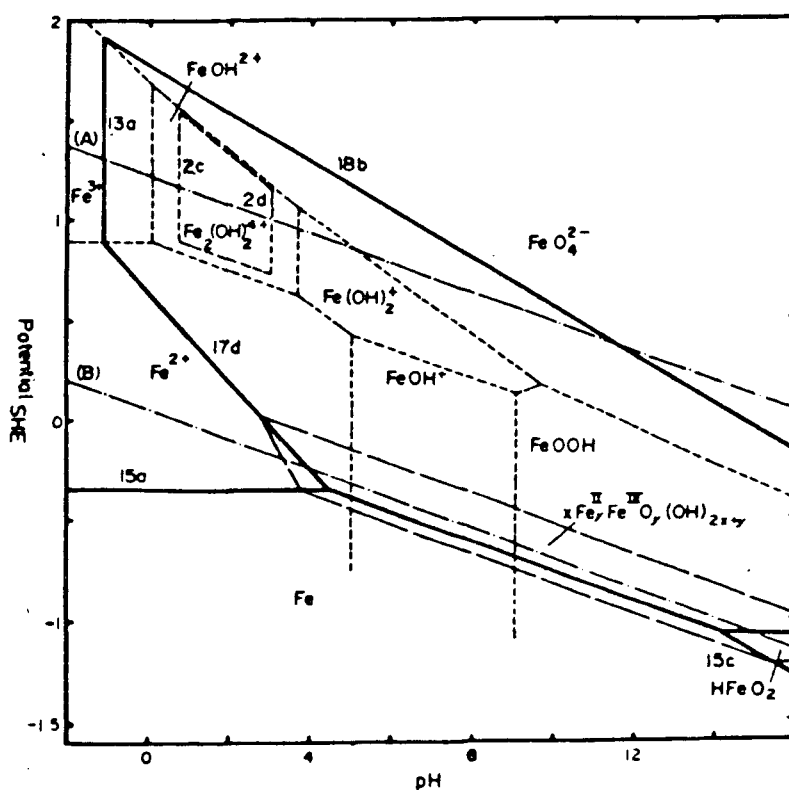
By adding $NaHCO_3$ to the solution the pH is raised. Oxide films can now form at much lower potentials which means that passivation behavior is possible. The occurrence of different active peaks (compare Figures 44-47, pg.64,66) suggests that several reactions occured place and the composition of the passive film changed as the potential was raised from negative (active)to more positive (noble) potentials.

Several authors have studied the film formation on mild steel in carbonate/bicarbonate solutions[63-67]. The following possible passivation processes were suggested and it is assumed that similar reactions could have taken place on the rotor steel.

At low concentrations of carbonate ions (below 10^{-3} mol/l), the principal oxide films on the metal surface are Fe_3O_4 at lower potentials and Fe_2O_3 at higher potentials. At carbonate concentrations above about 1 mol/l, $FeCO_3$ and Fe_2O_3 are the main oxidation products, where the latter is again formed at higher potentials. At concentrations in between, a mixture of Fe_3O_4 and $FeCO_3$ are found at lower potentials and Fe_2O_3 at higher potentials.

Thomas et al[6] proposed that the following reaction sequence takes place in bicarbonate solutions as the potential is raised from the free corrosion potential in the noble direction:

At potentials just below the first active peak the following reaction (7) dominates which is independent of bicarbonate concentration:

$$Fe + 2H_2O \longrightarrow Fe(OH)_2 + 2H^+ + 2e^- \quad ...(7)$$
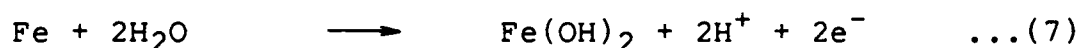
By raising the potential further, $FeCO_3$ forms either by attack of the $Fe(OH)_2$ (8) or by direct reaction with Fe (9):

$$Fe(OH)_2 + HCO_3^- \longrightarrow FeCO_3 + H_2O + OH^- \quad ...(8)$$

$$Fe + HCO_3^- \longrightarrow FeCO_3 + H^+ + 2e^- \quad ...(9)$$
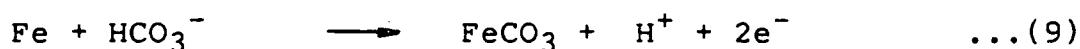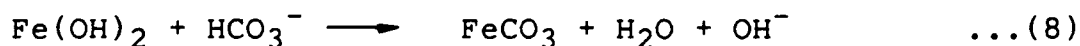
At the first active peak, passivation occurs due to a partial coverage of the metal surface with $FeCO_3$ and partial coverage with Fe_3O_4 following the reaction (10).

$$3Fe(OH)_2 \longrightarrow Fe_3O_4 + 2H_2O + 2H^+ + 2e \quad ...(10)$$
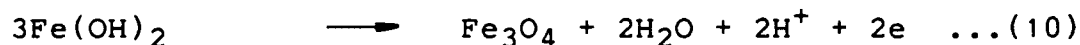
(Where the ratio of Fe_3O_4 to $FeCO_3$ is controlled by the concentration of bicarbonate)

The second peak is caused by the oxidation of the $FeCO_3$ (11) and Fe_3O_4 (12) to an Fe(III) film namely Fe_2O_3:

$$2FeCO_3 + 3H_2O \longrightarrow Fe_2O_3 + 2CO_3^{2-} + 6H^+ + 2e^- \quad ..(11)$$

$$2Fe_3O_4 + H_2O \longrightarrow 3Fe_2O_3 + 2H^+ + 2e^- \quad ...(12)$$
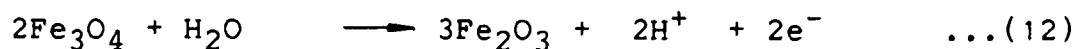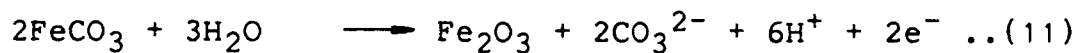
Figure 81: Discussion of the polarization curve in terms of chemical reactions in the Bicarbonate+Carbonate solutions
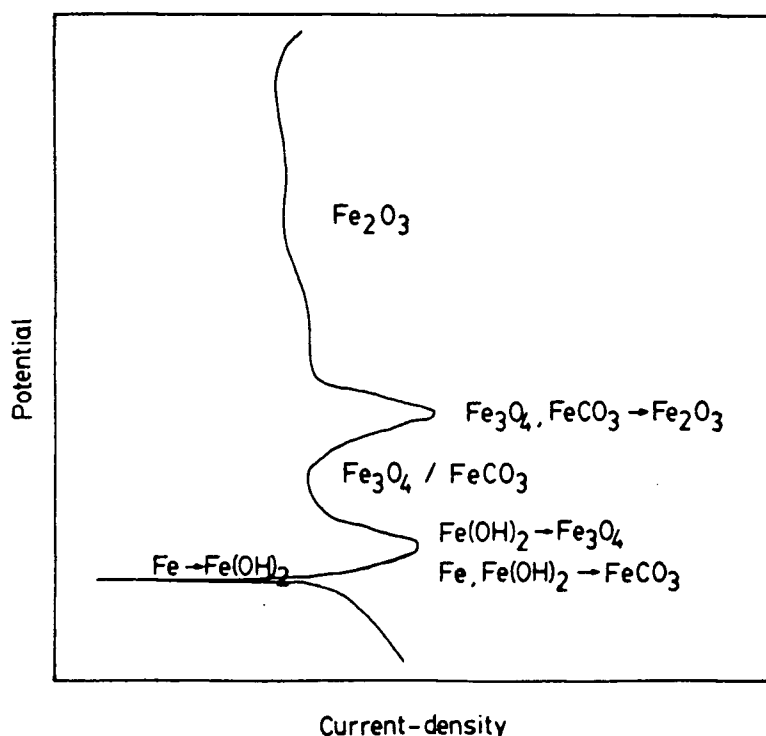
The occurence of only the first active peak at low concentration of bicarbonate was explained by Thomas[63] as being due to the very slow oxidation of ferrous carbonate at the low pH of these solutions. This could also explain why in the $3.5 \cdot 10^{-2}$ molar bicarbonate solution the second peak was observed only with the slower scan rate.

The appearance of only the first active peak in the 1 molar carbonate/bicarbonate solution is explained[64] by the inhibition of film breakdown at the transition from a protective $FeCO_3/Fe_3O_4$ film to the protective Fe_2O_3 film.

The transpassive peak was consistent with the dissolution of Cr. The aqueous thermodynamics of the Cr/H_2O system[68] shows that the chromium oxides dissolve at higher potentials.

In Figures 43 and 47, pg. 64.66, all three steels are compared in the CO_2/H_2O solution and in the carbonate/bicarbonate solution. The reason why steel "O" showed the lowest current density at the transpassive peak may be explained by its lower chromium content and the lack of a heat treatment which can cause chromium enrichment of the metal carbides. The higher current density in the passive "plateau" of steel-"O" could be due to a less protective film because of smaller chromium and nickel contents compared to the "A" and "R" steels. At the active peak in the carbonate/bicarbonate solution steel, "A" and R" showed practically no difference whereas in the passive region steel "R" gave slightly higher current densities.

In the CO_2/H_2O solution steel "R" and "A" gave much higher corrosion currents than steel "O", and again steel "R" gave higher current densities than "A". The reasons for this could be the difference in microstructure, heat treatment (segregation phenomena), alloy composition or the

inclusion composition. More experiments are, therefore, necessary to clearly explain these observations.

4.1.2. Sodium hydroxide solution

Agrawal et al[40] investigated the polarization behavior of Fe-Ni-Cr alloys in sodium hydroxide solutions and Crowe et al[69] studied SCC of stainless steel in caustic solutions. Also the behavior of iron and mild steel in sodium hydroxide solution was studied by several researchers[70-73]. Even so, not exactly the same steels were investigated as were used in our experiments, still very similar polarization curves were obtained. Agrawal and Crowe found that the significant features of the curves for Fe-Ni-Cr alloys depend on the characteristic features of the pure components iron, nickel and chromium.

Therefore, I consider polarization in the anodic direction, the first active peak (sometimes observed as double peak) above the free corrosion potential can be attributed to the dissolution of iron at the lower and nickel at the higher potential. The following passive region is due to a protective (Fe,Ni,Cr) -oxide film. The peak following this passive region (transpassive peak) is found to be due to the dissolution of chromium. At potentials more positive than the transpassive peak an (Fe,Ni) oxide film is responsible for the passive behavior. (Compare Figure 82)

Figure 82: Discussion of the polarization curve in terms of chemical reactions in the sodium hydroxide solutions
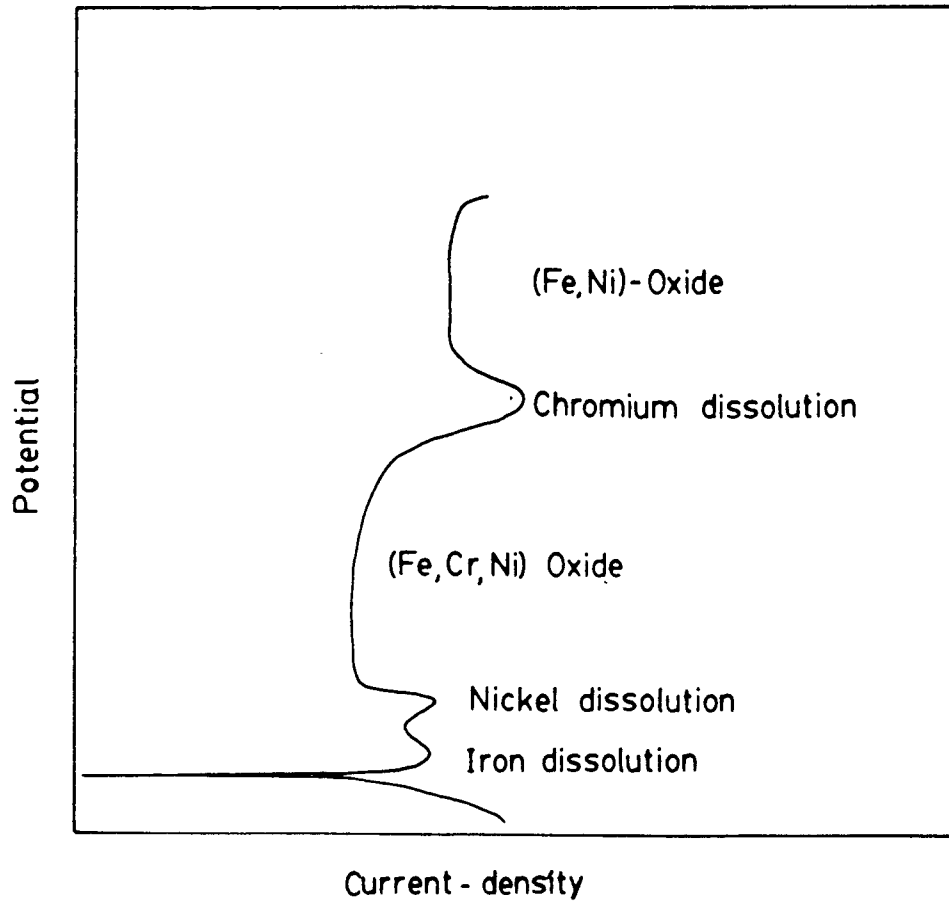
In Fig.48, pg.68, it can be seen that all three steels behaved very similarly in the sodium hydroxide solution. The current densities at the transpassive peak were comparable to the current densities found in the carbonate/bicarbonate solution. However, the peak currents at the active peak were about 10 times lower in the sodium hydroxide solution and both the active and transpassive peaks were displaced 200mV towards more negative potentials. These effects were mainly due to the different pH of the solution. At potentials above and below the transpassive peak, steel "O" seems to show slightly higher current densities compared to "A" and "R", which was also observed in the carbonate/bicarbonate solution. The active peak (double peak) appeared slightly different for steel-"O" as compared to "A" and "R". In steel-"O" the second nose, which is attributed to nickel dissolution was smaller. This may, therefore, be explained by the considerably lower nickel content of steel-"O".

In all test solutions the free corrosion potential for steel-"O" was slightly more negative than both steels "A" and "R".

In the acidic CO_2/H_2O solution, it was found that steels "A" and "R" gave very much higher current densities than steel "O". However in the carbonate/bicarbonate and sodium hydroxide solutions similar current densities were observed at the active peak. Therefore, different

dissolution processes may be occurring on each steel in the alkaline and acidic solution respectively.

With the remelted steel "R" (doped with inclusions), it was found that the transpassive peak did not appear in the as cast ot hot rolled condition but only in the heat treated condition. Since this peak is attributed to chromium dissolution, an enrichment of chromium at certain locations must take place during the heat treatment. The analysis of the carbides (compare chapter 2.2.8. on page 33) showed an enrichment in alloying elements. Therefore, at the transpassive peak a preferential dissolution of chromium rich carbides may take place. As mentioned earlier, no major difference in polarization behavior between the CaS doped steel and the MnS doped steel was visible. The difference in current densities at the active peak between the "R"-steel and both doped steels may be caused by the inclusions. However, since the microstructure of the doped steel is not exactly the same as the "R"-steel, these conclusions are not completely verified In further studies, "R"-steel needs to be tested in the remelted and heat treated state but without any additions of inclusions.

The decreased current density at the transpassive peak during the second polarization test in Fig.49, pg.68 may be attributed to the dissolution of most chromium carbides on the metal surface during the first test.

4.2. Slow strain rate vs. fracture mechanics tests

As mentioned in the introduction, SSRT tests are used for fast determination of sensitivity to stress corrosion cracking. Questions often arise as to whether findings from SSRT-tests can really be applied to samples with precracks. In most cases suspicion only arises when no cracking is found in the SSRT-test, because one worries about a probable lack of initiation sites. In our experiments mainly the reverse was found and many cracking signs in SSRT-tests could not be reproduced in the fracture mechanics tests. A possible explanation for this is given by Herbsleb et al [74,75] who found that in some metal/environment systems SCC only occurs when a critical loading - or strain rate is present, which allow a certain plastic deformation at the crack tip. Brose[76] also related strain at the crack tip to SCC and compared the SCC initiation resistance of smooth and notched samples.

Takemoto[77] combined the slow strain rate idea with fracture mecanics tests (analogous to our "dynamic" SCC experiment) and found a method for a quick determination of K_{ISCC} values. He found a critical loading rate below which the stress-intensity for stress corrosion crack initiation no longer was dependent on the loading rate.

With these explanations for stress corrosion cracking one could explain why, for example, steel-"O" showed no cracking in the static fracture mechanics test (1M $NaHCO_3$ /

1M Na_2CO_3) and only little cracking (if any) in the dynamic fracture mechanics tests. According to Takemoto's findings, the strain rate during the dynamic test must have been too fast to show appreciable cracking. In the static test the plastic flow conditions at the crack tip may not have been sufficient for any film rupture mechanism to take place and even higher stress intensities (approaching K_{IC}) would be necessary for cracking. Another factor could be the conditions of the environment (potential, pH) at the crack tip which may have been quite different in the SSRT-test (short crack) as compared to the fracture mechanics test (long crack). This could be responsible for the relative little cracking of "A" and "R" steels in the SSRT-test with NaOH solutions, whereas with the precracked samples severe cracking was found in both steels. Also, differences in environment conditions may have accounted for the observations in 1M carbonate/bicarbonate (compare Fig. 67,68, pg.92) where the corrosive attack at the crack tip was quite different from the crack mouth. This may be partially explained with the longer exposure time of the crack mouth to the environment than that of the crack tip, but diffusion controlled differences in environmental conditions could have caused this difference because of the narrow crack geometry.

From these results, it can be seen how very important the combination of environment (incl. potential) material

and stress state can be for stress corrosion cracking to occur.

The blunting observed with steel "A" and "R" in the CO_2/H_2O solution during the fracture mechanics test can be explained by strong corrosive attack, with no passivation. Steel-"O" showed no cracking in this solution at all. From the polarization curves (Fig.43, pg.64) it can be seen that steel "A" and "R" give about 10 times higher corrosion currents than steel-"O" and therefore perhaps the corrosive attack at the crack tip was noticed only in the two 3.5%NiCrMoV steels. If the crack blunting was due to a pure dissolution process, then the "crack-advance" (v) should be related to the anodic current density via Faraday's law of electrolysis:

$$v = i \cdot W' / F \cdot p \qquad \qquad ...(13)$$

where F = Faraday constant ($9.65 \cdot 10^4 A \cdot s$ equiv^{-1})

      p = density of the alloy ($8.0 \cdot 10^3 kgm^{-3}$)

      W' = equivalent weight of alloy

      i = anodic current density

      v = crack velocity

At 95°C and the free corrosion potential in CO_2/H_2O, v = $2.4 \cdot 10^{-11}$ m/s , W' = $2.8 \cdot 10^{-2}$ kg (based on oxidation state of Fe^{2+}). A calculation of the anodic current density (i) with these values gives about 0.7 A/m^2. This value is in good agreement with an anodic current density (Tafel

extrapolation of polarization curve) of about 1-1.5 A/m^2 found from polarization curves of steel "A" and "R" (Compare Fig.43, pg.64)

4.3. Comparison with Literature data

Most stress corrosion cracking data relating to carbonate/bicarbonate solutions was obtained on mild steel or high strenth low alloy (HSLA) line pipe steel. Tests were mainly conducted with the constant load or SSRT-technique[25,27,28,30,41,78].

The potential where cracking was observed lies between about -600 to -800mV$_{SCE}$, depending on temperature and pH. Cracking in this range is reported to be intergranuler for the mainly ferritic microstructures and maximum crack velocities are reported[27,30] as $2 \cdot 10^{-9}$m/s. This compares well with our SSRT-tests studies, but, additionally, we found similar cracking velocities at much more noble potentials. No published data were found to compare with the cracking rates of fracture mechanics samples in the carbonate/bicarbonate solution.

In the acidic CO_2/H_2O system, investigations have been conducted on low alloy steels[26] and on 3.5%NiCrMoV steels[38,39]. In the low alloy steels, cracking was found only at high CO_2 pressures and elevated temperatures. No quantitative cracking results were given.

In SSRT-tests, Mueller[38] observed a strong corrosive attack of the specimen with many secondary cracks. The fracture surface showed no intergranular cracking. These findings are comparable with our results since testing conditions were very similar. However, Speidel[39], found intergranular SCC in CO_2 containing water at 160°C when using fracture mechanics tests. Maximum cracking rates of $7 \cdot 10^{-10}$ m/s were reported. In our experiments at 95°C no cracking was detected, but rather strong crack tip dissolution took place. From the mechanical testing of our steel, no major difference in the plastic deformation behavior at 95°C and 160°C could be found. Therefore, differences between Speidel's results and the present study could be due to environmental effects. For example, a higher pH of the solution may have allowed passive film formation and prevented strong general corrosive attack. Our intergranular cracking rates of $2 \cdot 10^{-10}$ m/s obtained in the 1M carbonate/bicarbonate solution would be comparable to the findings of Speidel in the CO_2/H_2O system.

In caustic sodium hydroxide solutions, tests of rotor steels have been reported with SSRT, constant load, and fracture mechanics techniques[2,3,34,79]. From SSRT-tests, it was found that the minimum NaOH concentration required to produce SCC decreases with increasing temperature. Cracking was observed at 65°C above 0.8 Mol/lt and at 160°C above $3 \cdot 10^{-2}$ Mol/lt cracking was observed. At constant NaOH concentration the crack growth rates decreased with

decreasing temperature. At 160°C crack growth rates of $4 \cdot 10^{-10}$m/s to $3 \cdot 10^{-8}$m/s were found with precracked samples in 0.3 molar NaOH solutions. The crack path was intergranular[3]. Somuah et al[34] did slow strain rate tests at 120°C in 12M NaOH, with additions of NaCl, and found no sign of an intergranular crack path. The tests were done at the free corrosion potential. At more noble potentials, at the active peak and in passive regions, intergranular fracture was found. With fracture mechanics tests, intergranular corrosion was found at the free corrosion potential. Crack growth rates were calculated to be $\approx 10^{-8}$m/s.

Since most of the so far mentioned experiments (not including the present study) were done either at higher temperatures or with stronger NaOH solutions than our study, higher cracking rates were obtained in comparison to our measurements. However, both the crack path and cracking in the passive region was confirmed by our experiments. Estimated crack growth rates from cracked low pressure rotor discs[1,2,36] compare well with our results. In general, a large scattering of data is reported for service failures becouse crack velocities are estimated from the time of service, which does not include any incubation time for cracking or the effect of a changing K_I on growth rates. Typical crack growth rates in service have been estimated to vary from 10^{-10}m/s to 10^{-12}m/s.

A comparison of British and U.S. field experience data is given in the report of McMinn et al[3]. Additionally, laboratory studies in environments ranging from steam to concentrated sodium hydroxide solutions are also listed.

V. SUMMARY

The microstructure of three different rotor steels was investigated with the transmission electron microscope. Stress corrosion studies were conducted in carbonate/ bicarbonate and sodium hydroxide solutions by means of slow strain rate tensile and fracture mechanics techniques.

The hot rolled 1%CrMoV steel-"O" showed a ferritic bainitic microstructure with elongated MnS inclusions present. The heat treated 3.5%NiCrMoV steels "A" and "R" revealed an upper bainitic and lower bainitic microstructure respectively. Inclusions in "R" were much bigger than in "A", but less numerous. They were identified in both cases as CaS. In steel "A", oxide inclusions were also found.

With slow strain rate tensile tests, severe cracking of all three steels was found in the carbonate/bicarbonate solutions. The deepest cracks were observed at test potentials near or at the active to passive transition. In the caustic sodium hydroxide solutions only very little cracking could be found.

SCC tests with fracture mechanics specimen showed cracking of all three steels in the sodium hydroxide solution, whereas in the carbonate/bicarbonate environment cracks were found mainly in the 3.5%NiCrMoV steel. SCC tests with steel "O" and "A" showed cracking in NaOH solutions at various potentials in the active and passive region. At the transpassive peak, where chromium dissolution takes place, crack growth rates similar to the active peak were found. At a given stress intensity, the crack growth rates in NaOH were the smallest in steel "A" and about a factor of 5-6 times larger in steel "O". Cracking rates for "R" were similar to steel "O".

The crack path in the steels "A" and "R" was mainly intergranular in all tests. The crack path in steel "O" could not be clearly defined but could have followed the ferrite/bainite boundaries.

In the acidic CO_2/H_2O solution, strong dissolution processes took place at the crack tip of steel "A" and "R", but no "real" cracking could be observed.

The effect of different inclusions could not be completely analysed, but from polarization studies it could be concluded that the effect was rather minimal. The slower cracking of steel "A", as compared to "R", could be due to inclusions but is more probably the result of different steel composition (Mn,Si) and microstructure.

The crack growth rates and fracture appearance found in failed turbine steels is very similar to our SCC results in caustic solutions.

BIBLIOGRAPHY

1. F.F. Lyle and H.C. Burghard, Materials Performance 21, pp. 35-44 (1982).

2. A. McMinn, F.F. Lyle and G.R. Leverant, Corrosion 41, pp. 493-503 (1985).

3. A. McMinn, H.C. Burghard, F.F. Lyle and G.R. Leverant, Proceedings: International Symposium on Environmental Degradation of Materials in Nuclear Power - Systems - Water Reactors, NACE,Houston, Texas, pp.243-272 (1983).

4. J.G. Parker, Eurocor 77: 6th European Congress on Metallic Corrosion, Soc. Chemical Industry, London, England, pp. 555-562 (1977).

5. D.P. Timo, R.M. Curran and R.J. Placek, Workshop Proceedings: Rotor Forgings for Turbines and Generators EPRI, Palo Alto, California, paper 3.8 (1981).

6. A. Choudhurg, R.Jauch, K. Langner and F. Tince, 10th International Forging Conference, The Institute of Metals, Sheffield, England, paper 3 (1985).

7. W.H. Bailey, Workshop Proceedings: Rotor Forgings for Turbines and Generators, EPRI, Palo Alto, California, paper 4.3 (1981).

8. J. Muscroft and D.V. Thornton, ibid. paper 3.6 (1981).

9. K.Forch, ibid., paper 4.18 (1981).

10. G.E. Kerns,M.T. Wang and R.W. Staehle, Stress corrosion Cracking and Hydrogen Embrittlement of Iron Base Alloys NACE, Houston, Texas, pp. 700-735 (1977)

11. C. Parrini and A. DeVito, MICON 78: Optimization of Processing, Properties and Service Performance through Microstructural control, ASTM, Philadelphia, PA, pp.53-73 (1979).

12. H. Finkler and E. Potthast, Workshop Proceedings: Rotor Forgings for Turbines and Generators, EPRI, Palo Alto, California, paper 5.5.1 (1981).

13. R. Narayan and M.C. Murphy, Journal of The Iron and Steel Institute 211, pp. 493-501 (1973).

14. J.F. Smith, J.H. Reynolds and H.N. Southworth, _Acta Metallurgica_ 28, pp. 1555-1564 (1980).

15. P. Machner and W. Meyer, Report: _Vereinigte Edelstahl-werke AG, (EPRI Project RP-1403-8)_, Kapfenberg, Austria (1985).

16. D.A. Vermilyea, _Stress Corrossion Cracking and Hydrogen Embrittlement of Iron Base Alloys_, NACE, Houston, Texas pp.208-217 (1977).

17. R.W. Staehle, ibid., pp. 180-207 (1977).

18. H.H. Uhlig, ibid., pp. 174-179 (1977).

19. J.M. West, _Metal Science_ 14, pp. 534-540 (1980).

20. A. Turnbull, _Corrosion Science_ 23, pp.833-870 (1983).

21. G.J. Bignold, _Corrosion_ 28, pp. 307-312 (1972).

22. D.J. Lees, _The Metallurgist and Materials Technologist_ 14, pp.29-38 (1982).

23. D. Tromans, _Metallurgical Transactions A_ 12A, pp. 1445-1453 (1981).

24. B.G. Ackland and B.W. Cherry, _Australian Welding Research_ 11, pp. 48-54 (1982).

25. K. Kasahara and T. Sato, _Tetsu-to-Hagane_ 69, pp.1463-1470 (1983).

26. G. Schmitt and H. Schlerkmann, _Metallic Corrosion,8th International Congress on Metallic Corrosion_, DECHEMA, Mainz, W. Germany, pp. 426-437 (1981).

27. H.H. Lee, _Corrosion 79_, NACE, Houston, Texas, paper 172 (1979).

28. J.M. Sutcliffe, R.R. Fessler, W.K. Boyd and R.N. Parkins, _Corrosion_ 28, pp. 313-320 (1972).

29. D. Hixson and H.H. Uhlig, _Corrosion_ 32, pp. 56-59 (1976).

30. R.N. Parkins and R.R. Fessler, _Materials in Engineering Applications_ 1, pp. 80-96 (1978).

31. N. Bandyopadhyay, R.C. Newman and K. Sieradzki, _Int'l Congress on Metallic Corrosion_ 2, Nat. Research Council of Canada, Ottawa, Canada, pp. 210-215 (1984).

32. J.G. Parker, Proceedings: <u>Sulfide Inclusions in Steel</u>, ASM, Metals Park, Ohio, pp.403-421 (1975).

33. N. Bandyopadhyay and C.L. Briant, <u>Corrosion 41</u>, pp. 274-280 (1985).

34. S. Somuah, P. Chung, A. Boateng, S. Smialowska, A. Moccari, H. Gayley and D.D. Macdonald, Proceedings: <u>Int'l Symposium on Environmental Degradation of Materials in Nuclear Power-Systems-Water Reactors</u>, NACE, Houston, Texas, pp. 479-505 (1983).

35. R.D. Caligiuri, L.E. Eiselstein and D.R. Curran, ibid., pp. 824-837 (1983).

36. B.W. Roberts and P. Greenfield, <u>Corrosion 9</u>, pp. 402-409 (1979).

37. R.S. Shalvoy, S.K. Duglin and R.J. Lindinger, ibid., pp. 491-497 (1981).

38. M.P. Mueller, Report: <u>Brown Boveri Reasearch Centre</u>, Baden, Switzerland (1984).

39. M.O. Speidel, Report: <u>Institut fuer Metallforschung, ETH</u>, Zuerich, Switzerland (1984).

40. A.K. Agrawal, K.G. Sheth, K. Poteet and R.W. Staehle, <u>Journal Electrochem. Soc. 119</u>, pp. 1637-1644 (1972).

41. R.W. Revie and R.R. Ramsingh, <u>Canadian Metallurgical Quarterly</u>, <u>22</u>, pp. 235-240 (1983).

42. N. Bandyopadhyay and C.L. Briant, <u>Metallurgical Transactions A 14A</u>, pp. 2005-2019 (1983).

43. R.P. Harrison, D.de G. Jones and J.F. Newman, <u>Stress Corrosion Cracking and Hydrogen Embrittlement of Iron Base Alloys</u>, NACE, Houston, Texas, pp. 659-662 (1977).

44. R.N. Parkins, P.W. Slattery and B.S. Poulson, <u>Corrosion 37</u>, pp.650-664

45. N. Bandyopadhyay, C.L. Briant and E.L. Hall, <u>Metallurgical Transactions A 16A</u>, pp. 1333-1344 (1985).

46. J.G. Parker, <u>Br. Corros. Journal 8</u>, pp. 124-127 (1973).

47. <u>Annual Book of ASTM Standards</u>, ASTM, Philadelphia, PA, pp. 453-465 (1973).

48. R.I. Jaffee, P. Machner, W. Meyer and J.E. Steiner, 10th Int'l Forging Conference, The Institute of Metals, Sheffield, England, paper 9 (1985).

49. M. Atkins, Atlas of Continuous Cooling Transformation Diagrams for Engineering Steels, British Steel Corp., Leeds, England (1977).

50. T. Ohhashi, Report: Japan Steel Works Ltd., (EPRI RP2060-1 (1985).

51. R.E. Reed-Hill, Physical Metallurgy Principles, publ. by Van Nostrand Reinhold Ltd., Toronto, Canada (1973).

52. V.F. Zackay and H.I. Aaronson, Decompositon of Austenite by Diffusional Processes Metallurgical Soc. of AIME, N.Y., U.S.A. (1962).

53. H.I. Aaronson, Proceedings: Int'l Symposium on the Mechanism of Phase Transformations in Crystalline Solids, Institute of Metals, London, England (1969).

54. R. Kiessling, Non-Metallic Inclusions in Steel, Metals Society, London, England (1978).

55. D. Crowe, Ph.D. Thesis, U.B.C., Vancouver, B.C. (1985).

56. H.Tada, P.Paris and G. Irwin, The Stress Analysis and Crack Handbook, Del Research Corporation, Hellertown, Pensylvania (1973)

57. A.J. Russell and D. Tromans, Metallurgical Transactions A 12A, pp. 613-621 (1981).

58. B.F. Brown and J.E. Srawley, Plain Strain Crack Toughness Testing, STP. 410; ASTM, Philadelphia (1966).

59. B.F. Brown, Metallurgical Reviews 13, pp. 171-183 (1968).

60. M.J. Robinson and J.C. Scully, Stress Corrosion Cracking and Hydrogen Embrittlement of Iron Base Alloy, NACE, Houston, Texas, pp. 1095-1103 (1977).

61. A.P. Green and B.B. Hundy, Journal Mech. Phys. Sol. 4, pp. 128-144 (1956).

62. R.J. Biernat and R.G. Robins, ELectrochimica Acta 17, pp. 1261-1283 (1972).

63. J.G.N. Thomas, T.J. Nurse and R. Walker, Br. Corros. Journal 5, pp. 87-92 (1970).

64. J.G.N. Thomas and J.D. Davies, Br. Corros. Journal 12, pp. 108-114 (1977).

65. J.A. Von Fraunhofer, Corrosion Science 10, pp. 245-251 (1970).

66. D.H. Davies and G.T. Burstein, Corrosion 36, pp. 416 -422 (1980).

67. F. Clerbois et J. Massart, Corrosion Science 2, pp. 1-20 (1962).

68. M. Pourbaix, Atlas of Electrochemical Equilibria in Aqueous Solutions, NACE, Houston, Texas (1974)

69. D. Crowe and D. Tromans, Canadian Metallurgical Quarterly, 24, pp. 99-106 (1984)

70. C.L. Foley, J.Kruger and C.J.Bechtoldt, Journal Electrochemical. Soc. 114, pp. 994-1001 (1967).

71. D.D. Macdonald and B. Roberts, Electrochimica Acta 23, pp. 781-786 (1978).

72. Y. Geronov, T. Tomov and S. Georgiev, Journal of Applied Electrochemistry 5, pp. 351-358 (1975).

73. D.D. Macdonald and D. Owen, Journal Electrochem. Soc. 120, pp.317-324 (1973).

74. G. Herbsleb and R. Poepperling, Werkstoffe und Korrosion 29, pp. 732-739 (1978).

75. J. Scully, Corrosion Science 20, pp. 997-1016 (1980).

76. W.R. Brose, Fracture Mechanics, 14th Symposium, ASTM, Philadelphia, PA, pp. 463-481 (1983).

77. M. Takemoto, Proceedings: International Congress on Metallic Corrosion, Toronto, pp.565-577 (1984).

78. E. Wendler-Kalsch, Werkstoffe und Korrosion 31, pp. 534-542 (1980).

79. F.F. Lyle, Corrosion 84, New Orleans, LA, paper 174 (1984).